OSCILLATION SEARCH STUDY USING TAU-TO-ELECTRON DECAY
CHANNEL IN THE CHORUS EXPERIMENT

A THESIS SUBMITTED TO
THE GRADUATE SCHOOL OF NATURAL AND APPLIED SCIENCES
OF
THE MIDDLE EAST TECHNICAL UNIVERSITY

BY

ERHAN PESEN

IN PARTIAL FULFILLMENT OF THE REQUIREMENTS FOR THE DEGREE OF

DOCTOR OF PHILOSOPHY

IN

THE DEPARTMENT OF PHYSICS

NOVEMBER 1997

ABSTRACT

OSCILLATION SEARCH STUDY USING TAU-TO-ELECTRON DECAY
CHANNEL IN THE CHORUS EXPERIMENT

Pesen, Erhan

PhD, Department of Physics

Supervisor: Prof. Dr. Perihan Tolun

November 1997, 127 pages.

The CHORUS experiment is designed to search for $\nu_\mu \to \nu_\tau$ oscillation by detection of ν_τ in a ν_μ neutrino beam, with three decay channels of the tau lepton. These are the $\tau^- \to \mu^- \nu_\tau \overline{\nu}_\mu$, $\tau^- \to h^-(n\pi^0)\nu_\tau$ and $\tau^- \to \pi^+ \pi^- \pi^+ (n\pi^0)\nu_\tau$ decay channels. In this thesis the possibility of using the $\tau^- \to e^- \nu_\tau \overline{\nu}_e$ decay channel of the tau lepton, for ν_τ detection with the CHORUS detector, is studied. A 95% electron identification efficiency is obtained. When all detection efficiencies are taken into account, $4-6\%$ improvement on $\sin^2 2\theta_{\mu\tau}$ limit at large Δm^2 is achieved without any extra emulsion scanning load.

Keywords: Neutrino, Neutrino Mass, Neutrino Oscillation, Tau Detection

ACKNOWLEDGMENTS

TABLE OF CONTENTS

LIST OF TABLES

LIST OF FIGURES

CHAPTER 1

INTRODUCTION

Neutrinos are still the most mysterious particles, needing new experiments to be explored, although the number of experiments which are being carried out to investigate their properties is already considerable compared to those for other particles. In spite of these experiments, what physicists know is less than what they do not know about these particles. With their mysterious properties, they are always good candidates as solutions of the problems appearing in the high energy physics and astrophysics (like being a dark matter candidate).

The neutrino story starts with Pauli's hypothesis of a third decay particle of zero mass, and zero charge in nuclear beta-decay processes to explain the observation of the continuous beta ray energy spectra which was first observed by Chadwick in 1914. A single energy value would be expected for a two body decay process. This problem existed many years until Fermi came with the first theory of weak interactions [1] in 1932. Fermi theory included the new particle introduced by Pauli in the beta decay process. This particle was later called "neutrino" (meaning "the small neutron") and investigations on the properties of neutrinos started. Such experiments are still continuing.

An interesting reaction, called inverse beta decay, is discussed by Pontecorvo [2]

in 1946; first calculations of this reaction showed that neutrino interactions have very small detection cross-sections ($\sigma \sim 6 \times 10^{-44}\ cm^2$) which meant that very intense neutrino sources are necessary to carry out an experiment. Later on, first experimental observation of the neutrinos was achieved [8] by Reines and Cowan (1956-58) in an experiment using anti-neutrinos from a nuclear power plant. Further developments in weak interactions lead to an increased interest in the properties to these particles. Firstly, parity violation in weak interactions [3, 4] was tested experimentally [5, 6] by studying the beta decay process and resulted in the formulation of the V-A structure of the weak theory. Secondly, the helicity of the neutrinos was investigated; they all seemed to have negative (left-handed) helicity [7]. In the 1960s, it was shown experimentally that muons do not decay to electrons electromagnetically ($Br(\mu \rightarrow e\gamma) < 10^{-8}$ [9]) which was considered as a strong indication for the existence of a second neutrino species [10]. Violation of the expected increase of the elastic cross-section with increase in the neutrino energy motivated the physicists to investigate more neutrino interactions at high neutrino energies [10]. Neutrinos were produced ($\sim 1\ GeV$) with the accelerated protons ($\sim 15\ GeV$) at Brookhaven National Laboratory (BNL). The results of a famous experiment with an accelerator neutrino beam at Brookhaven indicated the existence of a second kind of neutrino which was the muon-neutrino [11].

Neutral current interaction of neutrinos are predicted by the electroweak theory [12, 13, 14]. These interactions were first observed at the Gargamelle bubble chamber experiment at CERN [15]. These successes are followed by the discovery

of a third family of leptons at the SPEAR e^-e^+ collider experiment by anomalous lepton production [16] in the process $e^-e^+ \rightarrow l^+l'^- + E_{miss}$. The tau lepton was observed while indicating the existence of a ν_τ only indirectly. More recent measurements on the width of the Z boson line-shape at LEP (CERN) show that there should be 3 neutrino families if the mass of all neutrinos are restricted to be less than 45 GeV. There exist theoretical studies concerning the existence of a 4th lepton family [17] with the assumption of higher neutrino masses.

There are unresolved physics problems related to investigations on neutrinos. The first one of these is the so called "solar neutrino problem". The expected neutrino flux from the sun [18, 19] is not in agreement with that measured by the Homestake [20], GALLEX [21], SAGE [22] and Kamiokande [23] experiments. The second one is the "atmospheric neutrino problem". Naive expectations show that expected numbers of ν_μ and $\overline{\nu}_\mu$ from atmospheric production reactions should be larger those that of ν_e and $\overline{\nu}_e$ by a factor of two. These neutrinos are produced by $\pi^\pm$ decays in the atmosphere. The ratio of the two neutrino species obtained by experiments and calculations, are compared in the literature. Discrepancies are obtained in the results by different experiments (FREJUS [24], Kamiokande [25] and IMB [26]). Experimental problems can be the possible reason for these discrepancies. However, this is unlikely since many different techniques are used. Alternatively, there can be theoretical problems like missing knowledge or there can be a particle physics solution like the MSW effect, neutrino oscillations, etc. More experiments with different techniques are necessary to investigate these effects and related neutrino properties further. Especially the phenomenon of

3

"neutrino oscillations" may or may not exist.

Neutrino mass being very small is also another puzzling property. There are many attempts to measure the neutrino mass directly. Alternatively, neutrino oscillations [27, 28] may be taken as an direct indication of the existence of neutrino mass. On the other hand, the existence of a massive neutrinos does not mean that there must be oscillations although it is likely that they go together. There is no indication of neutrino mass in the Standard Model; however, existing problems which lead physicists towards the suspician that neutrinos are massive.

Neutrino oscillations can be searched for with many different techniques and in many different regions on the parameter space, depending on the distance between the neutrino production point and the experimental set-up (long and short baseline), energy (high and low) and the source of the neutrinos (reactor, accelerator, astrophysical and solar). There can also be a classification by the neutrino detection method into two main classes: appearance and disappearance experiments. For reactor experiments (e.g. Gösgen [29]) only the disappearance method is possible by using $\overline{\nu}_e$ neutrinos because of their low energetic neutrino beams are below threshold to produce the other leptons. They are sensitive to lower Δm^2 (see section 2.4.3) region in the parameter space. Search of $\nu_\mu \to \nu_\tau$ oscillations, which is of particular interest to this study, is not possible with reactor and solar neutrino experiments since the tau neutrino charged current (CC) interactions have a too high energy threshold. Astrophysical neutrino observations are sensitive in different regions on the exclusion plot (low Δm^2 region [26]) compared to accelerator experiments. Accelerator experiments, on the other hand,

are more flexible as regards to the region to which they are sensitive and they are sensitive mainly to high Δm^2 and low $\sin^2 2\theta$ regions in the parameter space (with a multitude of combinations for 3 neutrino species). There has been recently an exciting result obtained by the LSND collaboration: they claimed to have found an evidence for $\overline{\nu}_\mu \rightarrow \overline{\nu}_e$ neutrino oscillation with a probability of $(0.34^{+0.20}_{-0.18} \pm 0.07)\%$ [30] and for $\nu_\mu \rightarrow \nu_e$. neutrino oscillation with a probability of $(0.26 \pm 0.1 \pm 0.05)\%$ [31]

The CHORUS experiment is designed to attempt a direct observation of the tau neutrino and in this way to search for $\nu_\mu \rightarrow \nu_\tau$ oscillation [32]. It is a high energy accelerator neutrino experiment since the neutrinos are obtained from protons accelerated to $\sim 450\,GeV$ at the CERN SPS. It is a "short baseline" experiment with $L = 400 - 800\ m$. Hybrid experimental detection techniques are used: the set-up is constructed using photograpic (emulsion) and electronic (trackers, calorimeter, spectrometer, etc.) detectors. Tau detection is planned via three decay channels of the tau lepton $(\tau^- \rightarrow \mu^- \nu_\tau \overline{\nu}_\mu\ ,\ \ \tau^- \rightarrow h^-(n\pi^0)\nu_\tau$ and $\tau^- \rightarrow \pi^+ \pi^- \pi^+ (n\pi^0)\nu_\tau)$. The fourth decay channel, which is $\tau^- \rightarrow e^- \nu_\tau \overline{\nu}_e$, was not included since the detector is not specifically designed to detect electrons emitted in this channel. With present conditions and 4 years of data taking, an improvement of a factor of 25 ($\sin^2 2\theta_{\mu\tau} \leq 2 \times 10^{-4}$) is expected in the $\sin^2 2\theta_{\mu\tau}$ limit at large Δm^2 when compared with the latest limit ($\sin^2 2\theta_{\mu\tau} \leq 5 \times 10^{-3}$) [33].

In this study, the possibility of tau neutrino detection via $\tau^- \rightarrow e^- \nu_\tau \overline{\nu}_e$ decay channel with the CHORUS detector, is investigated. In the second chapter neutrino properties and the neutrino oscillation phenomenon are reviewed.

Design details of the CHORUS experimental set-up relevant to this analysis, are presented in the next chapter. Hardware and software contributions to the experiment are explained in chapter four. The following chapter includes the improvements achieved for the detection of this channel, details of obtaining relevant parameters for the analysis and at the end, results obtained from this study. Moreover, the contribution from this channel to the CHORUS $\sin^2 2\theta_{\mu\tau}$ sensitivity is evaluated. Discussions and conclusions are presented as a final chapter. In addition, a powerful method to suppress the charm background, is shown in detail in the appendix.

CHAPTER 2

NEUTRINO OSCILLATION PHENOMENOLOGY

2.1 Intrinsic neutrino properties

Some basic intrinsic properties of the neutrinos are discussed at an elementary level in the first few sections. A more thorough discussion of neutrino mixing follows in the remaining sections of this chapter.

2.1.1 Mass of the neutrinos

Neutrinos were first postulated by Pauli as massless particles and they are assumed to be massless according to the standard model of weak interactions. However, a small mass may be handled by the theory; at present massive neutrinos are believed to be more probable. If they are massive, they can explain some unsolved existing physical problems like the dark matter problem in astrophysics. Some experimental results can be interpreted in this direction. Also in Grand Unified Theories, neutrinos have to be massive. There are many different experimental techniques, used to measure the mass of the neutrinos. These are direct measurements and indirect ones, such as testing the existence of neutrino mass with neutrino oscillations. The latter method is sensitive to very small masses.

2.1.2 Helicity of the neutrinos

Massive particles with non-zero spin can have a component of the spin which is not aligned with their motion. Helicity is the component of the spin in the direction of the motion (i.e. the momentum vector). Then, particles with their spin vector in their momentum direction, have helicity $(+1)$ and are called right-Handed (RH) particles and particles with their spin vector opposite to their momentum direction have helicity (-1) and are called left-Handed (LH) particles. This classification holds for neutrinos too. That is, neutrinos can be either right-handed or left-handed. Experimental results show that, only LH neutrinos and RH antineutrinos are observable.

2.1.3 Particle-antiparticle properties

In nature, particles are associated with their antiparticles as follows: Antiparticles have the same properties as the particles, except for the sign of the electric charge and other chargelike attributes.

Neutrinos, however, do not carry electric charge. Experiments indicate that neutrinos carry helicity and lepton number which is a good quantum number used to distinguish a lepton from an antilepton; however, the experimental evidence for the existence of this number may be evaded. Thus, it is indeed possible that the neutrino is its own antiparticle, in the case of Majorana neutrinos.

2.1.4 Electromagnetic properties of the neutrinos

Majorana neutrinos have no magnetic or electric dipole moment. However, according to the standard model, Dirac neutrinos, which have mass m_ν, will have a magnetic and an electric dipole moment. Both electric and magnetic moments are so far too small to be detected experimentally, if we use the present mass limit m_ν for neutrinos.

2.2 The Standard Model of electroweak interactions

Available experimental data, are in good agreement with the Standard Model of electroweak interactions, developed by Glashow [12]), Weinberg [13] and Salam [14]. In the Lagrangian the neutrino and the charged lepton form doublets of an $SU(2)_L$ group. Invariance under global $SU(2)_L$ transformations has to be extended so that both weak and electromagnetic interactions are covered. This is achieved by extending the group to $SU(2)_L \times U(1)$ where U(1) is the group of the weak hypercharge. Then invariance under the local $SU(2)_L \times U(1)$ gauge transformations holds.

Local $SU(2)_L \times U(1)$ gauge invariance is satisfied, only if all the particle masses in the theory, are zero. This is not the situation in reality, but the problem is solved by the so called "Higgs Mechanism" which spontaneously breaks $SU(2)_L \times U(1)$ gauge symmetry [34] and introduces the particle masses. The Higgs fields are supposed to interact with all boson and fermion fields. The corresponding coupling is introduced in such a way that local gauge invariance is preserved.

By choosing suitable, non-zero vacuum expectation values and the right field couplings, masses of the intermediate vector boson fields, masses of the fermions and Higgs bosons can be generated. This can be done in the quark sector [35] by choosing Yukawa-type coupling for quark-Higgs-field interaction.

A similar method could be used to give mass to the neutrino by the Higgs mechanism, however, the absence of RH neutrino fields in the standard model, makes the process impossible (to preserve the renormalizability). With this result, it can be said that neutrinos are massless in the standard theory of weak interactions.

If neutrinos are massive, which is not build into the standard theory, the phenomenon of mixing can occur in the lepton sector. Theoretically, lepton mixing can take place in many different ways because neutrinos are neutral particles. Lepton mixing violates lepton charge conservation. Besides, neutrinos can be Dirac ($\nu \neq \overline{\nu}$) or Majorana particles ($\nu = \overline{\nu}$). It is also possible that the number of neutrinos may be larger than number of charged leptons. All these possibilities are going to be discussed in the following sections in an elementary formulation.

2.3   Neutrino mixing schemes

Neutrino mixing schemes are classified by the type of mass term whose diagonalization leads to the corresponding mixing. By using left and right handed neutrino fields and by using their charge conjugate fields, the following possible

neutrino mass terms can be constructed.

$$L^{D+M} = -\frac{1}{2}\overline{(\nu_L)^c}M_L^M\nu_L - \frac{1}{2}\overline{\nu_R}M_R^M(\nu_R)^c - \overline{\nu_R}M^D\nu_L + H.c. \qquad (2.1)$$

where M^D,M^M,M_L^M and M_R^M are $n \times n$ matrices. The third term in the equation, which corresponds to L^D (Dirac mass term), is invariant under local gauge transformations which implies conservation of lepton charges. The other two terms are not invariant and they are called Majorana mass term (L^M).

2.3.1 Dirac mass term

In this case, only the L^D part of the eqn.(2.1), is kept and the following form can be obtained:

$$L^D = - \sum_{l,l'=e,\mu,\tau,....} \overline{\nu_{l'R}}M_{l'l}^D\nu_{lL} + H.c. \qquad (2.2)$$

M^D in this equation has to be diagonalized with the help of biunitary transformations [1]. With the neutrino mass term (2.2), the flavour neutrino fields ν_{lL} which exist in the standard model are linear combinations of the LH components of the fields of neutrinos with definite masses as,

$$\nu_{lL} = \sum_{k=1}^{n} U_{lk}\nu_{kL} \quad , \quad l = e, \mu, \tau, ... \qquad (2.3)$$

where U is the lepton mixing matrix. With this equation, eqn.(2.2) is invariant under global gauge transformations and hence lepton charges are conserved. The fields ν_{lL} are the fields in weak interactions. If M^D is not diagonalized, lepton

---

[1]
$$\nu_L = U \cdot \nu_L' \quad , \quad \nu_R = V \cdot \nu_R' \quad , \quad U \cdot U^\dagger = V \cdot V^\dagger = \mathbf{I}$$

charges are not conserved, however, the theory will be still invariant under global gauge transformations. With this mass term, total lepton charges are conserved which allows the processes like $\mu^- \to e^- \gamma$ while not permitting the processes like $K^+ \to \pi^- + e^+ + \mu^+$. Given these properties, the mixing of neutrinos with a Dirac mass term is similar to the case of quark mixing [28].

2.3.2 Majorana mass term

Leaving out the Dirac term in eqn.(2.1), the following mass term is obtained [36].

$$L^M = -\frac{1}{2} \sum_{l,l'=e,\mu,\tau,....} \overline{(\nu_{l'L})^c} M_{l'l} \nu_{lL} + H.c. \tag{2.4}$$

In this case M is a symmetric matrix $(M^T = M)$ and care has to be taken while diagonalizing the matrix. This calculation leads to the following neutrino mixing matrix,

$$\nu_{lL} = \sum_{k=1}^{n} U_{lk} \chi_{kL} \quad , \quad \chi_{kL} = U^\dagger \nu_{kL} + (U^\dagger \nu_{kL})^c \quad , \quad \chi_k = C \overline{\chi_k}^T \tag{2.5}$$

where C is the charge-conjugate matrix. The eqn.(2.5) shows that, LH flavour neutrinos are the linear combinations of LH Majorana neutrino field components with definite mass and it shows that neutrinos are equal to the corresponding anti-neutrinos. It can be concluded that there are $2n$ Majorana field components corresponding to the total number of neutrino flavours $(2n \ , \ \nu_e......\overline{\nu}_\tau)$. The eqn.(2.4) is not invariant under global gauge transformations because of the equality of neutrinos and anti-neutrinos. Lepton flavour charges and total lepton charges are not conserved as a consequence and processes like neutrinoless

double beta decay $(\beta\beta_{0\nu})$ are allowed. The observation of this process can help to disentangle the question of whether neutrinos are Majorana or Dirac particles.

2.3.3   Dirac-Majorana mass term

In all the cases above, the number of massive Dirac or Majorana neutrinos always coincides with the number of neutrino flavours. In the Dirac and Majorana neutrino mixing case, the number of massive neutrinos exceed the number of flavour neutrinos. The form of the Lagrangian in eqn.(2.1), can be shown for this case, to be

$$L^{D+M} = -\frac{1}{2}\overline{(n_L)^c}Mn_L + H.c. \tag{2.6}$$

where M is a $2n \times 2n$ matrix and n_L is equal to

$$n_L = \begin{bmatrix} \nu_L \\ (\nu_R)^c \end{bmatrix} \tag{2.7}$$

Again by applying the diagonalization procedure to M term and again by considering a symmetric M, we can obtain a mixing equation of the form,

$$\nu_{lL} \ = \sum_{k=1}^{2n} U_{lk}\chi_{kL}, \quad \chi = U^\dagger n_L + (U^\dagger n_L)^c \quad , \quad \chi_k = C\overline{\chi_k}^T$$

$$(\nu_{lR})^c \ = \sum_{k=1}^{2n} U_{\bar{l}k}\chi_{kL} \tag{2.8}$$

The above neutrinos are LH neutrinos, and similar equations can be written for RH neutrinos as

$$(\nu_{lL})^c = \sum_{k=1}^{2n} U_{lk}^* \chi_{kL} \quad , \quad \nu_{lR} = \sum_{k=1}^{2n} U_{\bar{l}k}^* \chi_{kL} \tag{2.9}$$

13

Equations (2.8) and (2.9) show that the Dirac-Majorana mass term is not invariant under global gauge transformations and no lepton charge is conserved as a consequence. This term also allows neutrinoless double beta decay due to the same reason. The main difference between the Dirac-Majorana mass term and the Dirac or Majorana mass term is that, in the former case not only oscillations between neutrinos but also between neutrinos and anti-neutrinos, is possible. RH neutrinos (LH anti-neutrinos), which are not taken as part of the standard model, are assumed to be "sterile" [27] which means that they do not have any kind of interaction with other particles.

2.4 Neutrino oscillation

2.4.1 Dirac or Majorana mass term

The two cases can be considered together, since they have similar mixing formalisms as in eqn.(2.3) with the field ν_k with definite mass m_k. In both cases U is a $n \times n$ matrix and n is the number of charged leptons. The state vectors $(\nu_e$, ν_μ , ..) that take part in weak interactions are superpositions of the state vectors of Dirac or Majorana neutrinos with different masses. If this is the case in reality, then, these state vectors of the neutrinos with definite masses will have different phase factors at some distance from the detector. Thus, composition of state vectors will change and therefore, neutrino type will change. In other words, for a neutrino beam with a specific neutrino type, change (oscillation) to another type will occur, depending on the distance from the production point

and on some other parameters, which will be discussed soon.

If we consider a neutrino beam with a momentum **p** which is larger than the mass of the neutrino itself, eqn.(2.3) can be rewritten as

$$|\nu_l >_t \; = \; \sum_{k=1}^{n} e^{-iE_k t} \; U_{lk}^* \; |k, L > \quad , \quad |\overline{\nu}_l >_t \; = \; \sum_{k=1}^{n} U_{lk} \; e^{-iE_k t} \; |k, R > \quad (2.10)$$

where $|k, L > (|k, R >)$ is the neutrino (anti-neutrino) state with momentum **p**, mass m_k and negative (positive) helicity. Here, mass differences of ν_k are assumed to be small so that it can be handled with the weak interactions [37]. In these equations, initial time is taken as zero. To obtain the probability amplitude for finding a given type of neutrino in a beam of neutrinos, it is necessary to decompose $|\nu_l >_t$ over the complete set of neutrino state vectors $|\nu_l >$. When this is done, the transition probability of neutrinos (anti-neutrinos) can be calculated as

$$P_{\nu_{l'} \to \nu_l}(t) \; = \; \left| \sum_{k=1}^{n} U_{l'k} \; e^{-iE_k t} \; U_{lk}^* \right|^2 \quad , \quad P_{\overline{\nu}_{l'} \to \overline{\nu}_l}(t) \; = \; \left| \sum_{k=1}^{n} U_{l'k}^* \; e^{-iE_k t} \; U_{lk} \right|^2 (2.11)$$

where $P_{\nu_{l'} \to \nu_l}(t) \; (P_{\overline{\nu}_{l'} \to \overline{\nu}_l}(t))$ is the probability amplitude of the transition of ν_l $(\overline{\nu}_l)$ into $\nu_{l'}$ $(\overline{\nu}_{l'})$ at a time t after the production of ν_l $(\overline{\nu}_l)$ at $t = 0$. As can be seen from eqn.(2.11), both probabilities are equal to each other which is a general consequence of CPT invariance. Moreover, the sum of the transition probabilities of a given neutrino (anti-neutrino) into other neutrinos (anti-neutrinos) is equal to unity which is the result of having a unitary mixing matrix. Furthermore, because of the structure of the equations, physical phases [2] do not enter into the

---

[2]   There are $\frac{(n-1)(n-2)}{2}$ physical phases of Dirac $((\frac{n(n-1)}{2})$ for Majorana) neutrinos which cannot be absorbed by unitary transformations where n is the dimensions of the mixing matrix.

expressions for the probabilities. Physical phases are the main difference that can be noticed between Dirac and Majorana masses and hence it is impossible to differentiate between them by using neutrino oscillations in vacuum.

The assumption of having large momentum with respect to the neutrino mass allows one to make the simplification: $E_k \simeq p + \frac{m_k^2}{2p}$. Thus, eqn.(2.11) can be written in expanded form for better interpretation.

$$P_{\nu_{l'} \to \nu_l}(L/p) =$$
$$\delta_{l'l} + 2 \sum_{j>k} |U_{l'j} U_{lj}^* U_{l'k}^* U_{lk}| \ [\cos(\frac{m_j^2 - m_k^2}{2p}L - \phi_{jk,l'l}) - \cos\phi_{jk,l'l}] \ (2.12)$$
$$\phi_{kj,l'l} = arg(U_{l'k} U_{lk}^* U_{l'j}^* U_{lj})$$

It is obvious from the equations that neutrinos, which participate in the oscillation, can not be of the same type. Also, if all neutrino masses are equal to each other, no oscillation can occur. A similar equation can be derived for oscillation probabilities of anti-neutrinos. Consequently, neutrinos can oscillate only if there exist at least two neutrinos with different masses and if at least some nondiagonal elements of the lepton mixing matrix are different from zero.

2.4.2 Dirac-Majorana mass term

Oscillation of neutrinos in vacuum in the case of A Dirac-Majorana mass term, can be calculated in a way which is similar to that for separate Dirac or Majorana mass terms. Eqn.(2.9) can be used for this purpose. The assumption of large neutrino momentum with respect to its mass, is still valid. Since LH anti-neutrinos

(RH neutrinos) do not take part in the standard model interactions, these particles are assumed to be sterile, as mentioned before. Using a similar method, the probability of finding another neutrino types inside the original neutrino beam, can be calculated as

$$P_{\nu_{l'} \to \nu_l}(L/p) =$$
$$\sum_{k=1}^{2n} |U_{l'k}|^2 \ |U_{lk}|^2 + 2 \sum_{j>k} |U_{l'j}U_{lj}^*U_{l'k}^*U_{lk}| \ \ \cos[\frac{m_j^2 - m_k^2}{2p}L - \phi_{jk,l'l}] \ (2.13)$$
$$P_{\overline{\nu}_{l'L} \to \nu_l}(L/p) =$$
$$\sum_{k=1}^{2n} |U_{\overline{l'}k}|^2 \ |U_{lk}|^2 + 2 \sum_{j>k} |U_{\overline{l'}j}U_{lj}^*U_{\overline{l'}k}^*U_{lk}| \ \ \cos[\frac{m_j^2 - m_k^2}{2p}L - \phi_{jk,\overline{l'}l}] \ (2.14)$$
$$\phi_{jk,l'l} = arg(U_{l'j}U_{lj}^*U_{l'k}^*U_{lk}) \quad , \quad \phi_{jk,\overline{l'}l} = arg(U_{\overline{l'}j}U_{lj}^*U_{\overline{l'}k}^*U_{lk})$$

Therefore, in the case of Dirac-Majorana mass term, neutrino mixing implies that both the probability of finding a sterile neutrino and finding a different type of active neutrino , at some distance from the source may be different from zero. It should not be forgotten here that, only the oscillation between active neutrinos, is possible in the Dirac or Majorana mass term cases. Transition probabilities for $\nu_{l'} \to \nu_l$ and $\overline{\nu}_{l'} \to \overline{\nu}_l$, are equal again as a consequence of CPT invariance. As a result of the above formulation it is possible, in principle, to observe the existence of the sterile neutrinos, by looking at disappearance of the neutrinos in the beam.

2.4.3 Neutrino oscillation between two types of neutrinos

This is the simplest case for the oscillation scenarios. If the neutrinos with definite masses (ν_1 and ν_2 in this case) are Dirac particles, the mixing matrix will

be a real, orthogonal 2×2 matrix with the general form

$$U = \begin{bmatrix} \cos\theta & \sin\theta \\ -\sin\theta & \cos\theta \end{bmatrix} \qquad (2.15)$$

where θ is the lepton mixing angle. If the massive neutrinos are Majorana or Dirac-Majorana particles, the mixing matrix will have again one angle but with CP-violating phase factors. However, the oscillation probability calculations does not change since they do not depend on the phase factors. With some simplifications, the probability of oscillation between two neutrino types at some distance, from the neutrino production point , can be derived from eqn.(2.12) as,

$$P_{\nu_{l'} \to \nu_l} = P_{\bar{\nu}_{l'} \to \bar{\nu}_l} = \sin^2 2\theta \, \sin^2 \left(\frac{1.27 \, \Delta m^2 \, L}{E} \right) \qquad (2.16)$$

where L is in km , E is in GeV and Δm^2 , which is $|m_1^2 - m_2^2|$, is in eV^2 ($\hbar = c = 1$). The formula (2.16) has been derived by assuming a common momentum (but different energies) for the mass eigenstates ν_l. This assumption is not correct because of the uncertainty principle in quantum mechanics. A fixed momentum would mean a complete uncertainty in the location of the neutrino and every possible oscillation pattern will disappear. There must be some uncertainty in the neutrino momentum in order to establish the neutrino source, as well as the detection points, that are both localised within an oscillation length. A proper wavepacket treatment takes these facts into account [37] and such a treatment leads to the results obtained above.

At large Δm^2 values, the probability function in eqn.(2.16), depends only on the mixing angle θ. In principle, an experiment should have E , L and Δm^2

Reactor

Atmospheric

Accelerator

Solar

| 10^2 | 10 | 1 | 10^{-1} | 10^{-2} | 10^{-3} | 10^{-4} | 10^{-10} | 10^{-11} |

L/E (km/GeV)

| 10^2 | 10 | 1 | 10^{-1} | 10^{-2} | 10^{-3} | 10^{-4} | 10^{-10} | 10^{-11} |
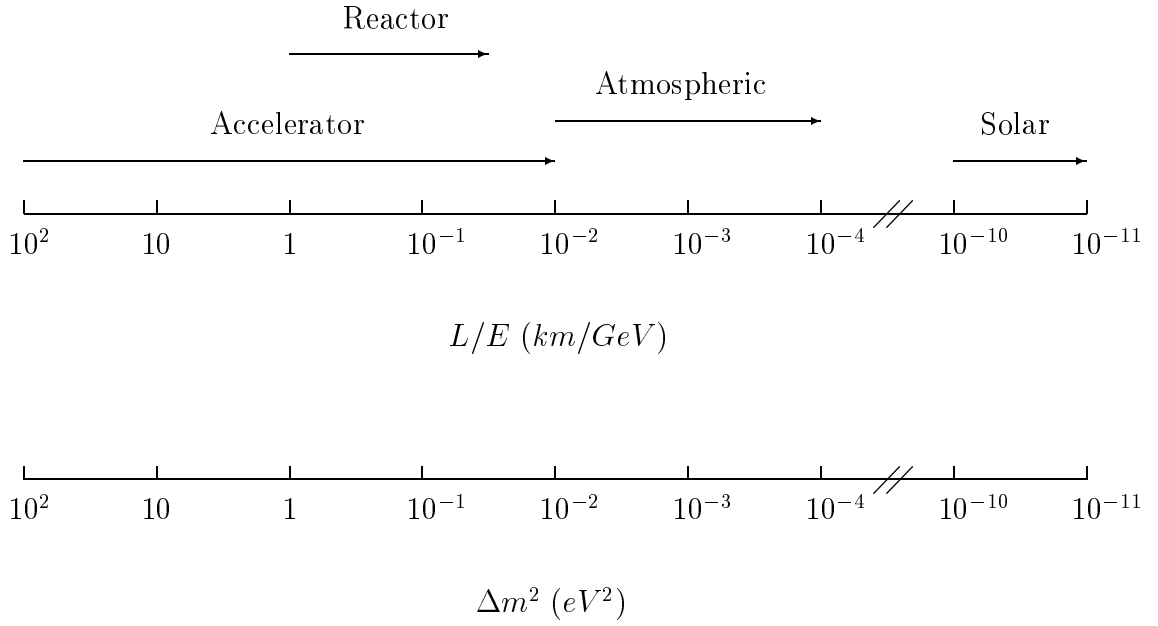
Δm^2 (eV^2)

Figure 2.1: Ranges of L/E and Δm^2 for various neutrino oscillation experiments values such that the oscillation probability is maximum. This is satisfied by the condition Δm^2 $(eV^2) \sim L/E$ (km/GeV). Knowing the mean energy of the neutrino beam, the detector distance can be arranged such that the desired Δm^2 region has been chosen. The range of Δm^2 explored in various experiments as a function of L/E , is shown in figure 2.1.

19

CHAPTER 3

THE CHORUS EXPERIMENT

The general structure of the experimental set-up can be seen in figure 3.1. It consists mainly of an emulsion target, trigger planes, fiber trackers, hexagonal magnet, calorimeter and spectrometer. The trigger system is explained in detail in the following chapter with a simulation of the performance. Only the main detector elements are summarised as far as they are relevant for this analysis. All the details of the experimental set-up can be found elsewhere [38].

Conceptually, the CHORUS experiment is designed to detect the tau neutrino with three decay channels of the tau particle. These are $\tau^- \to \mu^- \nu_\tau \overline{\nu}_\mu$, $\tau^- \to h^- (n\pi^0)\nu_\tau$ and $\tau^- \to \pi^+ \pi^- \pi^+ (n\pi^0)\nu_\tau$. The experiment starts with the ν_μ neutrino beam and looks for the appearance of ν_τ CC interactions in emulsion. The existence of a kink track due to a tau decay, is the sign of the tau neutrino interaction. The detector is positioned $400 - 800\ m$ away from the ν_μ production point. When CERN SPS WB neutrino beam energy spectrum is considered, the detector has maximum $\sin^2 2\theta_{\mu\tau}$ sensitivity at $\Delta m^2 = 50\ eV^2$. With its actual energy and distance from the neutrino production point, CHORUS is a short baseline experiment.
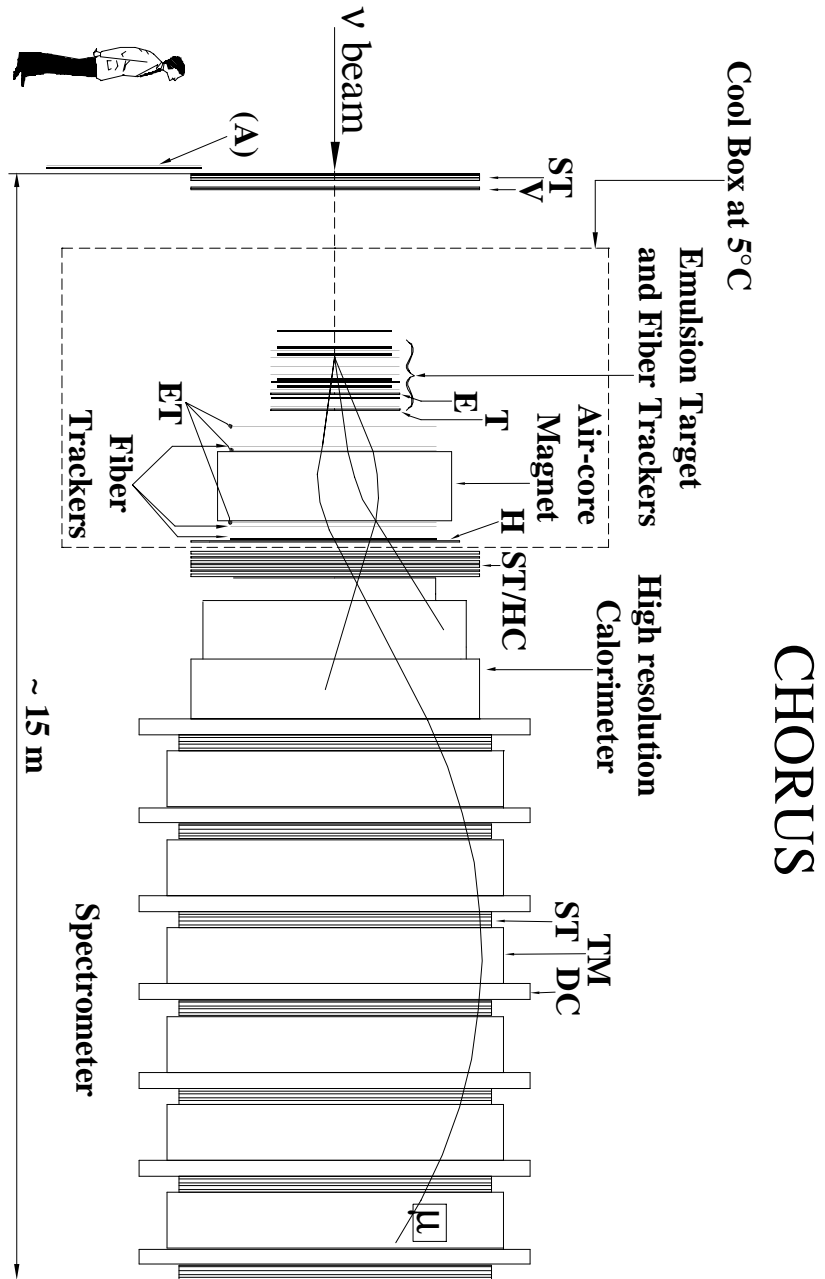
Figure 3.1: Sketch of the CHORUS detector

3.1 Neutrino beam

Protons that are accelerated to the energy of 450 GeV in the CERN SPS, are sent onto a berilium target which consists of 11 rods 10 cm long with 3 mm diameter. This is larger than the diameter of the proton beam to utilise all the protons that are available in the beam. There exists a cooling system for the berilium target which enables one to hit it with high proton intensities (a total of $\sim 3.4 \times 10^{13}$ protons in both spills). With the collision of protons and nucleons in the berilium target, pions and kaons are produced. Neutrinos originate from their decay in flight, mostly in a 289 m long vacuum decay tunnel.

The berilium target is followed by a horn and reflector (see figure 3.2). Negative particles are defocused by these devices and stopped in collimators. Positive hadrons are focused to produce ν_μ neutrinos. The magnetic lenses are followed by a decay tunnel which is mentioned above. In spite of the strong defocusing, background neutrinos ($\overline{\nu}_\mu$, $\overline{\nu}_e$) are still produced due to the decay of negative particles. Relative abundances of these neutrinos with respect to the ν_μ neutrinos, are listed in table 3.1 with their mean energy. Also the neutrino beam energy spectra can be seen in figure 3.3 for different neutrino types. The last structure in the neutrino beam line, is two blocks of iron shield (185 m and 39.5 m long) to eliminate beam related muons. There is also 100 m earth in between these two iron blocks, which serves also as shielding material for muons.

Abundances and mean energies of neutrino species were measured also in CHARM II experiment [39] in a slightly different beam setup. The corresponding
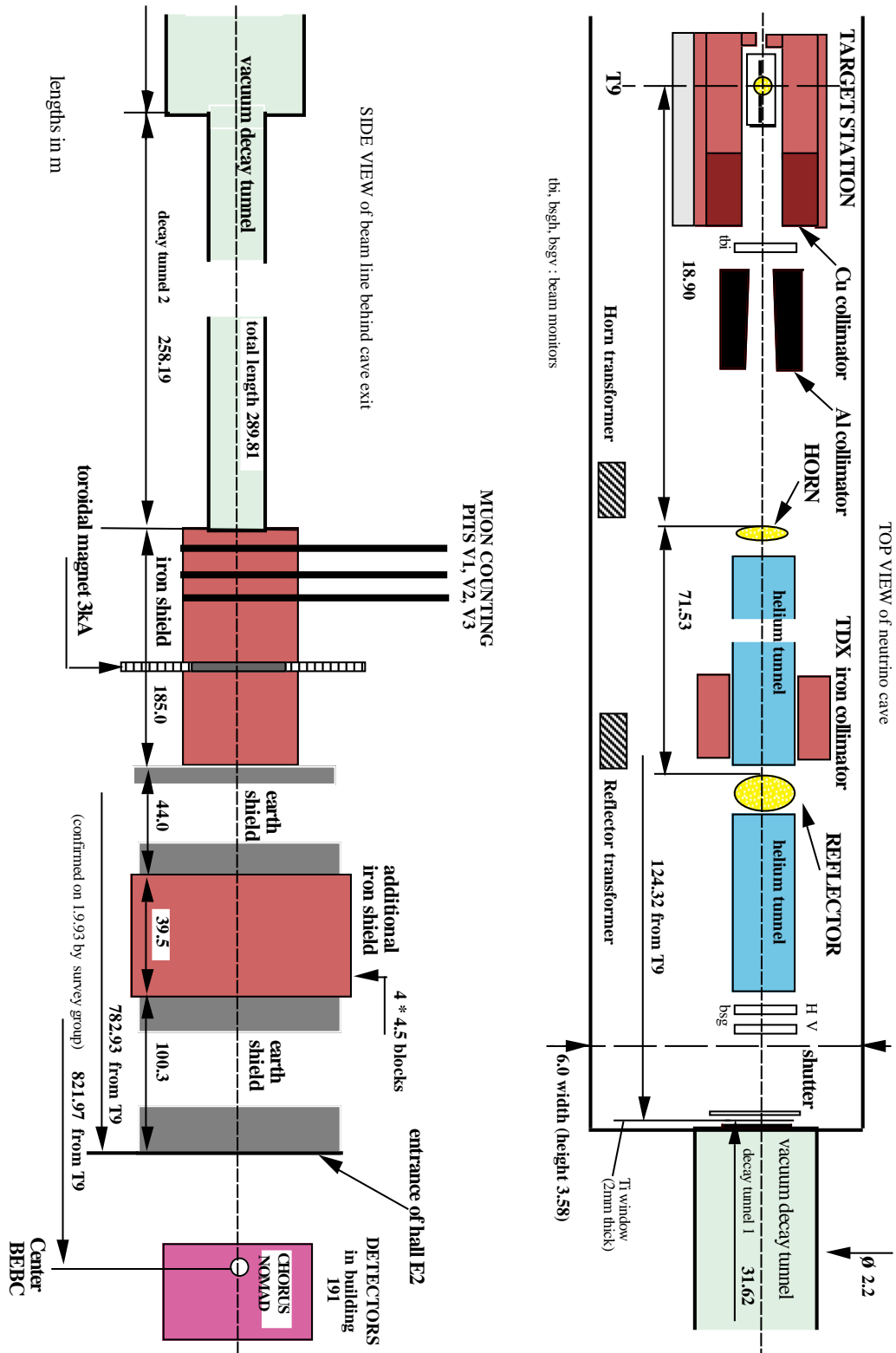
Figure 3.2: Sketch of the CERN WANF beam facility

23

Table 3.1: Compositions of different neutrino types of the CHORUS neutrino beam

neutrino type	relative abundance	$< E > (GeV)$
ν_μ	1	26.9
$\overline{\nu}_\mu$	0.056	21.7
ν_e	0.007	47.9
$\overline{\nu}_e$	0.0017	35.3
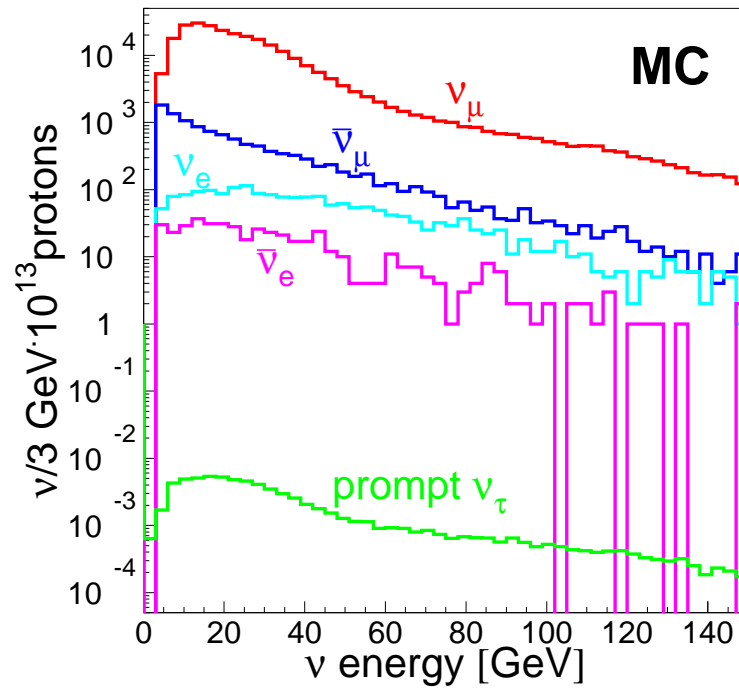
Figure 3.3: Energy spectrum of the CERN SPS beam neutrinos

values for the CHORUS experiment, are obtained with the help of Monte Carlo simulation programs. Beam contamination of ν_τ neutrinos, are estimated to be in the level of $\nu_\tau CC/\nu_\mu CC \sim 3 \times 10^{-6}$ [40] which is a negligible background source for the experiment (~ 0.1 background events for the total CHORUS data taking).

The neutrino beam line at CERN is controlled and monitored with West Area Neutrino Facility (WANF). Protons are accelerated up to 450 GeV/c once every 14.4 seconds. They are extracted in two 6 ms spills. The spills are separated by 2.7 ms. The neutrino beam line has a slope of 42.5 $mrad$ with respect to the horizontal axis of the experiment. The beam line has been refurbished in 1992. Electronics, data acquision and control systems of the neutrino flux monitoring systems were replaced. A new target station was installed.

3.2   Emulsion target

The CHORUS emulsion target consists of 4 emulsion stacks sandwiched with fiber tracker system (see figure 3.4). Each emulsion stack has dimensions of 1418×1468 mm^2 (made of 8 modules each). The modules consist of 36 individual emulsion plates. Emulsion plates are produced with two 350 μm layers, poured to each side of a 90 μm thick plastic sheet. In total, the volume of all emulsion stacks is 206 liters (770 kg of total mass). Each stack contributes approximately one radiation length and 0.08 interaction length. In order to reduce loss of the latent image of the tracks in the emulsion (fading), they are kept at a temperature of $5.0 \pm 0.5\ ^0C$ in a cool box. The relative humidity of the cool box is stabilised at 60%.

Additional thin emulsion sheets are placed between fiber trackers and emulsion stacks, to serve as high accuracy interfaces in between these modules. There is one emulsion sheet which is placed at the downstream side of the emulsion target and it is called "special sheet" (SS). The two "changeable sheets" (CS1 and CS2), are mounted to the two surfaces of honeycomb panel and they are placed near the first fiber tracker module (see figure 3.4). Each sheet consists of two 100 μm thick emulsion layers which are poured onto two faces of 800 μm thick plastic base plate. The thickness of the plastic plate is increased to have better track angle measurement. Special sheets are kept in the target area, during the whole running period while changing CS every three to six weeks. This method is used to decrease the number of background tracks in CS and hence to increase efficiency of finding the right tracks in these sheets.

The alignment between these sheets and the emulsion target is done by 15 X-ray guns per sector which produce 1 mm diameter black dots. The relative alignment between adjacent emulsion layers is realized by the tracks of passing-through muons.

During the neutrino beam exposure, temperature, humidity and background track intensity of the emulsion target are monitored continuously. Background tracks are mainly originating from muons in neutrino beam (which are negligible) and from muons produced by one of the SPS West area test beams which is called "X7" beam. The number of muons from X7 beam is kept under control such that the track density in emulsion, accumulated in two years, is acceptable. Moreover, the same tracks are used for intercalibration of emulsion plates and for distortion

corrections.

3.3   Tracker system

The experiment contains two independent fiber tracker systems. One group of fibre tracker planes (Target Trackers) is used to predict event positions in the emulsion. They are sandwiched between emulsion stacks. The other group of fibre tracker planes is positioned before and after the hexagonal magnet to measure the momentum and charge of low momentum particles. It is the only momentum measurement possible for electrons and hadrons, which all shower in the calorimeter.

Target tracker (TT) planes are made of 500 μm diameter fibres. Each plane is a ribbon of 7 layer fibres which are staggered. One tracker module consists of planes oriented in four projections which are Y, Z and $Y^{\pm}$, $Z^{\pm}$. The latter one rotated by $\pm 8^0$ relative to Y, Z. There are 8 tracker modules which are inserted in between 4 emulsion stacks (see figure 3.4). Tracks reconstructed by these modules are used to predict the position of the event vertex in emulsion and the positions of tracks in changeable sheets. The prediction accuracy is measured using beam muons located at the interface emulsion sheets. The prediction accuracy for isolated minimum-ionising tracks is $\sigma \sim 150 \ \mu m$ in position and $\sim 2.5 \ mrad$ in angle [41].

The diamond shaped magnet tracker (DT) has three tracker modules. These modules have the same fiber diameter and ribbon shape as the target trackers.
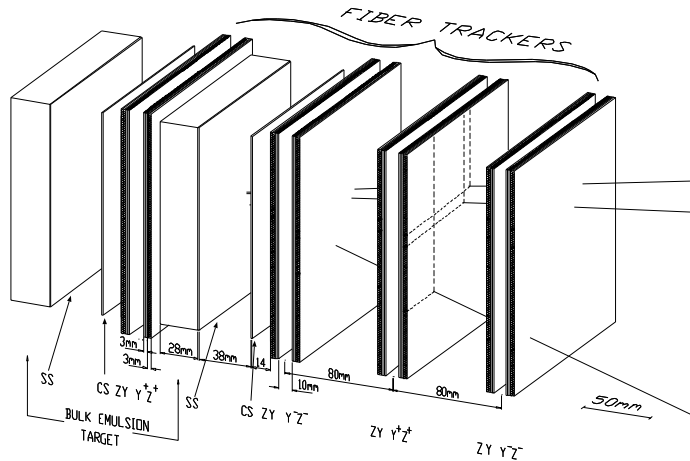
Figure 3.4: Geometric structure of the CHORUS target

One of the modules is placed before and the other two are placed after the hexagonal magnet. Each module consists of two planes rotated by 60^0. Planes are made of 3 individual paddles as shown in figure 3.5. Paddles allow to measure the three coordinates at 120^0 from each other. Both magnet and trackers have the same six-fold symmetry, such that one of the two coordinates measured by each module is in the bending plane. With these properties, the diamond trackers are designed to measure charge and momentum of the particles originating from a neutrino interaction in emulsion.

All fibers in these trackers are read by optoelectronic read-out systems. They consist of image intensifiers and a CCD camera at the end of the intensifier system [42] (see figure 3.5). The net gain of the entire assembly of the image intensifiers, ranges from 10^4 to 10^5 and the net demagnification factor from the

28

fiber bundle input to the CCD surface, is 0.11. Each CCD consists of 550×288 pixels with 16×23 μm^2 dimensions, corresponding to 145×209 μm^2 in the detector space. In order to measure the image distortion and to monitor the performance of the optoelectronic read-out, 45 "fiducial" fibers are coupled to a chain with light input supplied by a computer-controlled LED pulser.

3.4   Hexagonal magnet

The momentum of muons can be measured with a iron toroid spectrometer. The momentum of soft particles which can not penetrate the calorimeter like electrons and hadrons, however, need to be measured with air-core spectrometer. This is needed for detection of tau neutrinos through the non-muonic decay channels of tau. A bending magnet is necessary for this purpose. Such a magnet should have no stray field because of the electrostatic image intensifiers, it should have a restricted length due to the acceptance of the calorimeter and it should have restricted amount of material to minimise multiple scattering. An air-core magnet [43] of hexagonal shape was designed and located between the target region and the calorimeter. It is made of six equilateral triangles with 1.5 m sides, and 0.75 m depth (see figure 3.6). It produces a homogeneous magnetic field parallel to the outher sides and the field strength has no radial dependence. A field of 0.12 T is obtained. The magnet is kept in the 5^0 environment in the cool box and it is pulsed only during the neutrino beam spills.

The performance of the diamond tracker hexagonal magnet system is tested with muons. The muon momentum is measured with the spectrometer with a
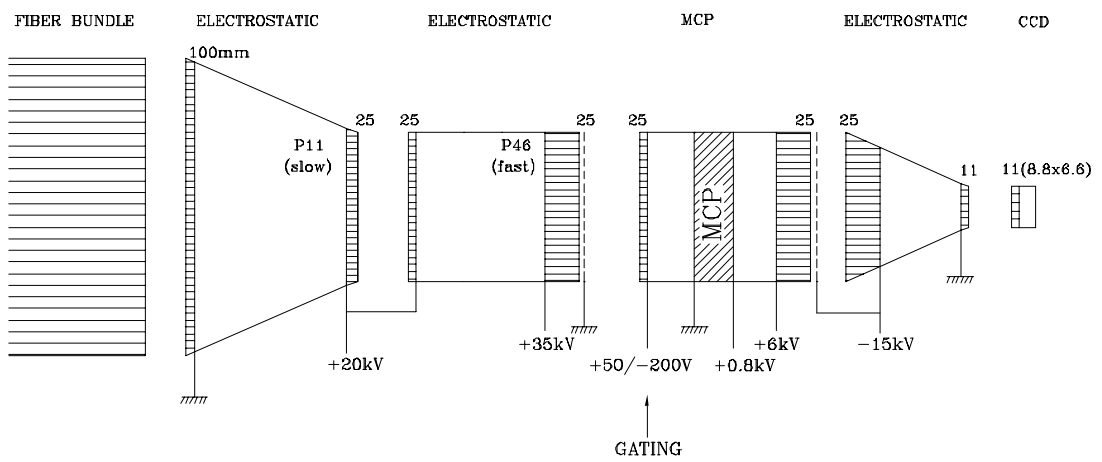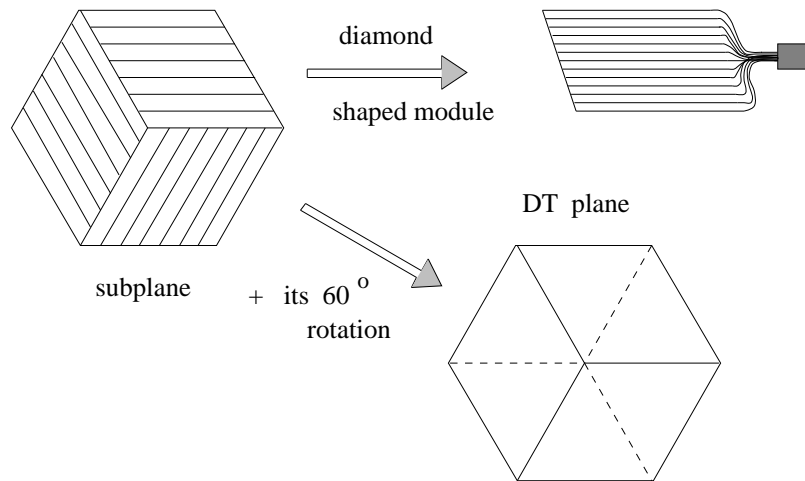
Figure 3.5: Top: Diamond tracker paddle geometry, bottom: sketch of the opto-electronic chain
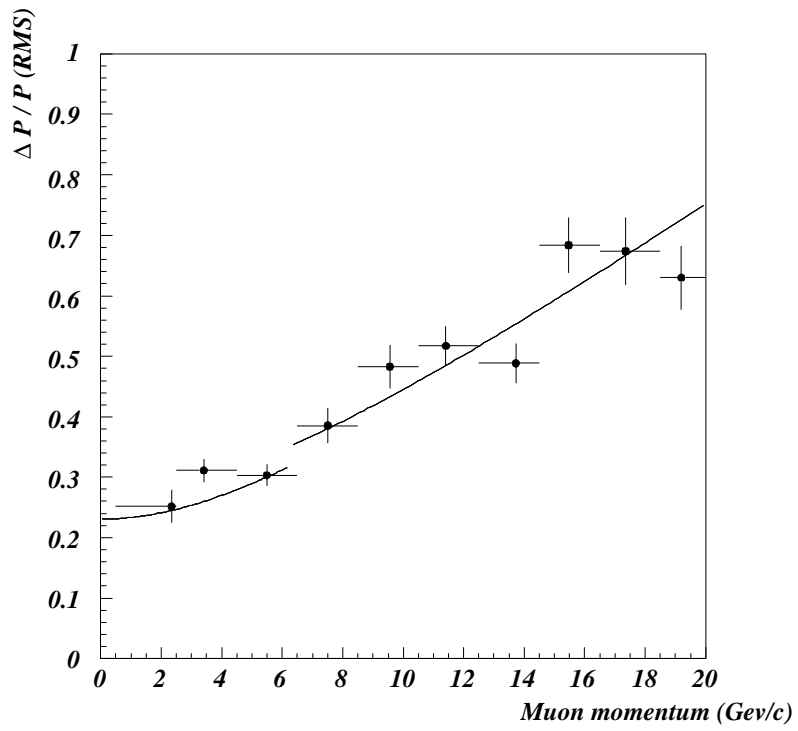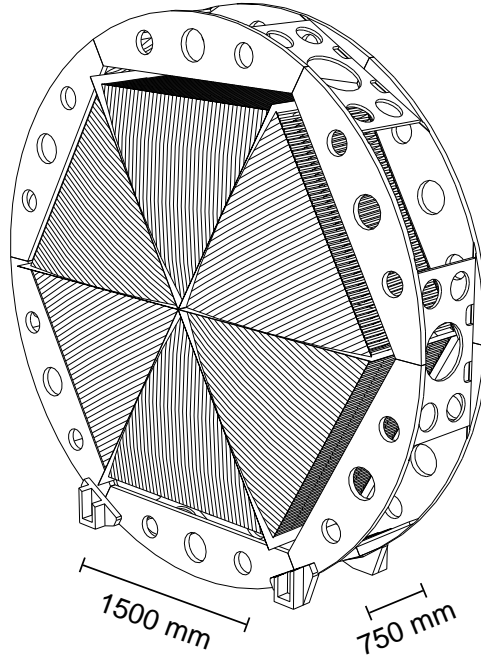
Figure 3.6: Top: Air-core hexagonal magnet, bottom: momentum resolution of diamond tracker hexagonal magnet infrastructure

resolution of $\Delta p/p \sim 7\%$ below 6 GeV/c if the range of stopping muon method is used and with a resolution of $\sim 16.5\%$ above 6 GeV/c if the curvature method is used. For the same muons, the momentum is also measured with DT and a resolution of

$$\frac{\Delta p}{p} = 22\% + 3.5\% \times p \; \frac{GeV}{c} \tag{3.1}$$

is obtained as shown in figure 3.6

3.5 Calorimeter

There are three parts of the calorimeter. They are called the electromagnetic (EM) and the two hadronic (HAD1 and HAD2) parts, named according to the particle type for which they measure the energy. EM has 4 planes, two in horizontal and two in vertical projections (see figure 3.7). Each plane consists of 62 individual modules. HAD1 and HAD2 have 5 planes in both projections. HAD1 planes have 40 modules while HAD2 planes consist of 36. The EM and HAD1 parts are made of lead with 1 mm plastic scintillating fibers interspersed ("spaghetti technique") [44]. The volume ratio of the mixture of lead and plastic is 4:1 for all parts of the calorimeter. The HAD2 part is made of lead and scintillator strips. In total, the calorimeter is 144 radiation lengths and 5.2 interaction lengths. Each individual module is read with two PMTs from each end. A group of streamer tube planes (one horizontal and the other vertical) is inserted behind each second plane of the EM sector and behind each plane of the HAD1 and HAD2 sectors.

32
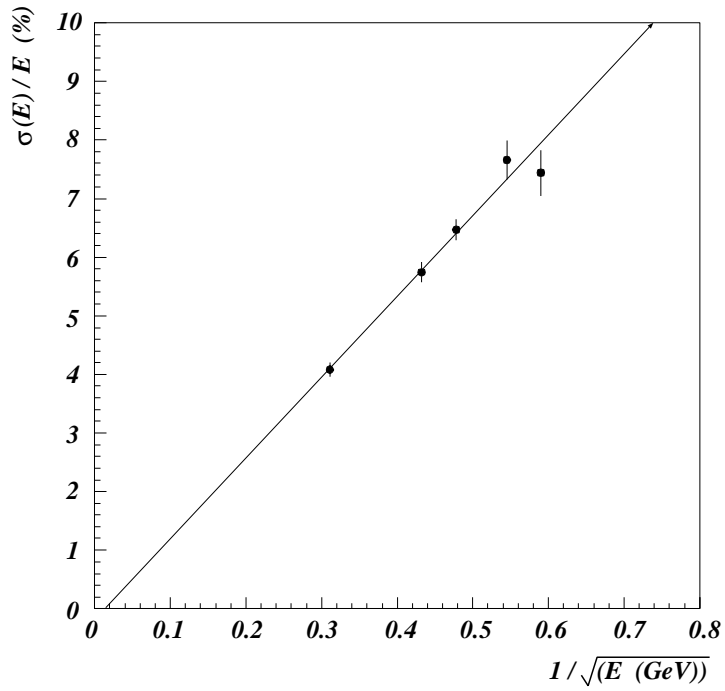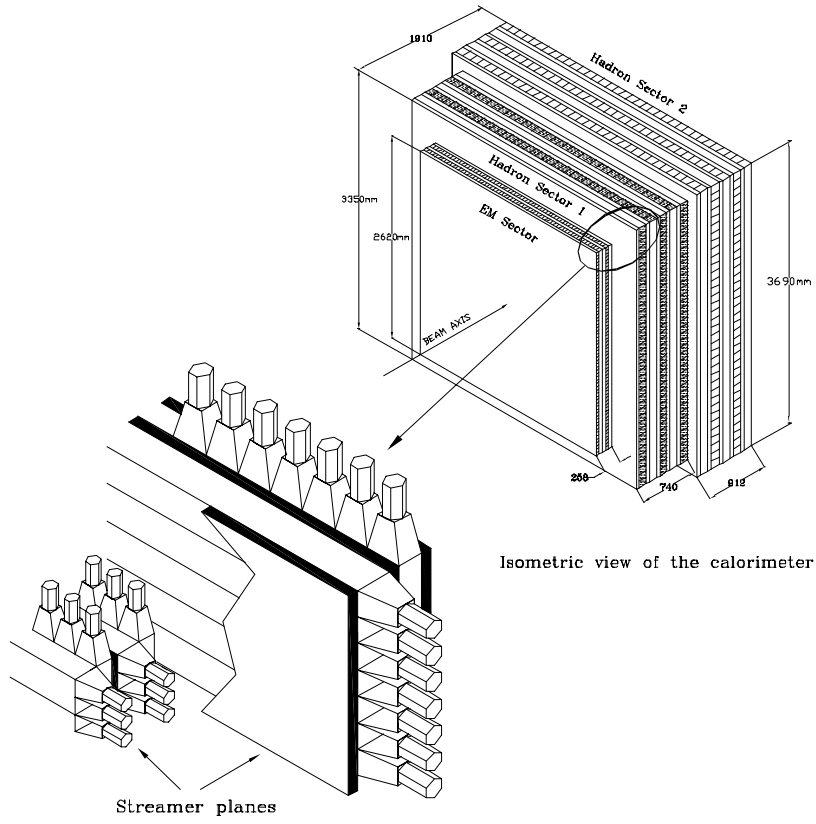
Figure 3.7: Top: Geometric structure of the calorimeter, bottom: energy resolution of the calorimeter for electrons

The response of the calorimeter to electrons and hadrons is tested with test beams of well-defined energy. The energy resolution of electrons is shown in figure 3.7. The following resolution

$$\frac{\sigma(E)}{E} = \frac{(13.8 \pm 0.9)\%}{\sqrt{E(GeV)}} + (-0.2 \pm 0.4)\% \qquad (3.2)$$

is obtained for electrons which is in good agreement with Monte Carlo predictions. A similar procedure was repeated for the response of the calorimeter to pions; and a resolution of

$$\frac{\sigma(E)}{E} = \frac{(32.3 \pm 2.4)\%}{\sqrt{E(GeV)}} + (1.4 \pm 0.7)\% \qquad (3.3)$$

is obtained for pions. Other performance parameters of the calorimeter can be found elsewhere [45].

3.6   Spectrometer

The CHORUS muon spectrometer uses the calorimeter modules of the upgraded CDHS detector [46] which were later used in the CHARM II detector [47]. The main functions of the system are to identify the muons and to measure their charge and momentum. It consists of 6×20 magnetised iron disks of 2.5 cm thickness (see figure 3.8. The iron is magnetised by four water-cooled copper coils. It provides a field of 0.85 Tesla $\cdot$ m per magnet. A current of 700 A is applied with a polarity which focuses (defocuses) negative (positive) muons.

Tracking between the magnets (7 gaps in between 6 magnets), is done by drift chambers and streamer tube chambers. Scintillator strips are sandwiched between

34
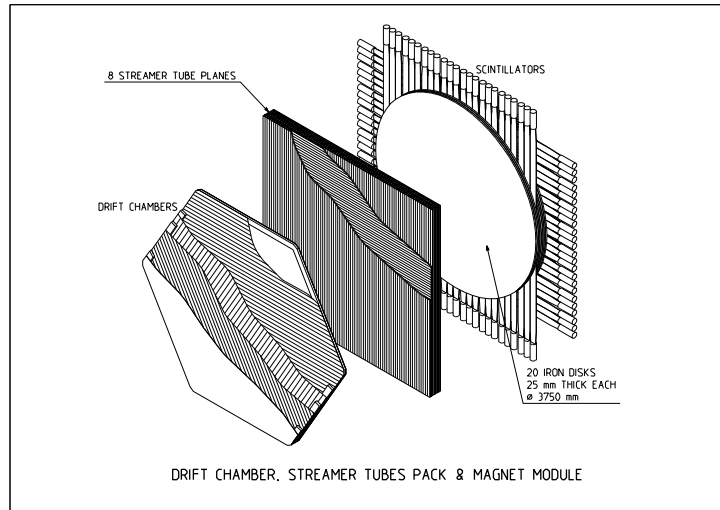
Figure 3.8: Geometric structure of a spectrometer magnet unit

the discs mainly to get a fast signals for triggering purposes and for calorimetry. There are seven drift chambers which are filled with an argon-ethane mixture. Each chamber consists of three hexagonal drift planes oriented at 60^0 with respect to each other. Each of seven drift chambers is followed by eight streamer tube planes. They provide measurement of track segments in each gap and eliminate right-left ambiguities in the corresponding drift chambers. The tubes are operated with argon-isobutane mixture with an additional admixture of water vapour.

The spectrometer has 19% momenta resolution at 71 GeV/c which is measured by test beam muons. At low momenta, the resolution is determined with the help of a Monte Carlo simulation programme.

35
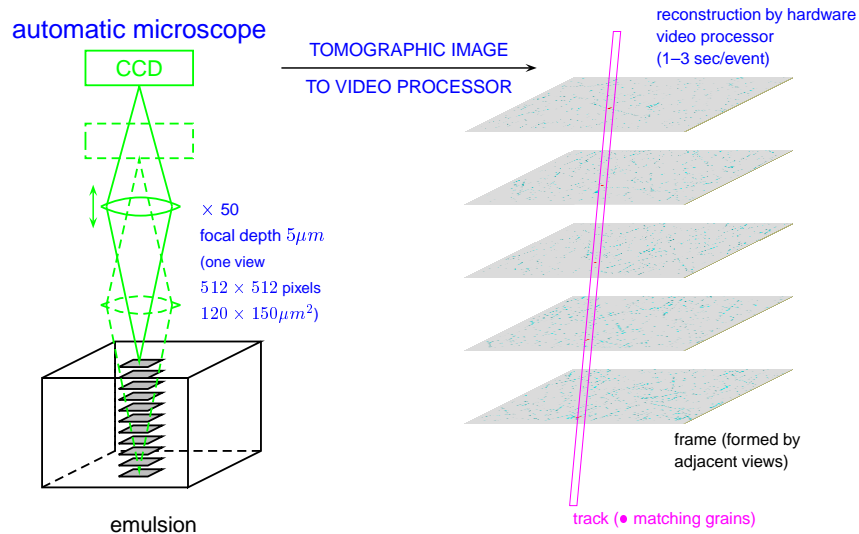
Figure 3.9: Sketch of the automatic emulsion scanning microscope system

3.7 Emulsion scanning

After the exposure of emulsions to the neutrino beam, a process called "emulsion development" starts. Before that, fiducial marks are printed onto the emulsion plates for calibration purposes which are then used during track scanning.

Track scanning is done by automatic [48] and semi-automatic systems which are developed in Nagoya, Japan. These systems are combination of a computer controlled 3D stage movement, a microscope with different magnifications of the objective and a CCD camera to record the microscope view. In both semi-automatic and automatic systems, the microscope stage is controlled by computer and image is recorded by a CCD. However, in the semi-automatic system, tracks are followed by the operator. In the automatic case, 16 digitised pictures

are overlayed in the direction of the predicted track slope and hence tracks are separated from background tracks with this method (see figure 3.9). Picture overlaying and track following is done by an electronic device called "track selector". Standard automatic scanning devices measure one $100 \times 100 \ \mu m$ view in 3 s. This corresponds to a speed of 40 s/track searched. There are even more faster devices available with the capacity of 1000 events/day. R&D is still going on to increase the scanning speed and hence the scanning power.

CHAPTER 4

THE CHORUS TRIGGER SIMULATION

4.1   Trigger hodoscopes

The CHORUS trigger system is designed to detect ν_τ CC interactions occurring in emulsion stacks. It consists of 5 trigger hodoscopes which are made of scintillators (see figure 4.1). These are named E,T,H,V and A according to their position and function. The trigger decision mechanism, is started with the signals obtained from these planes. The decision logic uses information supplied by these planes and by the other sub-detectors.

The details of the emulsion hodoscope plane, called E plane, is left to the following section. T plane is made of two thin ($\sim 6\ mm$ thickness) scintillator planes. The thickness is minimised to avoid loss of tracking precision in fibre trackers due to multiple scattering. For the same reason the planes are mounted as close as possible to the last fibre tracker of the target region. Each T plane is made of 15 thin scintillator strips of 10.2 cm width and 160 cm length, oriented horizontally. The two planes are staggered and cover an area of 160x160 cm^2 with small gaps in between scintillator strips. The reason for strip staggering is to prevent particle hit inefficiency due to the these gaps. Light is detected from each end of the strips with 12 stage photo-multiplier tubes (PMT) which
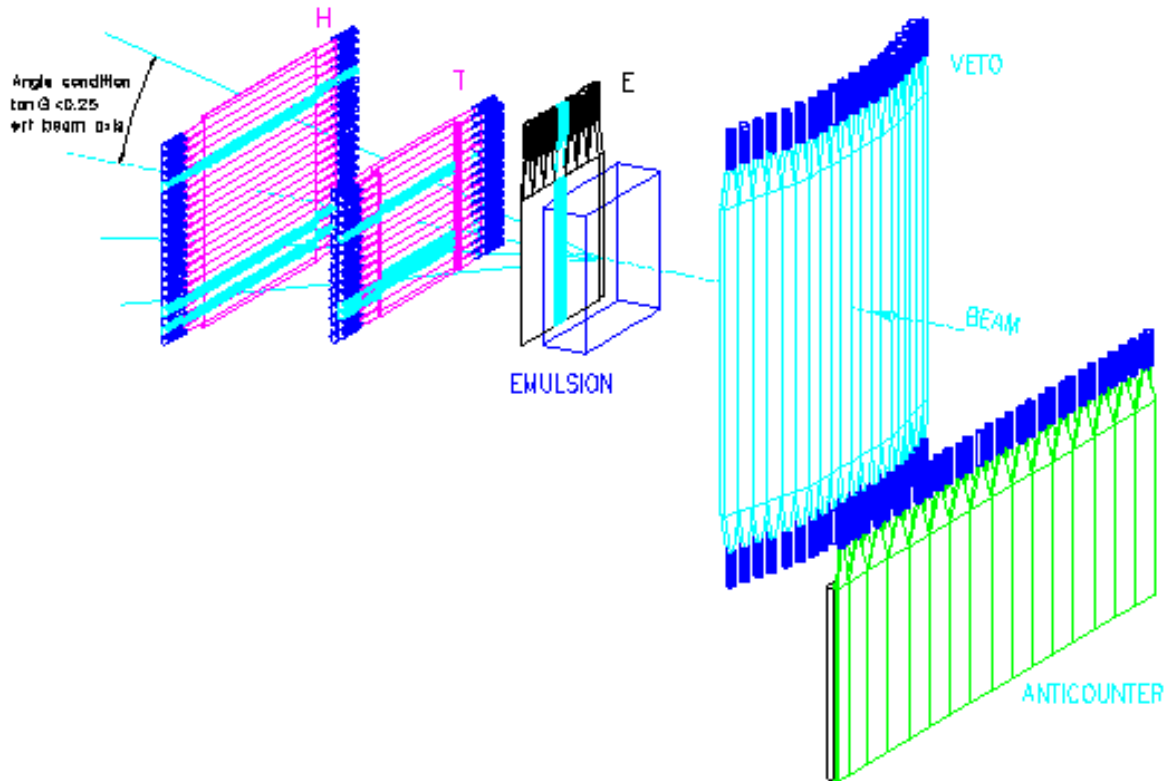
Figure 4.1: Trigger planes of the CHORUS detector

are operated at $\sim 1800\ V$. Specially designed light-guides, which map strip dimensions to a circular surface, are used to collect and transmit the light from strips to the PMTs. The two photo-multiplier signals are mean-timed to ensure strict timing which is then independent of the particle penetration position in the strips. Bicron type BC-408 scintillators are used. They have $\sim 4\ m$ attenuation length with approximately 10 γ/keV light yield.

All the scintillator planes in the trigger set-up, consist of two individual planes

made of thin scintillator strips. Besides T planes, the V plane is also connected to PMTs from both ends for the same reason. The rest of the planes are read from one end only. V plane strips are oriented vertically with respect to the beam direction like A and E planes. They have strip width of 20 cm and 320 cm strip length. The two V planes have 19 and 20 strips repectively and the last 6 strips, at both ends, are placed in a plane with an angle of 13^0 with respect to the neutrino beam to cover the sides of the detector in a better way.

The H plane is oriented like the T plane and the information is combined with this plane to differentiate between the particles coming from neutrino interactions in emulsion and the cosmic particles by using the rough angle determination provided by these planes. If hits on both plane strips are accepted in a cone of ~ 200 $mrad$, most of such cosmic particle tracks are rejected. The H plane has the same strip width as the T plane. However, it has 20 strips and strips are longer, ~ 200 cm. "A" planes, with 16 strips, are used to eliminate neutrino interactions in the heavy concrete base in the beam direction, upstream, below the detector.

The signals from each PMTs in a trigger plane, are timed in with a precision of 2 ns at FWHM (see figure 4.2). Timing and calibration is done at the beginning of each data taking period with a muon beam supplied by the CERN SPS. V and T strict plane timing is also adjusted with the help of the same beam. The veto plane is designed to reject the interactions from beam related muons, however, backscattering particles from neutrino interaction in emulsion, may also veto the event which brings a non-negligable inefficiency to event detection. In order
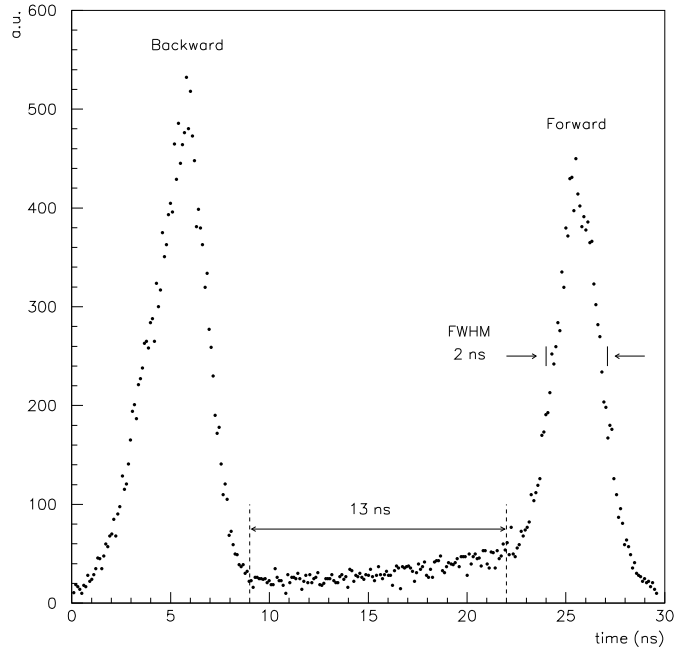
Figure 4.2: T and V planes signal time distribution for forward and backward going particles

to prevent this, T plane signals are taken for reference and veto signals which are delayed by ∼ 10 ns with respect to the timing for forward particles, are not considered. With this logic, the time difference between forward (beam direction) and backward tracks, should be larger than 10 ns. As can bee seen in figure 4.2 the timing is different by 13 ns. Moreover, it should be noted that all of these timing and other properties, are monitored online during data taking.

The main neutrino trigger decision in the experiment, is done in the following way: A hit in the T plane in coincidence with the H plane, satisfying the 200 $mrad$ angle restriction is the main condition. There should be no hit in either of the veto counters V and A. Moreover, strict timing is needed between V and T coincidence for a veto for reasons mentioned above. As last condition, a hit

41

in one of the calorimeter or spectrometer planes is required. All spectrometer and calorimeter planes, except the first electro-magnetic plane of calorimeter, are taken into account. After the E plane installation, the condition of a hit in this plane in coincidence with the T plane hit, is inserted into the main trigger decision. All other trigger properties and decisions are listed in the literature [38, 49].

4.2   Trigger Simulation

The trigger system of the CHORUS detector is designed to handle a certain trigger rate. Increase in the trigger rate is followed by a more than linear increase of the trigger dead time and care has to be taken. The amount of neutrino interactions occurring in a material is directly proportional to the weight of the material and interactions occurring in the emulsion region fully contribute to the trigger rate. Neutrino interactions occurring in heavy materials around the target region, partially contribute to the trigger rate and they are background for the trigger decision. Although the trigger is designed to select events in emulsion and to discard events in materials around the target region, some background trigger rate is unavoidable since materials around are heavy and cannot be far enough away.

Trigger geometry and main trigger decision mechanism of the CHORUS detector, have been simulated to determine the trigger efficiency for tau neutrino interactions in the emulsion and for determining the background trigger rate that can come from the heavy materials around the target region (figure 4.3). The

simulation program has been run for ν_τ and ν_μ charged current (CC) interactions. These are the important processes since the first one is the main interaction studied and the second one forms the main neutrino interaction for the experiment. ν_τ CC events are studied in the target region only, however, to calculate the effect of ν_μ CC interactions on the trigger rate, the interactions occurring in the materials around the target region are studied in detail. The aim of the trigger is to accept $\sim 100\%$ of the interactions by ν CC in the emulsion and to reject as many as possible of the other interactions that can occur around the target region. To study effects of the background interactions on the trigger rate the following procedure has been adopted. Vertices of the interactions are distributed in the heavy materials around the target region. For each vertex position approximately 5000 events have been simulationed. Approximately 50 runs were completed with different vertex positions. For an ideal approach, vertex positions should be distributed everywhere in the detector volume. However, to get enough statistics it would have been necessary to simulate more than 10 million events which is very difficult because of CPU time restrictions. Therefore, some assumptions have been made for the dependence of the trigger rate on position and the simulation program has been executed for optimised vertex positions.

Results obtained from this study are summarised in the table 4.1. The weighted mass is the total mass multiplied by the trigger efficiency at the material position. From the results it can be seen that the total effective mass is 2069 kg. Experimentally, it is known that 0.7 neutrinos interact with matter if 10^{13} protons are dumped on the Be target and if the neutrino target (such as the
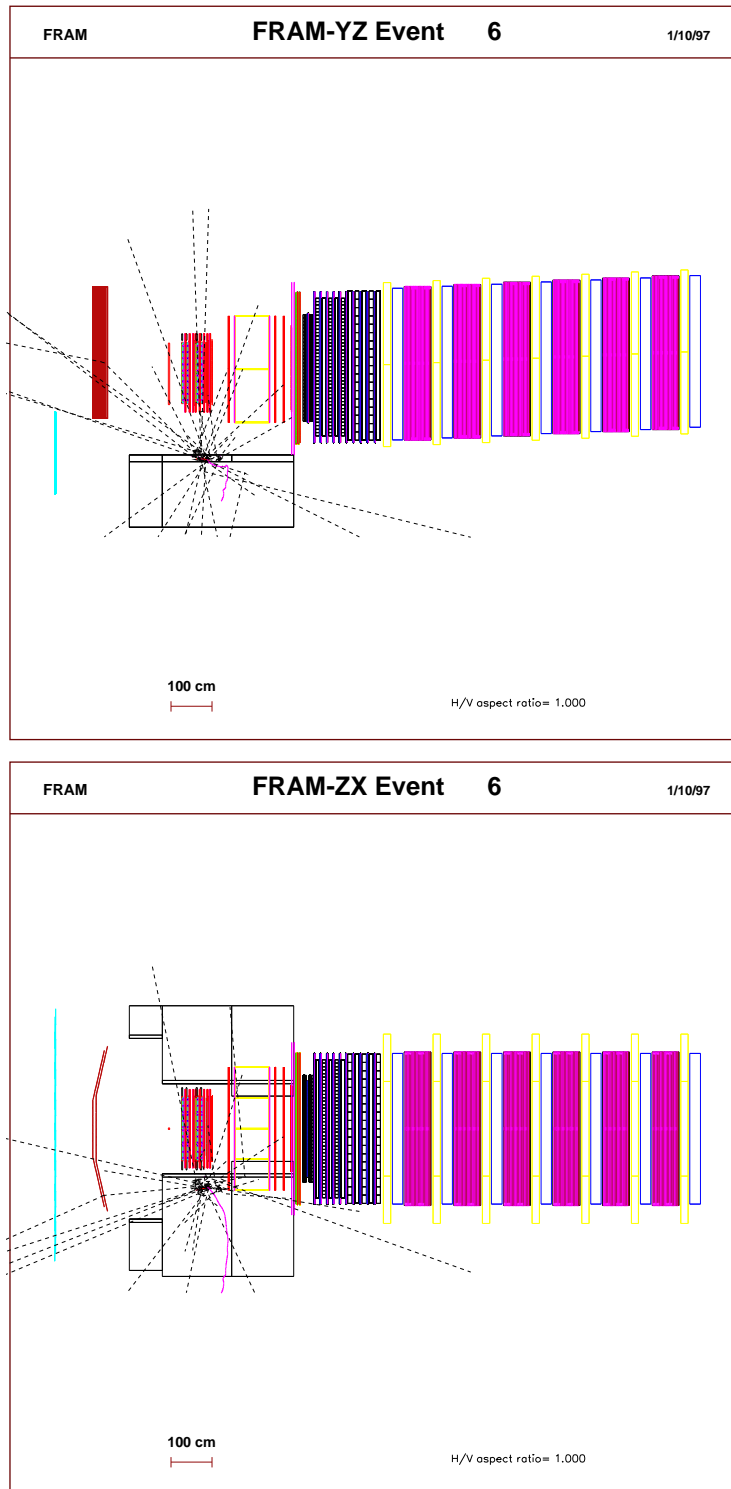
Figure 4.3: A pion interaction in the heavy iron floor under the detector. On top the side view and on the bottom the top view of the detector is shown

Table 4.1: Total mass (T.M.) and weighted masses (W.M.) of the materials around target region

Material Name	T. M. (kg)	W. M. (kg)	Trigger Rate/10^{13} pot
Base iron plates	30 000	530	0.154
Matel frames	104	30	0.009
Concrete blocks	15 000	100	0.029
Cold box material	195	6	0
Tracker scintill.	283	283	0.082
Opto electronic m.	400	20	0.006
Anti counter iron pl.	9000	200	0.058
Veto support	100	100	0.029
Emulsion	800	800	0.232
Total	55882	2069	0.599

emulsion stacks) has a total mass of 2400 kg. With this experimental knowledge it has been calculated that the CHORUS trigger will have 0.6 neutrino interactions per 10^{13} protons on Be target. For the main events that are to be studied in the CHORUS experiment, a 100% trigger efficiency has been estimated with the same simulation programme.

Most of the critical features of the trigger geometry and decision, like the hodoscope condition, is studied also with the simulation program mentioned above. The hodoscope condition with the discrete strip geometry, is tested and 200 $mrad$ angle cut is an optimised value such that almost all neutrino interactions occurring in emulsion are accepted and a reasonable reduction of the rate of cosmic tracks is obtained.

4.3   The Additional Trigger Plane

The E plane was not included in the original trigger design and the detector was operated without this plane in 1994 neutrino data taking. The increase in SPS efficiency and increase in the amount of neutrinos delivered to the CHORUS detector, made it important to decrease the background trigger rate further, to avoid an increase in the trigger dead-time. A new plane, called E plane, was designed and simulated to reduce this background.

To determine the optimum design parameters of the new plane the trigger simulation program was modified. A scintillator plane was introduced into the trigger simulation programme in the position which is technically available in the detector geometry. The programme was run for the same kinds of events of the general trigger simulation. Vertices have been distributed in the emulsion stacks and in the heavy iron material under the target region. Since the complete study was done before, this time only the iron material was studied in detail. As can be seen from table 4.1, this materials constitude approximately 40% to the trigger rate. Reducing this number would solve the main problem. Any hit in this new plane would satisfy the new trigger condition if the old trigger condition was satisfied already. That is, if trigger condition which was valid for 1994 run, is satisfied, the trigger system checks for a hit in the new plane to accept the interaction. Plane dimensions are optimised so that it reduces as much as possible the trigger rate coming from the material of the iron base and keeps the high efficiency for the main trigger occurring in the emulsion target. This
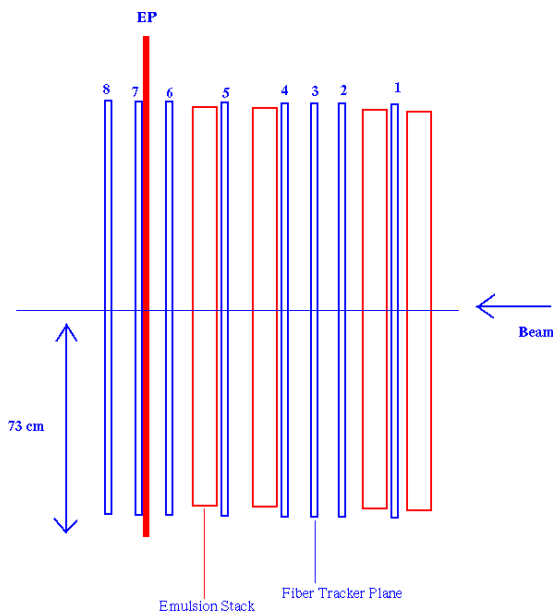
Figure 4.4: E plane positioning in target region

optimisations showed that vertical position of the plane has to be adjusted to the mm level and surface area of the plane had to be kept at a minimum size to avoid trigger rate, coming from the materials close to the target region, such an optoelectronic image intensifier chains. The results obtained with the simulation are compared with the previous trigger simulation and trigger efficiencies are obtained for the same vertex positions.

As optimised design emerged a plane of 7 scintillator strips with 20 cm width, oriented vertically. Only vertical strips were possible due to reasons of space in the detector. It had to be positioned in the emulsion target region with a mm precision (see figure 4.4). With these conditions a 33% reduction in the background trigger rate has been estimated. two-third of the 33% reduction is estimated to come from the heavy iron base. It is also shown that the main (ν_τ

47

) interactions occurring in emulsion target are not effected by the new trigger set-up.

The mechanical structure of the plane can be seen in figure 4.5. The plane consists of a support structure, scintillator planes, light guides, PMs, PM base electronics and electronic structure that shapes the PM signals and make logic signals. The detailed structure of the electronic set-up is shown in figure 4.6. Responsibilities on the construction of the materials and of financing have been shared by the collaborators as listed in table 4.2.

Table 4.2: Production places for the E plane components

Component	Produced by
Mechanical design	CERN
Supporting structure + Scintillator strips + Gluing + Wrapping + Flasher boxes + Fibres	NIKHEF
Light guides	METU
Cabling	CERN
Project leader, Electronic structure and Commissioning	Erhan Pesen

When run 1995 started, the E plane was tested before implementing to trigger logic. From these tests it has been found that a 32% reduction of the trigger rate coming from background, was achieved. In addition, it did not bring any inefficiency to the events studied in the CHORUS detector. Data was taken for
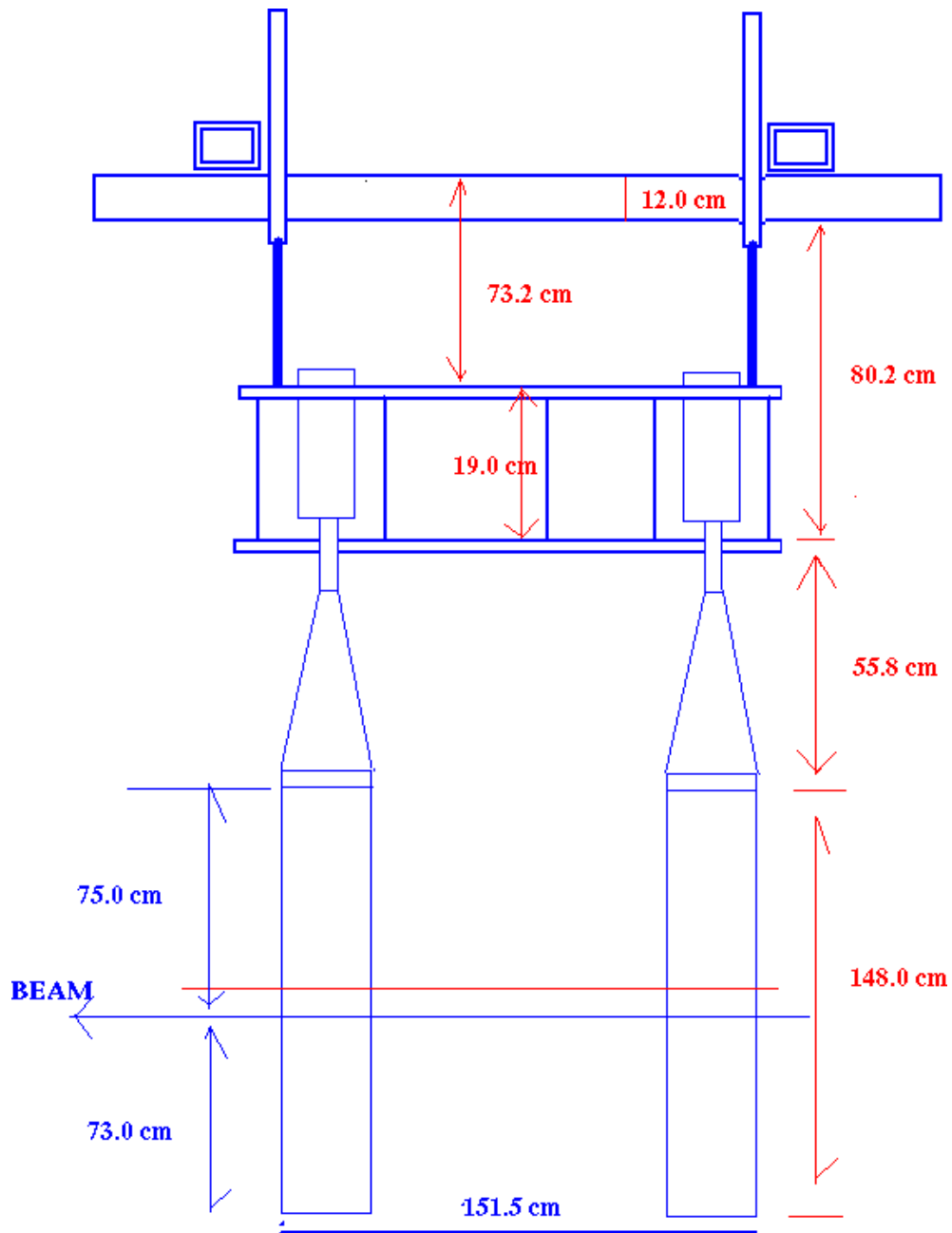
Figure 4.5: Mechanical structure of the E plane

Figure 4.6: Electronic structure of the E plane

a while in a test position in the trigger logic. The data obtained have been used to extract E plane parameters. Tracks that were found in the target trackers are extrapolated to veto and T planes. If they hit these two planes, the position where the track is hitting the E plane is calculated. Then the signals from the E plane were checked to see whether the hit of that strip of the plane was recorded. With this analysis programme, the E plane position has been checked with data and compared with the design parameters. A ∼ 100% match with the design parameters was obtained. Moreover, the efficiency of the E plane was checked with a similar method. Tracks are extrapolated and hits on the plane are examined. It has been shown that each strip has approximately 99.9% efficiency in recording minimum ionising particles (MIP) passing through the strip.

As a final step, all events rejected with the E plane logic were examined with an eye scan for a full run (appr. 500 events). No proper event occurring in the emulsion region is rejected. It is found that the total reduction of the background trigger rate was 32%. Interactions occurring in heavy iron base, are reduced at the 20% level. The rest of the reduction , which is 12%, is from the background trigger rate due to the neutrino interactions around the target region like image intensifiers of fiber trackers. In the 1995 data taking period, 10^{13} protons per spill, are delivered to the berilium target to produce neutrino beam. With the new trigger plane, no dead-time problem occurred and more neutrino CC interaction (∼ 200000) could be recorded on tape. Data taking periods are compared in figure 4.7.

CHORUS RUN SUMMARY 94/95

SCHEDULE, POTS and POTS ON TAPE 94/95

Run summary chart plotting PROTONS ON TARGET 10^{16} versus DAYS (124–624), showing SCHEDULE (green), POTS (blue), and POTS ON TAPE (red), with CHORUS PROPOSAL (94+95) at 2400.

- SCHEDULE: 3.38×10^{19}
- POTS: 2.01×10^{19}
- POTS ON TAPE: 1.68×10^{19}
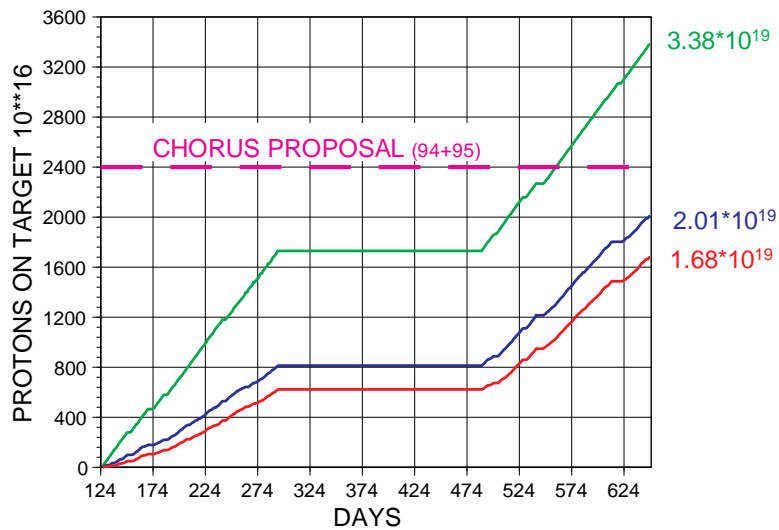
Emul. in	Emul. out	Emul. in	Emul. out
5.May 94	21.Oct. 94	4.May 95	11.Oct. 95

	1994	1995
SPS EFFICIENCY:	47 %	72 %
CHORUS EFFICIENCY:	77 %	88 %
MAIN TRIGGERS:	400 000	547 000
RECORDED CC EVENTS:	$\approx$ 120 000	$\approx$ 200 000

Ch.Weinheimer, Oct.95

Figure 4.7: Run statistics and detector efficiency

52

CHAPTER 5

DETECTION OF TAU NEUTRINO WITH $\tau \to e^- \nu_\tau \overline{\nu}_e$ DECAY CHANNEL

Detection methods of tau neutrino via three decay channels in the CHORUS experiment, are explained in detail in the experiment proposal [32]. For all the channels considered in the proposal, the analysis strategy can be shown to have three main parts. These are event selection, finding these events in emulsion stacks and identifying an event by studying kinematical properties of the particles originating from the neutrino interaction.

Studying kinematical properties of the electrons from the tau decay with the CHORUS experimental set-up, is rather difficult due the interactions of electrons in the emulsion stacks. The CHORUS experiment has four emulsion stacks and each emulsion stack approximately corresponds to one radiation length. This fact makes it difficult to study kinematical properties of the electrons originating from the tau decay. The efficiency of finding the tau to electron decay events in emulsion, however, is expected to be close to the efficiency of finding the other tau decay events once the electron from tau decay, has reached the calorimeter without showering.

The only difference of the electron decay channel from other decay channels is

the presence of the electron in the event. In some cases this electron is lost due to showering in the emulsion stacks. The fact that electrons are not easily selected, makes it very difficult to separate these events from other non-muonic tau decays which are studied in the experiment. Therefore, they are automatically selected.

The last stage of the analysis, after selecting and finding the events in the emulsion, one has to identify these events by studying the kinematical properties. In order to achieve this, the electron has to be identified first, and its charge has to be determined. Then by studying the kinematical properties of the events, they can be separated from the background. The most challenging item of this analysis, is to identify electrons by the calorimeter and to find a way of eliminating the background events that can come from the CC interactions of ν_μ with the charm production if the percentage of wrong charge measurement is high. Details of the background sources will be explained in chapter 5. Finally, possible contribution to the calculation of oscillation parameters, is considered. In the following sections the details of the analysis steps will be presented and discussed.

Unless it is noted, in most of the analysis steps, events which are under study, are generated with the event generator program of the CHORUS, called JETTA, version 1.01/51. JETTA uses neutrino beam files generated by GBEAM which takes into account CERN SPS Wide band neutrino beam production structure and energy spectrum. Generated events are simulated by EFICASS version 1.10/24. EFICASS has all the geometric and material properties of the CHORUS detector. Finally, the standard CHORUS analysis program, called CHORAL, version 2.15/13, is used to obtain necessary parts of the general analysis, like

calorimeter shower energy calculations, etc. CHORAL is capable of analysing both simulation and real data in the same way. A program called TAUE is written to analyse and interpret the results obtained from all the programs mentioned. All the errors used are statistical errors unless otherwise stated.

5.1 Tau neutrino interaction in emulsion

The short decay track of the tau particle with decay kink attached, is taken as a visual sign of the tau neutrino interaction. A sketch of the topology of the tau neutrino interaction in emulsion is shown in figure 5.1.a. The figure is drawn for the single prong decay case of the tau lepton. The mean track length of the tau track is of the order of 1.5 mm for the energy range of the experiment (figure 5.1.b). There are two vertices, namely the neutrino interaction vertex (primary) and the kink or decay (secondary) vertex. Primary vertices are associated with heavy nuclear fragment tracks originating from the nuclear break-up due to lepton-nucleon interaction. These tracks are called black tracks. High energetic charged hadron tracks exist in the hadron shower which may be attached to the primary vertex. The visual identification method suppresses most of the background that are partly unavoidable for counter experiments [50].

The position of tracks inside the interface emulsion sheets (changeable CS and special sheets SS) and the vertex position, are predicted with the fibre tracker system. Search of all events in the emulsion is not feasible due to time constraints. Tracks are followed down to the neutrino interaction vertex with automatic scanning microscopes which are specially developed for this purpose. These tracks are
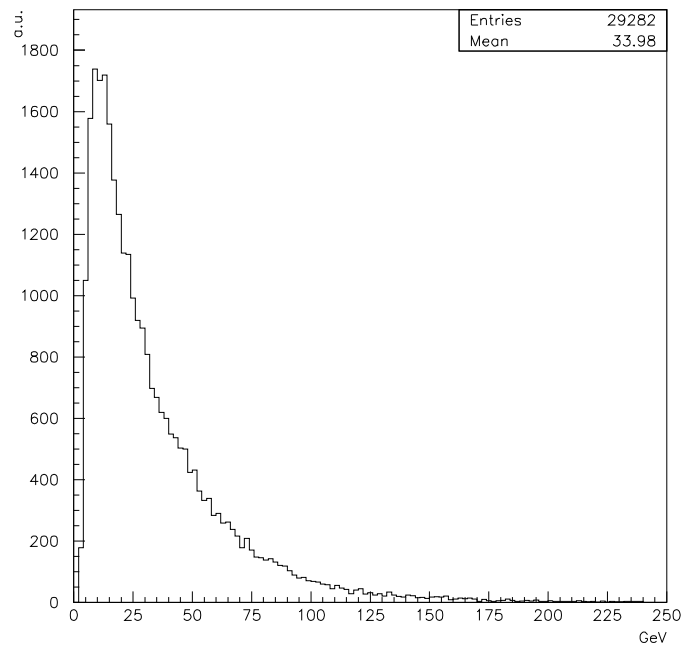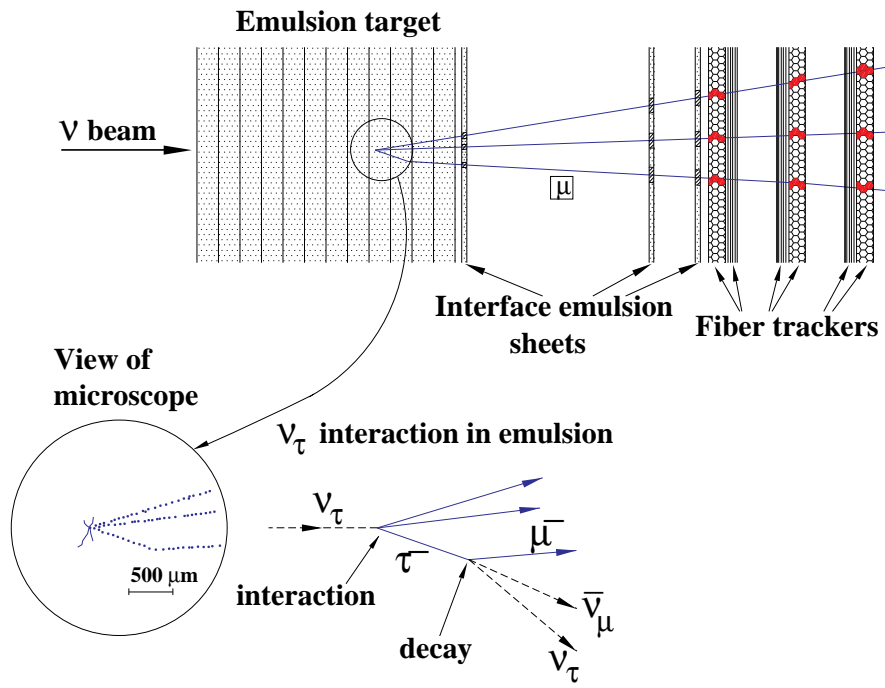
Figure 5.1: a) Sketch of a tau neutrino interaction in the emulsion. b) Energy distribution of the tau lepton

called scan-back tracks. The search for a decay kink on the scan-back tracks (kink search), is started after the vertex location. The grains in the emulsion have a size of 1 μm enabling high resolution spatial of the track location. The automatic scanning technique has an angular resolution of 10 $mrad$ while semi-automatic system has 6 $mrad$ angular resolution depending on the procedure used. Properties of the emulsion, are explained in detail in the CHORUS detector chapter.

5.2 Trigger Efficiency

The online event selection efficiency of the CHORUS trigger system for the electron decay channel of ν_τ CC interactions, has been studied in detail by simulating these events. It is difficult to obtain this parameter Experimentally since events are rejected if the trigger condition is not satisfied. The simulation of the main trigger condition for neutrino interactions reproduces well the rate observed as discussed in detail in previous chapters. Similarly, one obtains also agreement for calculations including E-plane which indicates reliability of the trigger simulation.

CC interactions of the ν_τ with the tau decaying with $\tau^- \rightarrow e^- \nu_\tau \bar{\nu}_e$ channel, are placed randomly inside the target. In this case the target is the 4th emulsion stack since the analysis is based on electron identification by the calorimeter and charge identification by the hexagonal-magnet and diamond tracker spectrometer. Interaction of electrons in other emulsion stacks gives low identification efficiencies as mentioned before. The same exercise is repeated for the main background forming neutrino interaction events. The output of these simulation programs

57

is analysed by CHORAL. Events are reconstructed and the trigger condition is checked by considering the hits in the trigger planes. Contribution of veto plane to the trigger condition due to the back-scattering particles from the event vertex, is considered to be negligible. In the experiment, vetoes from these particles are prevented by strict V-T plane signal timing. All the strips in the trigger planes are 99.9% efficient for detection of the hits. Trigger plane efficiencies are continuously monitored. Each trigger plane consists of two adjacent planes with staggered strips to minimise the inefficiency coming from the gaps between scintillator strips. The last trigger condition, a hit in the calorimeter planes (except first electromagnetic plane) or a hit in the spectrometer planes, is also imposed. Trigger efficiencies for the ν_τ CC interactions and for the possible background events are presented in Table 5.6. As can be seen from the table, the CHORUS trigger system has 99% efficiency for CC neutrino interactions in the emulsion target.

5.3   Vertex Reconstruction

Only events only with vertices reconstructed inside the emulsion stack are sent to emulsion laboratories for scanning. Target tracker tracks are combined with each other to produce a vertex, using the detector information attached to the reconstructed tracks. ν_τ CC interactions events with decays in the $\tau^- \rightarrow e^- \nu_\tau \bar{\nu}_e$ channel are simulated to extract vertex reconstruction efficiencies for these events and for background events. Inefficiencies occur due to the choice of wrong track combinations and including a wrong vertex reconstruction. Thus some vertices

can be predicted outside of the emulsion stack which will remove these events from scanning. Then even if the predicted vertex is in the stack, it may not be found during scanning when the predicted position is far from the real vertex position.

Simulated events are processed and their vertices are reconstructed by target tracker algorithms in CHORAL. Also prediction efficiencies of vertices for different kinds of neutrino interactions are summarised in table 5.6.

5.4   Event Selection

Electron identification is required In order to be able to select or eliminate electron events for emulsion scanning. In the beam direction there are four emulsion stacks sandwiched with fibre trackers downstream of the detector. Most of the electronic part of the detector is downstream of emulsion stacks. Thus the problem of electron identification, can be discussed in two parts depending on the vertex position of the event in the emulsion stacks.

In the case of having the vertex of the electron event in one of the first three emulsion stacks, the probability of losing the electron due to energy loss by the bremstrahlung mechanism is maximised. Electrons have to traverse at least a full emulsion stack (2.57 cm) corresponding to one radiation length. Although the electron showers in emulsion, it is, in some cases, possible to measure a part of the electromagnetic shower with the calorimeter. However, this effect is not sufficient to differentiate electron events from the hadronic events. Electrons coming from $\pi^0 \rightarrow \gamma\gamma \rightarrow e^- e^+$ interactions, are enough to account for the most of this effect.

For events with vertices in the fourth emulsion stack, depending on position of the vertex inside stack, there is a chance for electrons not to shower in emulsion. This number can be estimated to be 63% simply by considering radiation length with the assumption of a uniform vertex distribution. Event selection by the detection these electrons, can be used in principle. Pair production electrons from the neutrino interaction vertex decrease the event selection efficiency with this method. As a result, the efficiency of selecting electron events averaged over vertices in all emulsion stacks, is low due to gamma background coming from π^0 production at the (ν_μ) interaction vertex. However, electron identification in the calorimeter can be used to define a sample of events with an enhanced number of tau to electron decay events.

The tau neutrino CC interaction in the 4th emulsion stack with electronic decay channel, has similar kinematical characteristics as the events with the hadronic decays. Separation of these events from the hadronic kink events is difficult. They will therefore be present in the hadronic sample unless electron-hadron separation is applied to separate the channels.

Event selection efficiency of non-muonic decay channels of the tau (including electrons) is studied and events have been scanned. For non-muonic decay channels, altogether $88.6 \pm 0.5\%$ of the decay modes, these events are selected for scanning [51]. A simulation is used to determine the selection efficiency for tau to electron decay channel events. As expected from the discussion above, the result is not very different from the one for non-muonic decay channels. Thus

an event selection efficiency of $82.3 \pm 0.6\%$ is obtained. The details of the selection procedure and the calculation of the efficiency of selecting $\tau \to e$ events are discussed in the following sections, together with the results for the background contamination.

5.5   Track scanning in emulsion

Event search in emulsion stacks can be performed after the event reconstruction in the electronic part of the detector. Vertex and track information is sent to emulsion laboratories for events satisfying the selection criteria. Track energy, momentum, particle type and charge information is attached if available. Moreover, global kinematic parameters like visible energy, missing transverse momentum are also available with the event.

Track and vertex search in the emulsion is carried out with semi-automatic and automatic scanning microscopes as explained in previous chapters. Track scanning methods for non-muonic tau decay events, are in the development phase and still being improved. For this analysis, all negative tracks which are attached to the reconstructed vertex are chosen if their momentum are in the $1 \leq P \leq$ 20 GeV/c range, if they have spatial angle of $\theta \leq 0.4$ rad with respect to the beam direction and if their angles with respect to the $X7$ test beam satisfy $\theta_{X7} \geq$ 0.05 rad. Tracks are searched in changeable sheets (CS1 and CS2) and in the special sheet (SS) first. If the track is found, the event vertex is searched in the target emulsion (4th emulsion stack for this study) using the better position information supplied by CS and SS. Scan-back tracks are classified into seven

categories (track priority) for emulsion scanning. These are:

1. Tracks extrapolated from the spectrometer, diamond tracker and target tracker with space angle $\theta < 0.2\ rad$ with respect to the beam direction.

2. Tracks extrapolated from the spectrometer, diamond tracker and target tracker with space angle $0.2 < \theta < 0.4\ rad$.

3. Tracks extrapolated from the diamond tracker and target tracker or spectrometer and the target tracker with space angle $\theta < 0.2\ rad$.

4. Tracks extrapolated from the diamond tracker and target tracker or spectrometer and the target tracker with spatial angle $0.2 < \theta < 0.4\ rad$.

5. Target tracker tracks with space angle $\theta < 0.2\ rad$.

6. Target tracker tracks with space angle $0.2 < \theta < 0.4\ rad$.

7. Bad isolation ($isol < 2$), high χ^2 probability ($\chi^2 > 0.7$) of the straight line fit, big space angle ($\theta > 0.4\ rad$) with respect to the beam direction and cut on space angle with respect to $X7$ beam ($\theta_{X7} < 0.08\ rad$).

Space angle, isolation parameters and angular distance of tracks from $X7$ beam are defined as:

$$\theta = \sqrt{\theta_y^2 + (\theta_z - 0.042)^2} \tag{5.1}$$

$$I = \sqrt{I_y\ I_z} \tag{5.2}$$

$$\theta_{X7} = \sqrt{(\theta_y + 0.08)^2 + \theta_z^2} \tag{5.3}$$

62

where θ_y (θ_z) is the angle of the track with respect to the y (z) axis, I_y (I_z) is the number of isolated clusters in y (z) projection used for the track and $0.042\,rad$ is the ν beam angle with respect to the x axis of the detector coordinate system. If many tracks fall into the same category, another priority is defined by the following formula.

$$P = \frac{\theta}{I\,\theta_{X7}} \tag{5.4}$$

Tracks with small P values, will have higher priority for scanning. A full detector simulation used to understand the track priority for electron tracks originating from the tau decay. The results are obtained if the trigger condition is satisfied, the vertex is reconstructed and if the event passed the kinematical selection criteria. For the events passing these selection criteria, $\sim 50\%$ of the electron tracks can be scanned ($\sim 52\%$ for all non-muonic tracks). The track priority is 3 or 4 since spectrometer information is not available for electrons. For the events, which are taken in 1994 running period, tracks with priority 7, are also scanned to deduce scanning efficiency for these tracks.

Since data for electron tracks originating from the tau lepton are not yet available, those which are selected from the scanned tracks, are used to determine the scanning efficiencies for these tracks. The efficiencies are compared with those of all other non-muonic tracks. Since scanning methods are still being developed, it should be mentioned that the values of the efficiencies are preliminary. The results are summarised in table 5.1. The important conclusion can be drawn that scanning efficiencies in CS and SS for electron tracks, are similar to the other

non-muonic tracks.

Table 5.1: Scanning efficiencies for electron and all non-muonic tracks in different emulsion plates

Track type	Efficiencies		
	CS	SS	Total
electron tracks	0.54	0.71	0.38
all non-muonic tracks	0.57	0.79	0.45

Simulation of $\tau \rightarrow e$ events show that $63.8 \pm 1.8\%$ of the electrons from the tau decays, will be selected as scan-back track.

The search for kink starts after the vertex has been located. This method is also in development phase. If a scan-back track is lost in subsequent emulsion plates, it is flagged as kink daughter track candidate. At the moment events are classified into two categories. These are events with short decay length and events with long decay length. The latter is also split into two other categories. If the vertex and decay kink are in the same emulsion plate, events are classified in the short decay length sample. If the vertex and decay are in different emulsion plates, they are put in the long decay length class. All these categories have different scanning and kink location efficiencies depending on the method and technique, used. A detailed discussion of the kink finding efficiency is out of the scope of this study, however, it was checked that it is similar for electron and hadron decay channels of tau.

The formula used to express the kink finding efficiency is,

$$\varepsilon_{kink} = \varepsilon_{P_T} \ \varepsilon_{loc} \ \varepsilon_{s,l} \tag{5.5}$$

where ε_{P_T} is the efficiency of having events with $P_T \geq 250 \ MeV$ kink daughter transverse momentum, ε_{loc} is the efficiency of having events with a decay length of at least 20 μm and shorter than 6 emulsion plate thickness ($\sim 4800 \mu m$) and $\varepsilon_{s,l}$ is the scanning efficiency of the short and long decays respectively.

The values ε_{P_T} and ε_{loc} is tested with simulated electronic tau decay events. For the hadronic decay channel of the tau, $\varepsilon_{Pt} = 63.5\%$, similar to the value of 65.5% for the electronic decay channel. The electronic decay channel has a value of 92.2% for ε_{loc} while the hadronic decay channel has a value 89.5%. These considerations show that assumption of having similar kink finding efficiencies ($\sim 26\%$) for the hadronic and electronic decay channels of tau is reasonable. A complete kink finding efficiency can only be determined after all events have been scanned, since the scanning methods and techniques evolve during the process, and instrumental effects of the scanning stages play an important role.

5.6   Track Matching

Once the kink daughter track is found in the emulsion, the matching of this track can be studied with the tracks found in the target trackers in order to study properties of the event such as track multiplicity. The kink daughter track information is obtained from a simulation as it would be obtained from the emulsion and this information is used for track matching in the target tracker region. For the scope of the study, it is accurate enough to obtain the track information from the simulation rather than from the emulsion.

A cone is defined around the track as follows: the difference between track
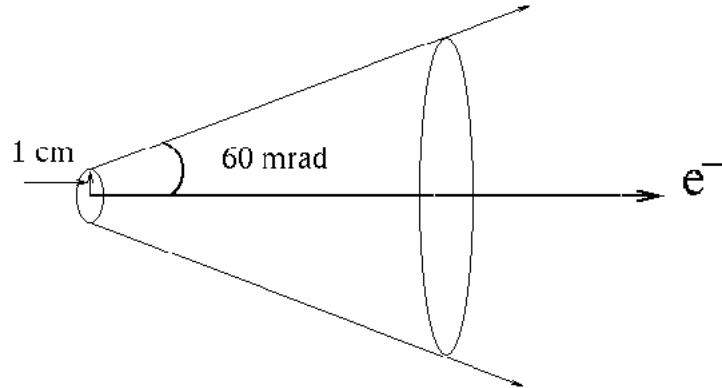
Figure 5.2: Cone definition around the kink daughter track in the target tracker region

angle of the candidate and daughter tracks should be smaller than 60 $mrad$ and the distance of the candidate track to the kink daughter extrapolated to the kink position, should be smaller than 1 cm. These definitions are explained in figure 5.2.

Simulated ν_τ CC interactions with the τ decaying with $\tau \rightarrow e^- \overline{\nu}_e \nu_\tau$ channel, are used to study and optimise the two parameters, cone angle and cone radius. Monte Carlo (MC) track information for kink daughter electrons are used for track matching in CHORAL treating it as information coming from the emulsion measurement. Simulated events are selected and used if the following conditions are satisfied:

- the main neutrino interaction trigger.

- vertex reconstructed in the 4th emulsion stack.

66

- accepted by non-muonic tau decay event selection criteria.

- existence of a single track in the cone.

- track reconstructed inside the acceptance of the calorimeter.

- single hexagonal magnet triangle is traversed.

These conditions are used for $\tau \to e^- \overline{\nu}_e \nu_\tau$ decay events selected with these criteria show a Gaussian distribution for the differences between the reconstructed and true angle and position of the tracks shown in figure 5.3 and figure 5.4. These studies show ~ 2.6 $mrad$ resolution in both projections for the angle matching and ~ 310 μm resolution for the position matching in both projections at CS. The track multiplicity in the cone, defined above, is another important parameter and the requirement of a single track in the cone has a 57% inefficiency for the $\tau \to e^- \overline{\nu}_e \nu_\tau$ decay channel (figure 5.5). However, as mentioned earlier, it is necessary to overcome the showering problem of the electrons coming from the τ decay.

The same analysis has been done for events obtained in the neutrino beam in 1994. Only the events with vertex reconstructed in 4th stack are taken. With the help of the electron identification program which uses the calorimeter information, tracks obtained from the scanning, are flagged in the same way as simulated electron tracks. Moreover, it is imposed that the momentum was reconstructed in the diamond tracker. In figure 5.6 similar distribution for the cone angles are shown for the events obtained in the beam. A Gaussian behaviour is observed. This was expected since almost equivalent cuts are applied to these tracks using
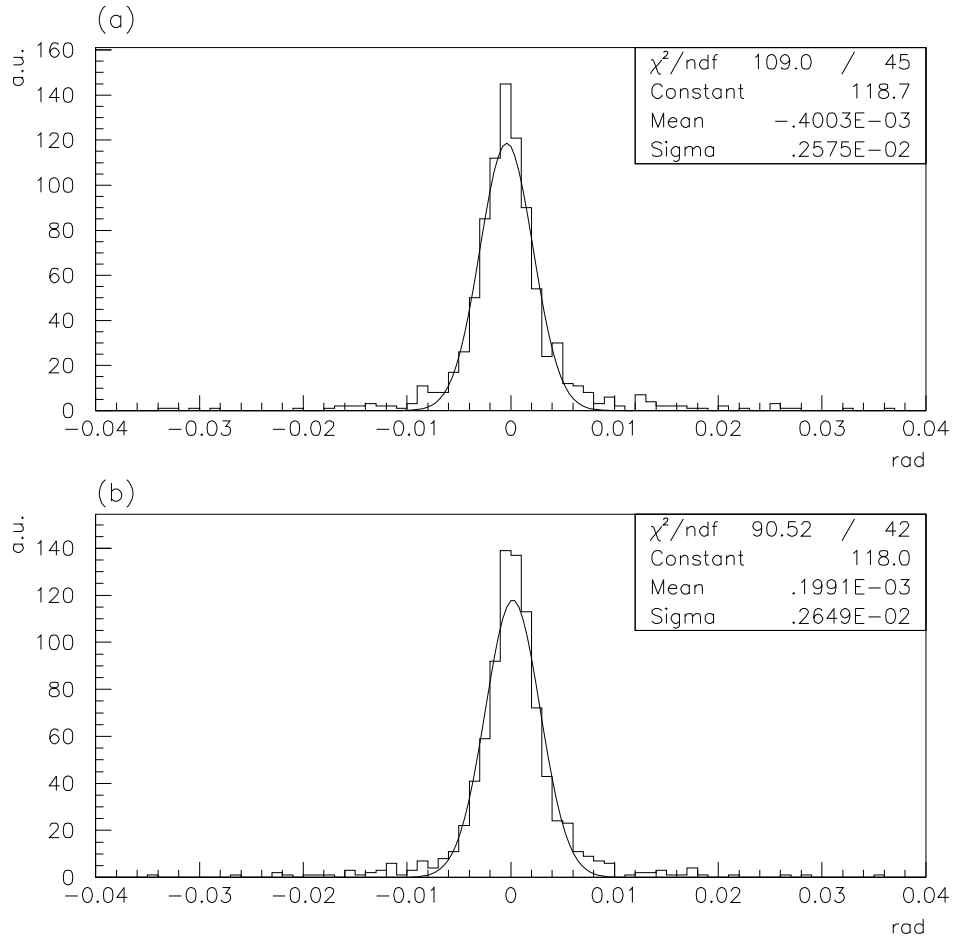
Figure 5.3: Angle difference between reconstructed and real tracks in a) horizontal (y) and b) vertical (z) projections for simulated events. The resolution is ~ 2.6 *mrd*

(a)

χ^2/ndf	77.60 / 52
Constant	95.06
Mean	.9352E-03
Sigma	.3346E-01

(b)

χ^2/ndf	62.54 / 46
Constant	98.15
Mean	-.3746E-02
Sigma	.3307E-01
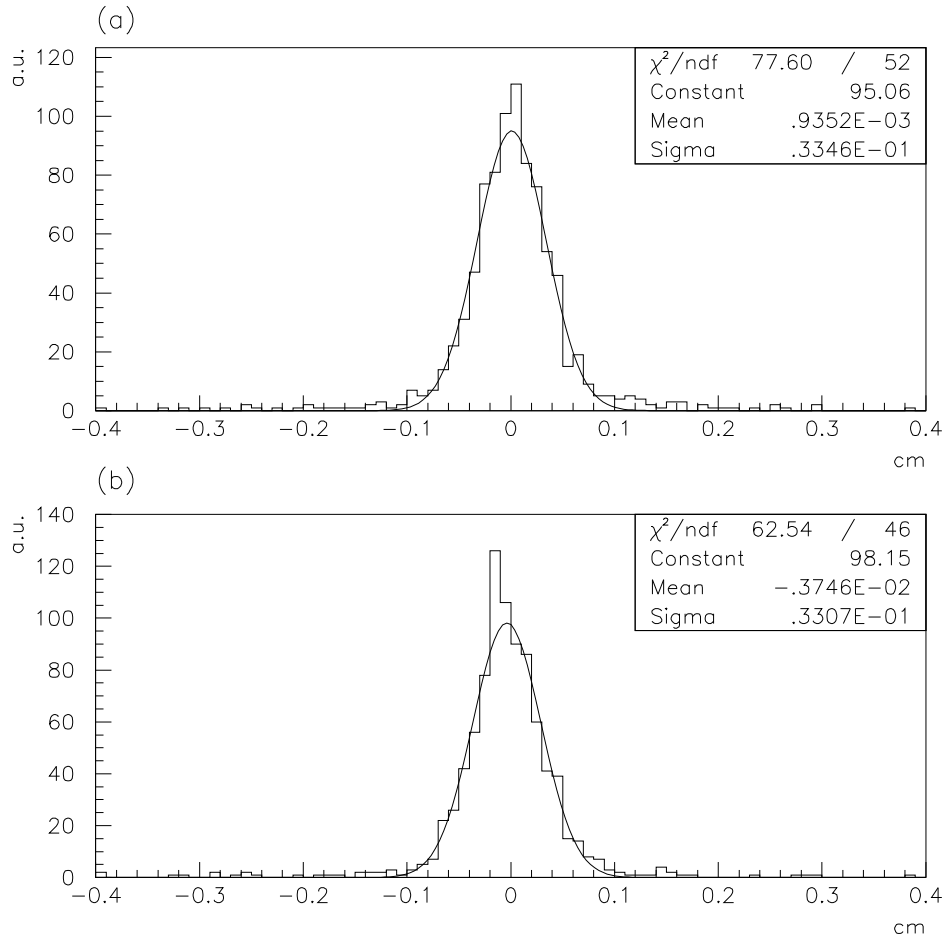
Figure 5.4: Difference between reconstructed and real position of tracks in a) horizontal (y) and b) vertical (z) projections (simulated events). The resolution is $\sim 310~\mu m$

69
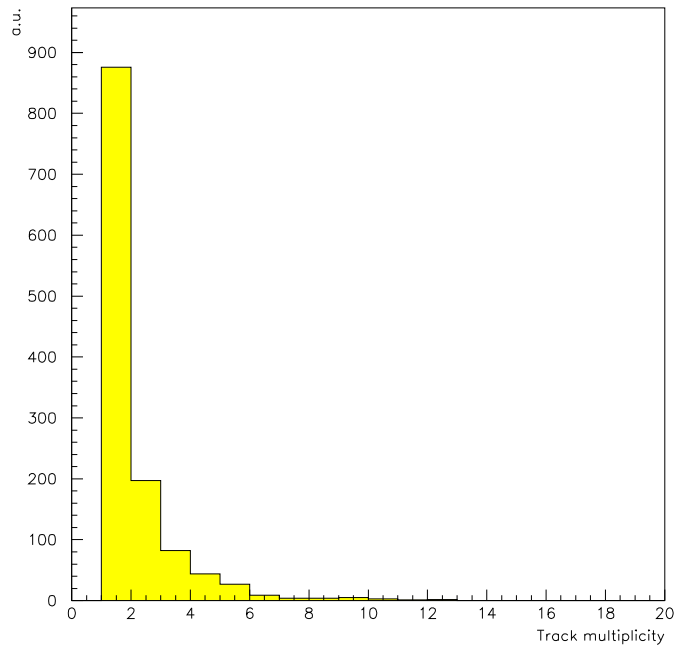
Figure 5.5: Track multiplicity in defined cone. 57 % of the events have a single track in the cone

the simulation. An angle resolution of 6 $mrad$, instead of 2.6 $mrad$, is obtained

for real tracks. This is very reasonable since for simulated events, the limiting

factor is the target tracker resolution which is of the order of 2.5 $mrad$. In the

case of real tracks, the angle measurement resolution in the emulsion which is

$\sim$ 6 $mrad$, is the limiting factor. The increased resolution is not a problem for

the track matching of the $\tau \rightarrow e^- \overline{\nu}_e \nu_\tau$ decay channel owing to the very safe cone

angle cut ($<$ 60 $mrad$). The cone angle cut can be restricted more to minimise

the loss of efficiency due to a high track multiplicity in the cone. However, this

is not optimal due to the showering of the electron tracks in the emulsion and

target trackers.

70
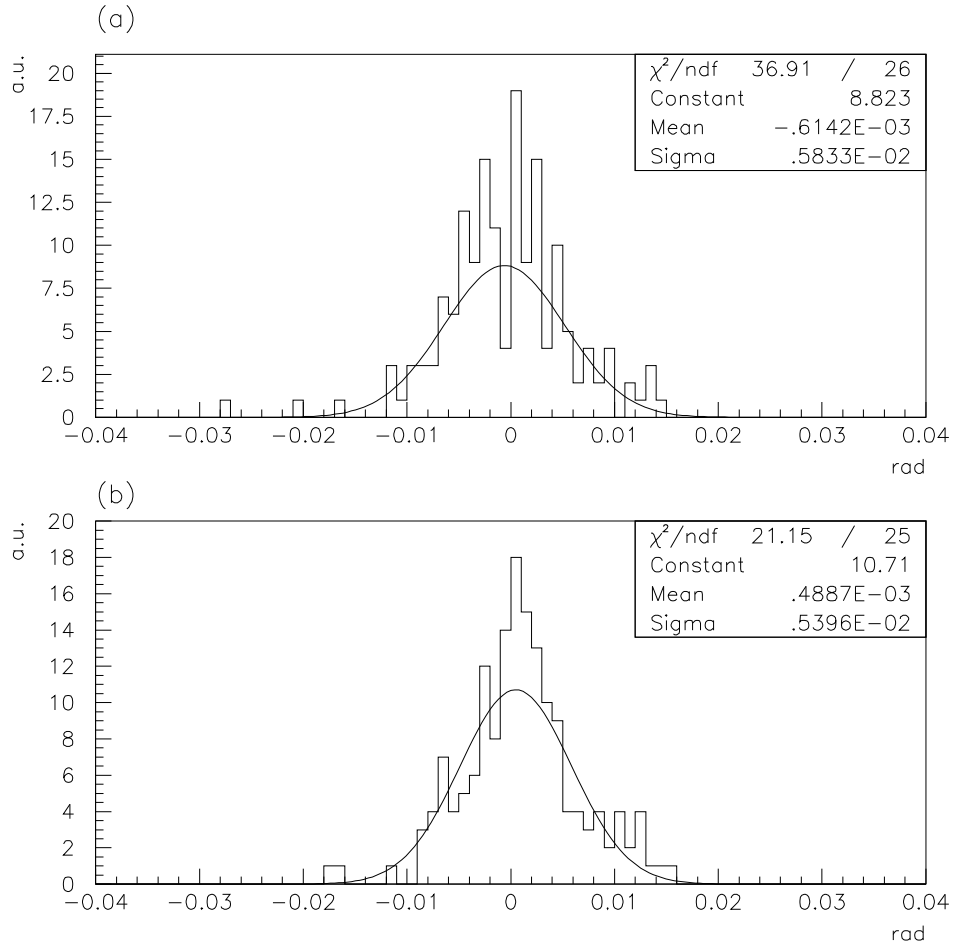
Figure 5.6: Difference between angle reconstructed with the target tracker and measurement in the emulsion for tracks in a) horizontal (y) and b) vertical (z) projections for electron tracks in neutrino interactions

5.7 Charge Measurement

The charge of the hadrons and electrons is measured by the air-core spectrometer formed by the diamond tracker and hexagonal magnet [38]. Properties of the device are summarised in previous chapters.

The diamond tracker system can in principle be used in two ways. The measurement can be optimised for momentum or charge determination. For the momentum measurement, more care has to be taken which induces some inefficiencies to the event tagging and reconstruction. For the $\tau \to e^- \overline{\nu}_e \nu_\tau$ decay search, the energy measurement of the electron can be done more accurately by the calorimeter. This procedure will be explained in detail in the following sections. Charge measurement is more basic information which can be obtained from the air-core spectrometer.

The charge of particles, traversing the diamond trackers, is determined by the sign of the momentum fit. In addition to the target trackers, there is one fibre tracker plane before the magnet and two fibre tracker planes after the magnet. The momentum fit is done by considering the hits upstream and the downstream of the magnet and then by measuring the bending through the magnet. There are three possibilities for the sign of the fitted momentum. The first possibility, when the charge is not determined is a source of inefficiency for the tagging of the $\tau \to e^- \overline{\nu}_e \nu_\tau$ decay. Wrong charge tagging is also a source of inefficiency and it increases the contribution of the background ($\nu_\mu CC$ with the charm production with wrong charge measurement of the e^+ from D^+ decay). Finally, we can
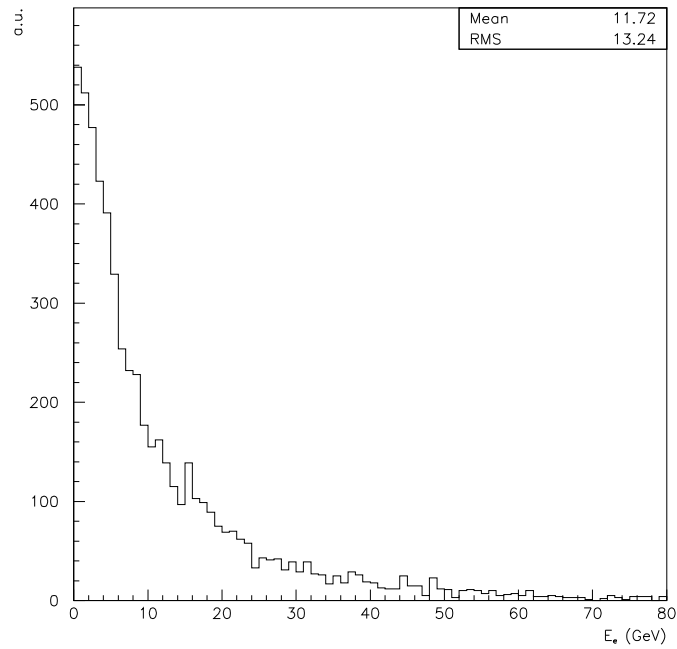
Figure 5.7: Energy distribution of the electrons from the tau decay

distinguish the case of good charge determination.

Main reasons for an undetermined charge in the air-core spectrometer are the following:

- Penetration through more than one magnet triangle (i.e. a "spoke" of the hexagonal magnet is crossed).

- Penetration straight through the spokes of the magnet.

- Non-isolated tracks.

- Inefficiencies in the trackers.

The first two of the reasons are unavoidable given the geometry and the others depend on the intrinsic resolution of the fibre trackers.

73

The wrong charge identification is studied with the help of the detector simulation for electron tracks since no calibration data are available. Single electron tracks, which are coming from the 4th emulsion stack, with different energies are simulated through the hexagonal magnet. Also tau neutrino CC interactions with $\tau \rightarrow e^- \overline{\nu}_e \nu_\tau$ decay, are simulated. The simulated events are processed through the TAUE analysis program and parameters are obtained for comparison of the two. The following conditions are applied to these events before the charge measurement by the diamond tracker is attempted. For the single electron simulation, only the last two conditions are applicable.

- neutrino trigger condition satisfied.

- vertex reconstructed.

- vertex located in 4th emulsion stack.

- $1 \leq E_e \leq 20\ GeV$ (see figure 5.7)

- no other track reconstructed inside the cone around the track (figure 5.2).

The results of the wrong charge tagging calculation, obtained from the electron simulations are shown in figure 5.8. For single electrons, one observes a constant probability (around 3%) at low energy followed by a steady increase at higher energies. The increase starts after $10\ GeV$ which is the upper bound for diamond tracker system design specifications. The bending through the magnet starts to be unreasonable for tracks above $10\ GeV$. The result is worse for the electrons coming from the tau decay due to presence of the other hadronic and electronic
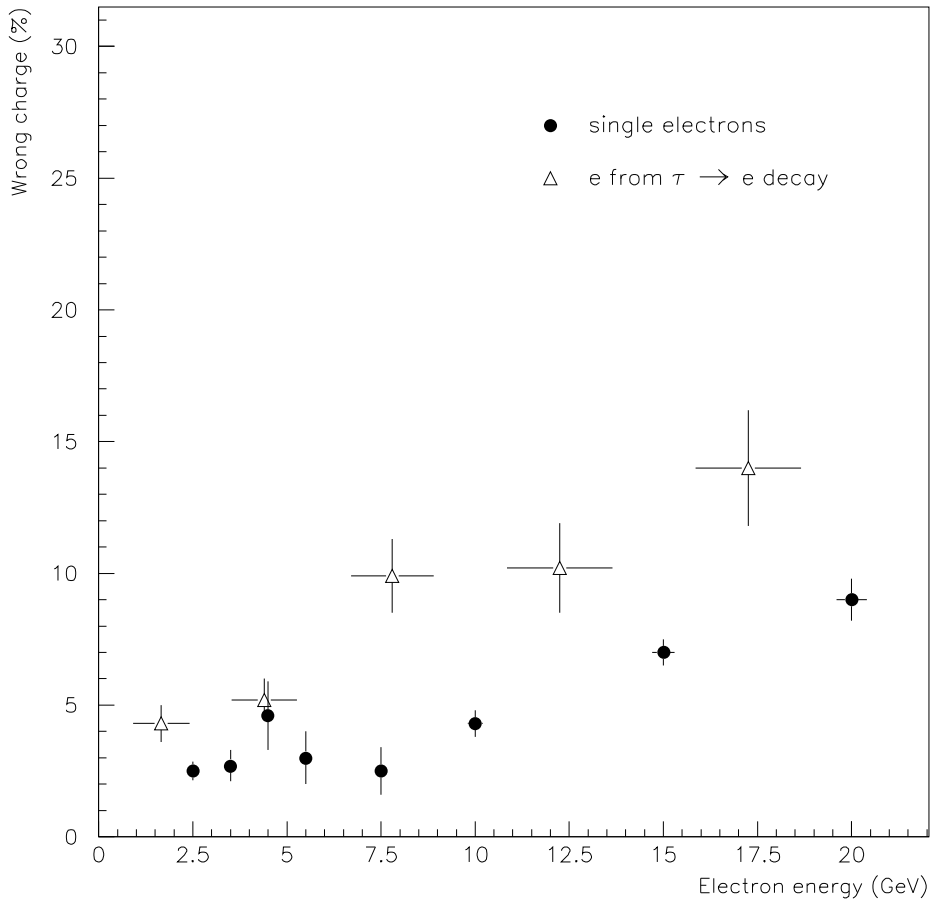
Figure 5.8: Wrong charge tagging percentage for simulated single electrons and for simulated electrons coming from the tau decay

tracks in the event. Moreover, electron tracks are affected more by multiple scattering. These facts increase the possible number of track combination after the magnet at the track fitting stage. Thus the possibility of making wrong track combinations increases.

For the scope of the analysis, overall efficiencies are the important parameter. The results are shown in table 5.2. The wrong charge tagging fraction is of 7.4% for electrons originating from the tau decay. In 52 % of the cases the charge of the electron measured correctly. Wrongly tagged events can be suppressed

by applying a few more cuts on the diamond tracker (DT) momentum fitting parameters. These are the cuts on the number of track combinations on the planes after the hexagonal magnet ($DT_{comb} \leq 10$) and a cut on the number of DT paddles used to for momentum fitting ($DT_{padd} \geq 5$). When both are applied, wrong charge tagging decreases to 1 % level as can be seen from table 5.2, while true charge tagging increases to 68 %. The price to pay to achieve this is a higher inefficiency. 74 % of the tau neutrino CC events are lost when these cuts are applied.

Another, parameter that can be restricted to get better momentum fit in diamond tracker system, is the χ^2 probability of the fit. A cut of $\chi^2 > 0.005$ can be applied for this purpose. However, as can be seen from table 5.2, wrong charge tagging ratio increases ($\sim 10\%$) with the increasing true charge tagging ratio ($\sim 90\%$). In this case also, 71% of the tau neutrino CC interaction events are lost as a price of the gain in true charge tagging efficiency.

Table 5.2: Charge tagging efficiencies for simulated electrons originating from $\tau \to e\overline{\nu}_e\nu_\tau$ decay

cuts	true charge(%)	wrong charge(%)	event loss(%)
	52	7.4	
$DT_{comb} \leq 10$ $DT_{padd} \geq 5$	68	1	74
$\chi^2 > 0.005$	90	10	71

In conclusion, simple rules can be used for charge tagging in this study. Similar calculations for electrons coming from the background neutrino interactions will be presented later.

5.8   Electron Identification

The CHORUS calorimeter consists of three main sections. These are the electromagnetic and two hadronic sections. Electromagnetic and first hadronic part of the detector is made with an advanced technique called spaghetti technique [44].

Response of the calorimeter to electrons and hadrons are calibrated. The CHORUS calorimeter simulation reproduces the results obtained from the experimental data [45]. The calorimeter response to electrons is calibrated as a starting point of the electron identification with the help of the CHORUS simulation program (EFICASS). Single electrons, with different energies (2.5, 3.5, 4.5, 5.5, 7.5, 10.0 and 15.0 GeV), are created just upstream of the calorimeter. The resulting energy resolution is shown in figure 5.9 and the following energy resolution

$$\frac{\sigma(E)}{E} = \frac{(16.4 \pm 1.2)\%}{\sqrt{E}} + (-0.4 \pm 0.4)\% \tag{5.6}$$

is obtained which is in good agreement with the results presented in equation 3.2 (figure 3.7) within the limits of the errors.

The granularity in electromagnetic part of the calorimeter is high which is needed for electron identification. Each electromagnetic module has dimensions of $4 \times 4 \ cm^2$ which can be compared with the Moliere radius of 2 cm. By the definition of Moliere radius, one electromagnetic module of the calorimeter, can contain most of the energy of an electron shower (see figure 5.10). Laterally, the calorimeter has 4 electromagnetic planes and only the very energetic electrons can develop a shower which reaches the first plane of the hadronic calorimeter (~ 21.5 radiation length). Keeping these properties of the calorimeter in mind,
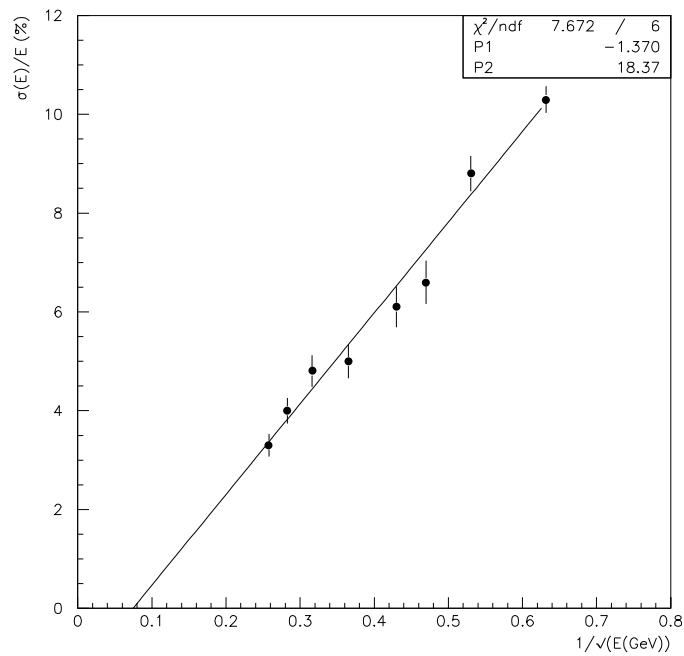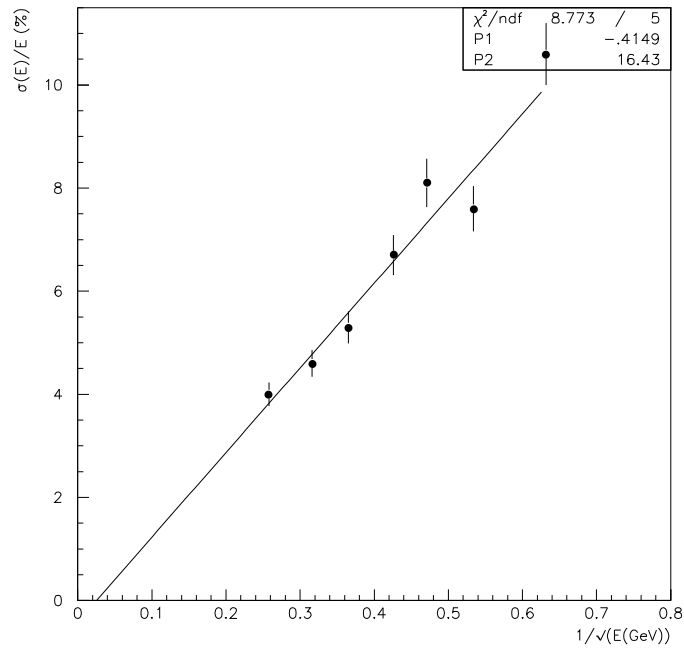
Figure 5.9: Top: Energy resolution of the calorimeter for the single electrons created in front of the calorimeter in the simulation, bottom:energy resolution of the calorimeter for the single electrons simulated in 4th emulsion stack. The electron energy is calculated by the electron identification method
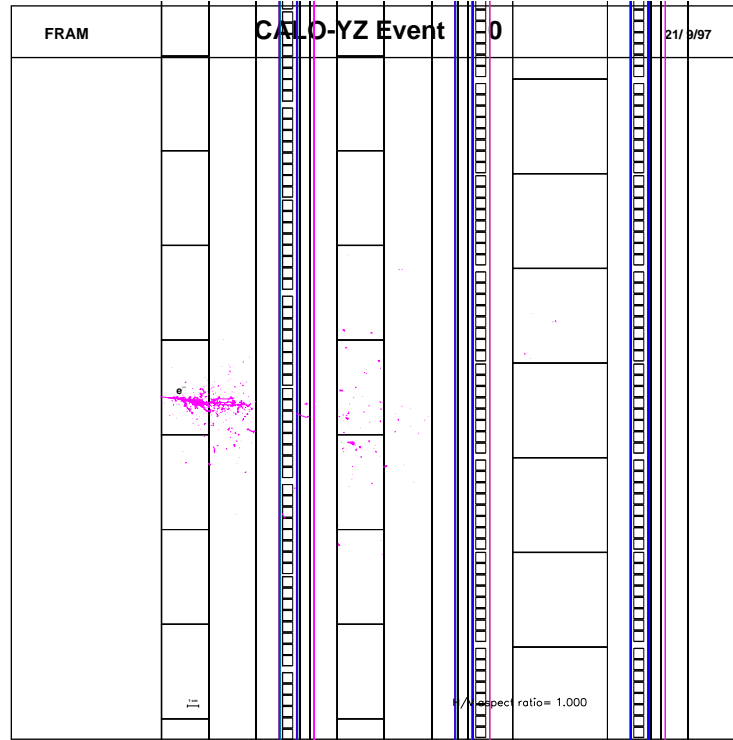
Figure 5.10: An example of a simulated 15 GeV electron shower in the electromagnetic part of the calorimeter. One box in electromagnetic part corresponds to two electromagnetic modules

a method can be developed to the identify electrons, coming from the neutrino interactions.

For this purpose, tracks found in the tracker system, can be extrapolated to the front surface of the electromagnetic calorimeter and corresponding modules on the track path can be grouped (see figure 5.11). The target tracker resolution ($\sim \pm 2.5$ $mrad$) is reasonable enough for this application. When extrapolated, a track originating from the 4th emulsion stack and hitting the centre of an electromagnetic module, should have a ± 8 $mrad$ wrongly calculated angle in one projection to be extrapolated to a wrong electromagnetic module. The energy deposition in the modules on each side of the modules sitting on the track path, are used if the extrapolated track position is close to the edge of a module.
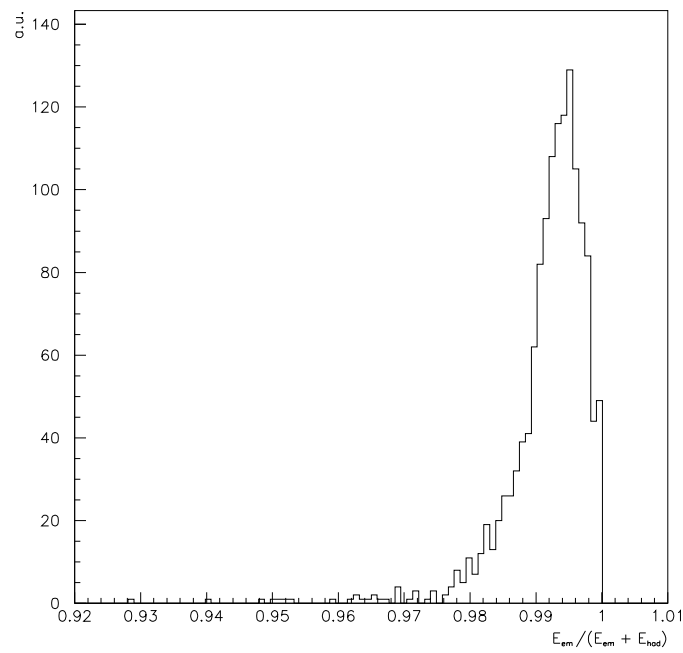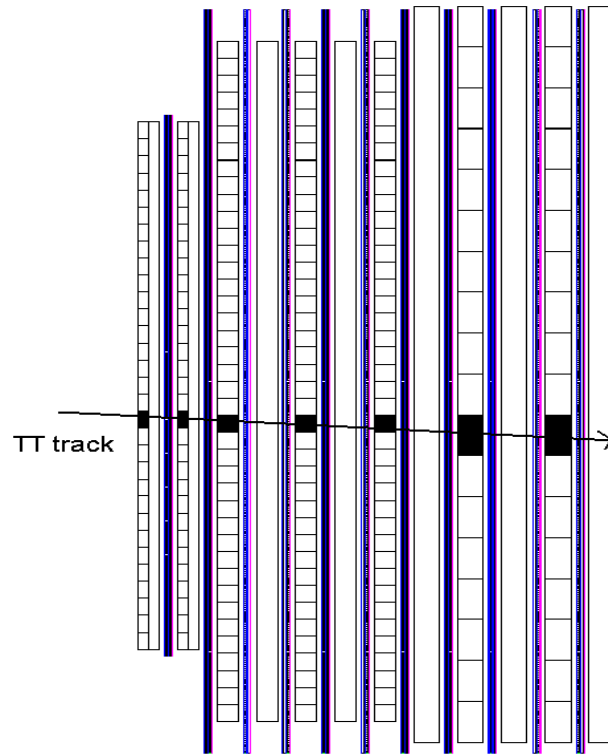
Figure 5.11: Top: Sketch of the method used for electron identification with the CHORUS calorimeter, bottom: Energy ratio of 20 GeV simulated single electrons at calorimeter, obtained by electron identification programme. Peak is closer to 1 for smaller electron energies

With this method the energy deposition on the track is collected for each track in the event and is separated into two parts, electromagnetic and hadronic energy. Comparison of these two parameters can be used to determine the type of the particle creating the track.

The exercise, used to test the energy response of the calorimeter for electrons sent from the front face of the calorimeter is repeated for the single electrons generated in the 4th emulsion stack. In this case, the energy of the electron is calculated using only the electromagnetic modules on the track. The result is shown in figure 5.9. An energy resolution of

$$\frac{\sigma(E)}{E} = \frac{(18.3 \pm 0.8)\%}{\sqrt{E}} + (-1.4 \pm 0.3)\%$$

is obtained for this case. For a sample of single electrons with 20 GeV mean energy, the identification method parameter, which is the ratio of energy deposition in electromagnetic part to the total energy deposition in the main modules, is drawn in figure 5.11. It shows that, the method gives good identification power.

Neutrino interactions, on the other hand, should have less electron identification power because of the particle multiplicity in the events. The presence of other particles complicates the extraction of the energy of the electrons from the calorimeter. At this point, it should be noted that, the probability of having another particle near the track, with angle closer than ± 8 $mrad$ in both projection is very small. Even if one projection of the electromagnetic part, is hit by more than one particle, second projection can still be used.
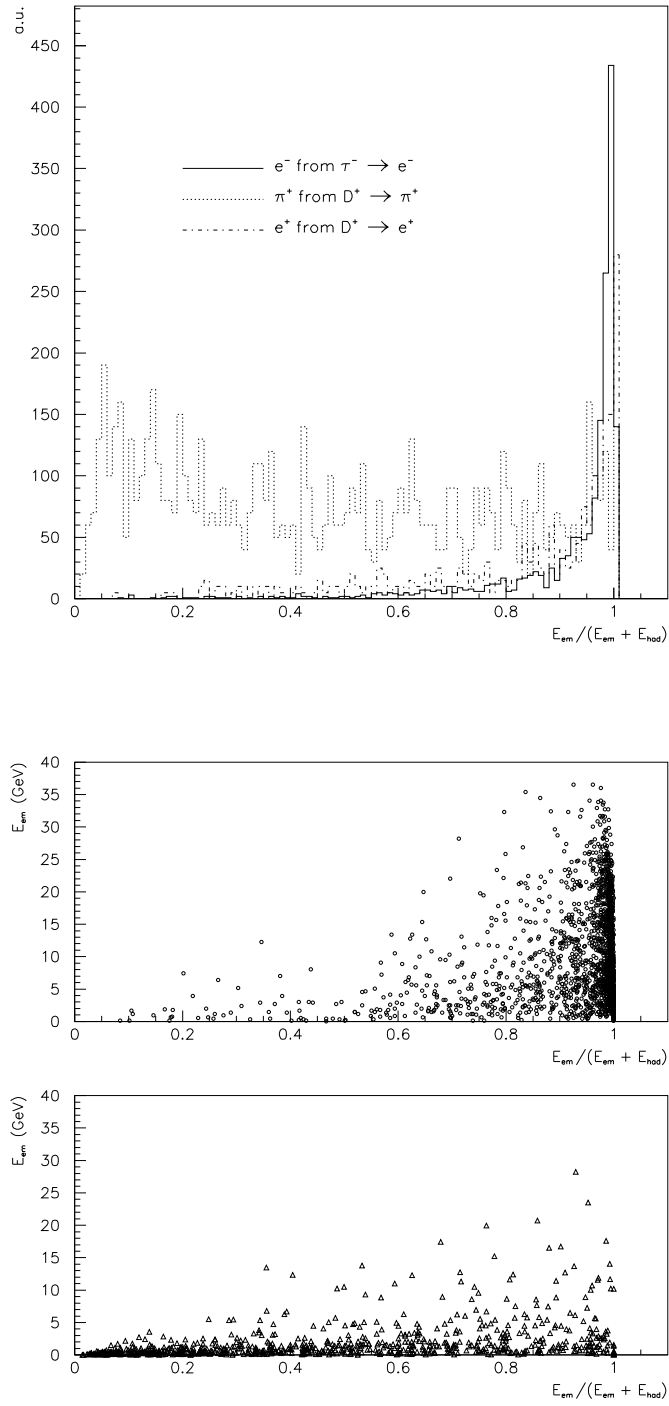
Figure 5.12: Top: Ratio of the electromagnetic energy for electron and pion tracks, middle: electromagnetic energy versus the ratio for electrons, bottom: for pions
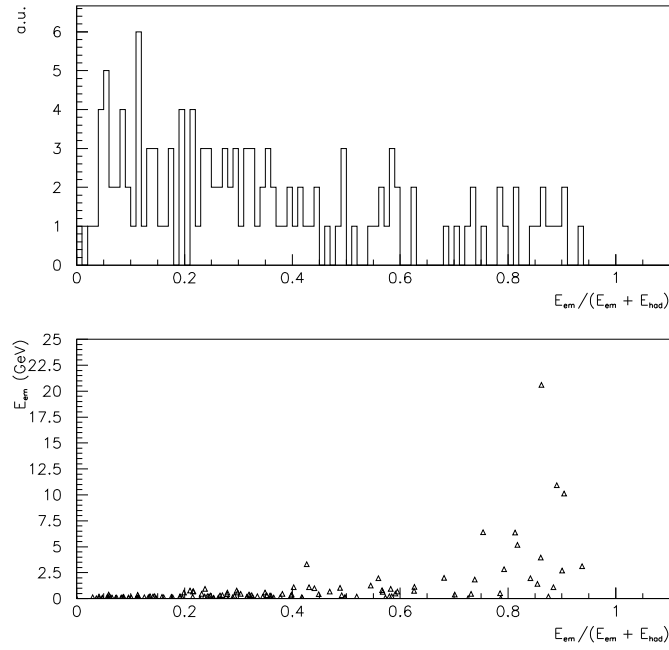
Figure 5.13: Top: Ratio and, bottom: the electromagnetic energy dependence of the ratio for muons

Interactions of hadrons in the electromagnetic calorimeter is a more serious problem for electron identification. The number of pions entering the calorimeter per event is higher than that of electrons. If a pion interacts with the electromagnetic part of the calorimeter, it can be tagged as an electron. This ratio is studied for the pions originating from the charm meson decay. The pions from the primary vertex are not studied since once the vertex is found, the pions are not considered if they are not the kink daughter.

Tau neutrino CC interactions with $\tau^- \rightarrow e^- \overline{\nu}_e \nu_\tau$ decay, ν_μ , $\overline{\nu}_\mu$, ν_e and $\overline{\nu}_e$ CC interactions with the single prong decays of the charm meson, are simulated to calculate the electron identification efficiencies and contributions to the background. As in the case of the charge measurement, cuts that are going to be applied to data are applied to simulated events also. These are:

83
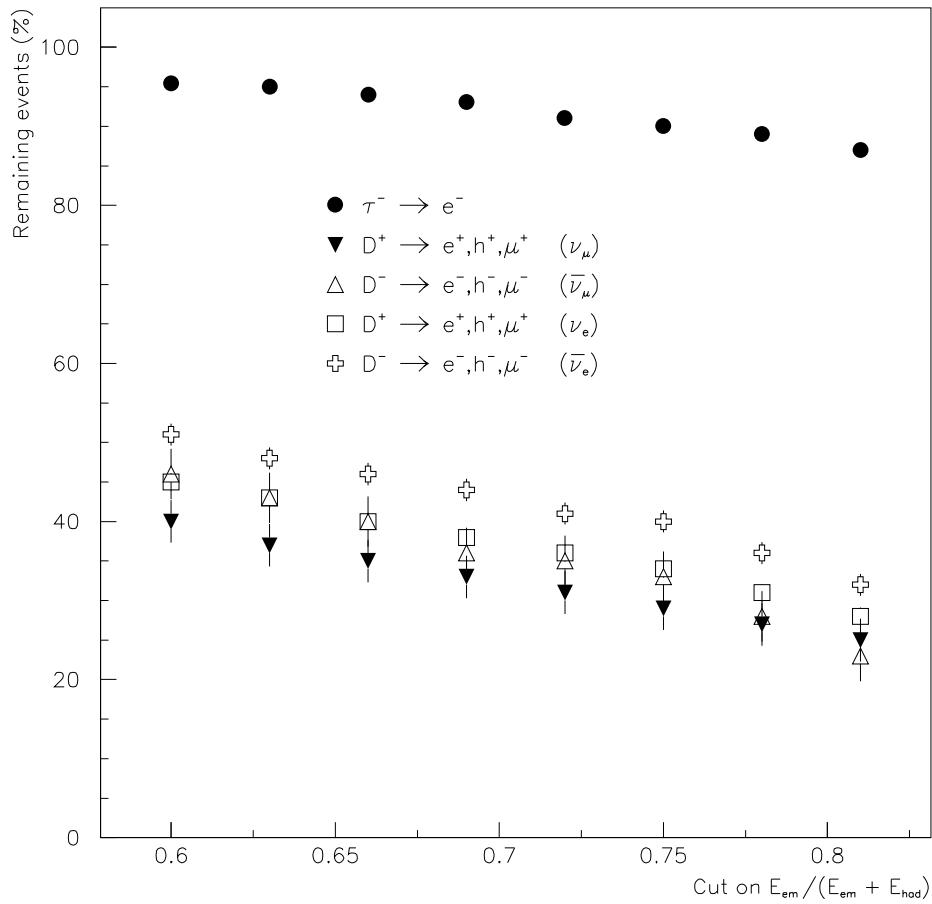
Figure 5.14: Dependence of the cut on the energy ratio for electrons from tau decay and for non-muonic other particles from the charm decay

- Neutrino trigger condition.

- Vertex reconstruction.

- Vertex is in 4th emulsion stack.

- Kinematic event selection criteria are satisfied.

- A single target tracker track is reconstructed inside the cone (figure 5.2).

- One magnet triangle is traversed.

- The track is isolated.

- Kink daughter reaches the calorimeter.

The distribution of the identification parameter for electrons from the tau decay and for pions from the charm meson decay, is shown in figure 5.12. As can be seen from the figure, pions have a rather flat distribution while electrons from the tau and charm decay, have a peak near to one. In the same figure, the electromagnetic energy dependence of the ratio is presented for electrons and pions. Most of the pions are accumulated at the low energy region which gives an additional freedom to decrease the pion contamination in the electron identification. Muons can be identified from the spectrometer. The ones produced by the charm decay which stop in the calorimeter are a small fraction and they can be eliminated (see figure 5.13).

Finally, in order to obtain an optimised cut on the energy ratio, the behaviour of the electrons from tau decay and all the other particles from the charm decay

are studied. The dependence of the cut on the energy ratio is shown in figure 5.14. The electron identification efficiency for electrons from the tau decay, is decreasing slowly since the region shown represents the tail of the distribution for the electrons (see figure 5.12). At the value of $E_{em}/(E_{em} + E_{had}) = 0.6$, $95.5 \pm 0.5\%$ electron identification efficiency is obtained with a $45 \pm 2.7\%$ background contribution on average from the single prong decays of the charmed meson without a cut on the electromagnetic energy. The optimum and a sample cut on energy ratio for electron tagging, can be chosen after overall tau neutrino selection efficiencies and related background contributions are calculated. The conclusion drawn here is that, electron identification with the CHORUS calorimeter can be obtained efficiently enough to detect tau neutrino CC interaction events with $\tau^- \to e^- \overline{\nu}_e \nu_\tau$ decay with their vertex in the 4th emulsion stack.

5.9   Backgrounds Sources

The main reason for backgrounds in this channel, is the similarity of event topology of the charm production events to that of tau production events. The charm particles also have a short decay length similar to the tau lepton. If the primary lepton is not identified by the electronic part of the detector, neutrino interactions with a charm decay are similar visually to the tau neutrino interactions in emulsion. The primary lepton can be miss-identified due to the detector inefficiencies or due to the acceptance. For $\overline{\nu}_{e,\mu}$ CC interactions, this is the main mechanism whereby they can constitute a background to the interaction under consideration.

86

$\nu_{e,\mu}$ CC interactions, on the other hand, are background sources if the primary lepton is missed and the charge of the daughter particle coming from the charm decay is measured incorrectly at the same time. Wrong charge identification has been discussed in previous sections. Erroneous daughter particle identification in the calorimeter introduces other decays of the charm particles as background, in combination with the other conditions mentioned above. Identification of the muons as an electron is less probable than the identification of the hadrons as an electron.

The Charm production in NC interactions, is also source of background, if the charge and/or the type of the particle is miss-identified. This background, when compared with other ones, can be neglected since the charm production cross section is very low (0.8×10^{-4}). Prompt production of ν_τ in the beam (i.e. from D_s decays) is studied in detail [40] and results show that the background events from these neutrinos are negligible $(\nu_{\tau_{prompt}}/\nu_\mu \sim 3 \times 10^{-6})$. For the aim of this study, it can be concluded that $\nu_{e,\mu}$ CC and $\overline{\nu}_{e,\mu}$ CC interactions are the main background sources for the search of ν_τ CC interactions through $\tau \to e^- \nu_\tau \bar{\nu}_e$ decay channel.

Another source of background is formed by pions originating at the ν interaction vertex and reinteracting in the emulsion. They can interact with a typical kink topology. The origin of the process is due to elastic scattering of the π^- with a nucleus, leaving no traces of visible recoil, charged blobs or Auger electrons near the interaction point, or A_1 resonance production in the interaction $\pi^- N \to A_1 N$. A recent measurement of the white kink cross-section gives an

Table 5.3: Background sources for $\tau^- \to e^- \nu_\tau \bar{\nu}_e$ decay search

Background sources
$\nu_\tau N \to X\tau^- \to e^- \bar{\nu}_e \nu_\tau$
$\nu_\mu N \to \mu^- X D^+ \to spr^\dagger$
$\bar{\nu}_\mu N \to \mu^+ X D^- \to spr^\dagger$
$\nu_e N \to e^- X D^+ \to spr^\dagger$
$\bar{\nu}_e N \to e^+ X D^- \to spr^\dagger$
$\nu_\mu N \to \nu_\mu X D^+ D^- \to spr^\dagger \;\; or \;\; D^+ D^0 \to spr^\dagger$
White kink
Main Backgrounds
$\nu_\mu N \to \mu^- X D^+ \to spr^\dagger$
$\bar{\nu}_\mu N \to \mu^+ X D^- \to spr^\dagger$
$\nu_e N \to e^- X D^+ \to spr^\dagger$
$\bar{\nu}_e N \to e^+ X D^- \to spr^\dagger$

$\dagger$ Single prong decays.

effective mean free path of $\lambda_{WK} = (370 \pm 130)m$ at $P_T(kink) > 0.3$ GeV/c [52]. The estimated suppression factor is approximately 4×10^{-6} if no kinematical cuts are applied and if no miss-identification of the hadrons occurs. This is thus a small background source.

Finally, the estimated background for the CHORUS experiment, is less than one. All backgrounds listed here (see table 5.3), do not have serious contribution to the tau neutrino detection (see table 5.7). In the case of a higher statistics sample with a correspondingly increasing background, a method is developed (see appendix A), which can be used to increase the signal to background ratio.

5.10   Contribution to the oscillation sensitivity

5.10.1   Tau neutrino detection efficiency

Most of the items that contributes to the detection efficiency calculations of the tau neutrino CC interaction with tau decaying into an electron have already been explained and discussed above. Efficiencies that are presented for each criterion, are not necessarily decoupled from each other. Some parameters may be correlated with one another and in the final calculations, these correlations have to be taken into account.

For this purpose, the tau neutrino CC interaction with the electronic decay channel of the tau and the main background interactions with the single prong decays of the charm mesons, are simulated. These processes are listed in table 5.4 together with the amount of simulated events. All vertices are placed randomly inside the 4th emulsion stack. For $\overline{\nu}_\mu$ and ν_μ interactions, events with the primary lepton out of the calorimeter acceptance, are not simulated in order to save simulation time. The fraction of these events is taken into account in the efficiency calculations.

The first item on the list is the trigger efficiency. All other efficiencies be handled after the trigger condition applies since an event is not taken by the detector if this condition is not satisfied. The results for different neutrino interactions are presented in table 5.7. All efficiencies in the table are multiplicative. That is, a certain efficiency is obtained after the previous one is applied and hence changing the order may change the apparent efficiency for this item. However, the total

Table 5.4: Number of simulated events for different neutrino interactions

Interaction type	# of events
ν_τ CC*	15000
$\overline{\nu}_\mu$ CC†	90000
ν_μ CC†	60000
$\overline{\nu}_e$ CC†	30000
ν_e CC†	15000

† Only single prong decays of the charmed mesons.
* Only electron decay channel.

efficiency should be almost independent of the order of application of the cuts. The individual efficiencies are presented in another table which is table 5.6.

If the trigger condition is satisfied, vertex has to be constructed with the CHORUS tracker system and it has to be predicted in the 4th emulsion stack. In order to classify these events as non-muonic tau decay, no muon should be identified in the spectrometer and the calorimeter. Moreover, events should satisfy the kinematic conditions (table A.3) applied to select the non-muonic tau decay events. These conditions are applied to reduce the contribution from the background neutrino interactions with the aim to reduce the scanning load. The kinematic conditions and the elimination of events with a muon are combined and presented as one item. As mentioned before, some of the muons from the primary vertex, are eliminated at the simulation stage and inserted into the calculations presented as muons out of the calorimeter acceptance.

The track scanning and vertex location process for non-muonic tau decay events is still in the development phase and hence the scanning methods are

Table 5.5: List of the conditions applied to neutrino interaction events

1-	Trigger condition satisfied
2-	Vertex reconstructed
3-	Vertex is in 4th stack
4-	Event selection criteria (see table A.3)
5-	Muon is out of the calorimeter acceptance
6-	At least one negative track with
	$1 \leq P \leq 20$, $\theta \leq 0.4\ rad$ and $\theta_{X7} \geq 0.05\ rad$
7-	Kink plate number ≥ 4
8-	Scan-back track
9-	Electron identified ($E_{em}/(E_{em} + E_{had}) \geq 0.6$)
10-	Single track in cone
11-	BR($\tau^- \to e^- \nu_\tau \overline{\nu}_e$)
12-	BR($D \to spr^\dagger$)
13-	$\sigma_{\nu_\tau}/\sigma_{\nu_\mu}$
14-	$N(\overline{\nu}_\mu)/N(\nu_\mu)$
15-	$N(\overline{\nu}_e)/N(\nu_\mu)$
16-	$N(\nu_e)/N(\nu_\mu)$
17-	$\sigma(\nu \to l\ c\ X)/\sigma(\nu \to l\ X)$
18-	$N(D)/N(c\bar{c})$

$\dagger$ Single prong decays.

changing in time. At the moment, for these events all target tracker tracks attached to the vertex, having a momentum fit with the diamond trackers in a range $-20 \leq P \leq -1\ GeV/c$, with an angle $\theta \leq 0.4\ rad$ with respect to the neutrino beam and having angle $\theta_{X7} \geq 0.05\ rad$, are chosen as scan-back tracks and all of them are scanned in the emulsion. As explained before, the angle θ_{X7} is calculated with eqn.(5.3). Also, the emulsion plate number where the kink is located, should be greater than 4 (36 emulsion plate exists in one emulsion stack).

The conditions which are enumerated above are necessary for event reconstruction and result in event position prediction in the emulsion before scanning.

Table 5.6: Event detection efficiencies for applied conditions for different processes. Efficiencies are not multiplicative

	ν_τ CC*	$\overline{\nu}_\mu$ CC†	ν_μ CC†	$\overline{\nu}_e$ CC†	ν_e CC†
1-	99.2 ± 0.1	99.2 ± 0.4	98.8 ± 0.3	99.9 ± 0.1	99.9 ± 0.1
2-	96.2 ± 0.3	93.5 ± 1.0	88.9 ± 0.9	96.5 ± 0.3	97.3 ± 0.2
3-	77.5 ± 0.6	66.1 ± 1.9	61.5 ± 1.5	69.5 ± 0.7	68.7 ± 0.6
4-	76.0 ± 0.6	68.6 ± 1.9	63.1 ± 1.4	92.6 ± 0.4	92.1 ± 0.4
5-		2.7 ± 0.1	9.0 ± 0.1		
6-	61.2 ± 0.7	53.7 ± 2.0	33.8 ± 1.4	57.0 ± 0.8	58.2 ± 0.7
7-	44.5 ± 0.7	33.2 ± 1.9	23.2 ± 1.3	43.5 ± 0.8	40.0 ± 0.7
8-	36.7 ± 0.5	36.9 ± 2.0	5.2 ± 0.7	36.3 ± 0.8	5.0 ± 0.3
9-	79.7 ± 0.7	35.1 ± 2.0	32.6 ± 1.4	43.5 ± 0.8	39.1 ± 0.7
10-	56.5 ± 0.6	59.6 ± 2.0	62.5 ± 1.4	55.4 ± 0.8	54.2 ± 0.7

† Only single prong decays of the charmed mesons.
* Only electron decay channel.

As a next step, the selected scan-back tracks are searched for in CS and SS, and the vertex location procedure starts if the track is found in these emulsion sheets. Scanning and vertex location efficiencies are expected to be similar for the electron decay events of the tau compared to other non-muonic decays since no particle type information is used for selection of the scan-back tracks. Other hadronic tracks from the primary vertex are useful to locate the neutrino interaction vertex in the emulsion. They can be used also if the electron from the tau decay is lost or has showered in the emulsion or in the tracker region.

Detailed kink search efficiency calculations have been done already for other non-muonic and muonic decay channel events of the tau lepton. The results obtained for other non-muonic decay channel processes are assumed to be applicable to the events with a decay into an electron. This is a reasonable assumption for the goal of this study. The kink finding efficiency calculation is quite complex

Table 5.7: Event detection efficiencies for applied conditions to different processes. Efficiencies are multiplicative

	ν_τ CC*	$\overline{\nu}_\mu$ CC†	ν_μ CC†	$\overline{\nu}_e$ CC†	ν_e CC†
1-	99.2 ± 0.1	99.2 ± 0.4	98.8 ± 0.3	99.9 ± 0.1	99.9 ± 0.1
2-	96.4 ± 0.3	93.7 ± 1.0	89.2 ± 0.9	96.5 ± 0.3	97.3 ± 0.2
3-	80.9 ± 0.5	70.8 ± 1.9	69.4 ± 1.5	72.0 ± 0.7	70.6 ± 0.6
4-	82.3 ± 0.6	78.6 ± 2.1	75.4 ± 1.6	95.9 ± 0.4	93.9 ± 0.4
5-	-	2.7 ± 0.1	9.0 ± 0.1	-	-
6-	74.2 ± 0.7	74.4 ± 2.5	55.0 ± 2.2	73.6 ± 0.9	69.5 ± 0.8
7-	94.4 ± 0.4	86.5 ± 2.3	91.5 ± 1.7	88.8 ± 0.7	89.2 ± 0.6
ε_R	44.5 ± 0.7	0.9 ± 0.05	2.1 ± 0.1	43.5 ± 0.8	40.0 ± 0.7
ε_S	13.0 ± 0.6	13.0 ± 0.6	13.0 ± 0.6	13.0 ± 0.6	13.0 ± 0.6
ε_{kink}	26.0	26.0	26.0	26.0	26.0
8-	63.8 ± 1.8	78.8 ± 4.6	12.3 ± 3.1	76.8 ± 1.5	9.1 ± 0.9
9-	90.9 ± 1.4	50.8 ± 6.3	35.7 ± 4.6	53.7 ± 2.0	54.0 ± 5.0
10-	73.4 ± 2.2	90.6 ± 5.2	40.0 ± 8.8	76.4 ± 2.4	40.7 ± 6.7
ε_{e^-}	42.5 ± 1.9	36.2 ± 5.3	1.8 ± 0.4	31.5 ± 1.7	2.0 ± 0.4
11-	18.0	-	-	-	-
12-	-	65.0	65.0	65.0	65.0
13-	53.0	-	-	-	-
14-	-	5.6	-	-	-
15-	-	-	-	0.17	-
16-	-	-	-	-	0.7
17-	-	3.0	3.0	3.0	3.0
18-	-	33.0	33.0	33.0	33.0
$\varepsilon_{total}^{††}$	$6.1 \pm 0.4 \times 10^{-4}$	$4.0 \pm 0.7 \times 10^{-8}$	$7.9 \pm 2.0 \times 10^{-8}$	$5.0 \pm 0.4 \times 10^{-8}$	$1.2 \pm 0.3 \times 10^{-8}$

† Only single prong decays of the charmed mesons.
* Only electron decay channel.
†† $\varepsilon_{total} = \varepsilon_R \ \varepsilon_S \ \varepsilon_{kink} \ \varepsilon_{11-18}$

and has been explained shortly in previous sections.

The next step is to trace back the kink daughter such that one can extract information from the electronic part of the detector. The target tracker track can be extrapolated to the subsequent detector parts. For the kink daughter electrons, it is necessary to eliminate showering tracks in the emulsion or the fibre trackers. This is the reason for the condition of having only one fibre tracker track in a 60 *mrad* cone around the kink daughter track extrapolated from the emulsion. It is also important that the kink daughter should be within the geometrical acceptance of the calorimeter. Moreover, the electron track should be one of the scan-back tracks. This condition automatically includes the conditions applied for scan-back track selection. The kink daughter track extrapolation to the calorimeter gives the possibility of identifying an electron-like shower in the electromagnetic calorimeter and hence the possibility to identify the particle type of the kink daughter.

The total efficiencies for tau to electron decay events and background neutrino interactions are listed in table 5.7. The applied conditions are represented by numbers in the table and the meaning of these numbers are listed in table 5.5 because of practical problems. Table 5.7 also contains parameters such as cross sections, beam abundances, branching ratios, etc. in order to be able to calculate the total detection efficiency of the corresponding neutrino interaction.

94

5.10.2 Contribution to the CHORUS sensitivity to oscillation

At the moment, % 10 of the CHORUS neutrino interaction data has been analysed and no ν_τ candidate interaction has been observed yet. 15000 ν_μ CC and 1343 ν_μ NC events have been located in emulsion. The pilot analysis, has been performed for muonic and hadronic decay channels of the tau lepton. A similar method is followed here to determine the expected improvement on the present CHORUS $\sin^2 2\theta_{\mu\tau}$ limit with the inclusion of tau to electron decay channel.

The oscillation probability, equation 2.16, for the case of two neutrino type mixing, is reduced to the following form for large Δm^2 values.

$$P(\nu_\mu \rightarrow \nu_\tau) \leq \frac{1}{2}\sin^2 2\theta_{\mu\tau} \tag{5.7}$$

The oscillation probability $P(\nu_\mu \rightarrow \nu_\tau)$ is a measurable quantity and when no ν_τ candidate interaction is observed, it can be determined with the following formula [53]:

$$P(\nu_\mu \rightarrow \nu_\tau) \leq \frac{2.3}{N(\nu_\mu)}\frac{\sigma(\nu_\mu)}{\sigma(\nu_\tau)}\frac{1}{\frac{A_{\tau\mu}}{A(\nu_\mu)}\sum_{i=\mu,h,e}\frac{A_i}{A_{\tau\mu}}\,\varepsilon_i\,r_i\,Br_i} \tag{5.8}$$

where $N(\nu_\mu)$ is the number of scanned events with their vertex located in the emulsion, $\sigma(\nu_\mu)$ $(\sigma(\nu_\tau))$ is the beam weighted ν_μ CC (ν_τ) event cross section, A is the overall acceptance and efficiency of the corresponding process, ε is the kink finding and event identification efficiency, r is fraction of events existing in this class with respect to the μ decay channel of the tau and Br is the branching ratio of the corresponding decay channel.

The scanning efficiency in the 4th emulsion stack is determined for the hadronic decay channel to be 15.5±0.6% and 32.1±0.2% for the muonic decay channel [54]. For the electron channel, a value equal to the hadronic decay channel is assumed with the inclusion of a difference of the scanning efficiency in CS and SS ($\sim 84\%$). The reconstruction efficiency for the electron decay channel is determined via the simulation results and it is $44.5 \pm 0.7\%$ as listed in table 5.7. That parameter is obtained independently for muonic decay channel as $46.0 \pm 0.9\%$. When all these parameters are combined, a value of $39.2 \pm 1.7\%$ is obtained for the parameter $A_e/A_{\mu\tau}$ for the electron decay channel for events in the 4th emulsion stack.

The fraction of events in the electron decay channel is lower than the hadronic decay channel since only the events with their vertex in the 4th emulsion stack is used. When this fact is taken into account, approximately 11% of the events enter into this category. The kink finding efficiency is assumed to be equal to the one of the hadronic decay channel as mentioned before. In the electron decay case, the event identification efficiency is considered and inserted into the kink finding efficiency which is estimated by simulation to be $11.0 \pm 0.6\%$.

All the values, used to calculate the $\sin^2 2\theta_{\mu\tau}$ limit at large Δm^2 for the electron decay channel and other decay channels of the tau are listed in table 5.8. In order to calculate the fractional contribution of the electron decay channel of the tau to $\sin^2 2\theta_{\mu\tau}$, the probability ratio for the two cases has to be derived.

$$\frac{P_{\mu,h,e}(\nu_\mu \to \nu_\tau)}{P_{\mu,h}(\nu_\mu \to \nu_\tau)} = \frac{\sum_{i=\mu,h} \frac{A_i}{A_{\tau\mu}} \varepsilon_i \, r_i \, Br_i}{\sum_{i=\mu,h,e} \frac{A_i}{A_{\tau\mu}} \varepsilon_i \, r_i \, Br_i} \tag{5.9}$$

Probability ratio in eqn.(5.9) is calculated as 0.96 by using the values listed

Table 5.8: List of parameter values used in $\sin^2 2\theta_{\mu\tau}$ limit calculation

Decay mode	$\frac{A_i}{A_{\tau\mu}}$	Br_i	ε_i	r_i
$\tau \to \mu^- \nu_\tau \overline{\nu}_\mu$	1.07	0.18	0.55	1
$\tau \to h^-(nh^0)\nu_\tau$	0.36	0.50	0.26	0.44
$\tau \to e^- \nu_\tau \overline{\nu}_e$	0.39	0.18	0.11	0.11

in table 5.8. This is an improvement of 4% in the $\sin^2 2\theta_{\mu\tau}$ sensitivity at large Δm^2. It should be noted here that the scan-back track and particle identification conditions were not applied in the hadronic decay mode. When these conditions are also neglected for the electron channel to reach similar conditions, an improvement of 6% is obtained. The present CHORUS limit on $\sin^2 2\theta_{\mu\tau}$, for large Δm^2 is,

$$\sin^2 2\theta_{\mu\tau} \leq 4.5 \times 10^{-3} \tag{5.10}$$

When results of the $\tau \to e^- \overline{\nu}_e \nu_\tau$ decay channel are included, the present limit decreases to the value,

$$\sin^2 2\theta_{\mu\tau} \leq 4.23 \times 10^{-3} \tag{5.11}$$

This improvement is reached without any special event selection process and without any extra scanning load. With some additional selection mechanisms, more tau to electron events can be added, in non-muonic decay sample. This can improve the CHORUS sensitivity. For these calculations, presently available values are taken and a pessimistic approach is used in the calculations. Full scanning results are necessary for more complete calculations.

CHAPTER 6

CONCLUSION

The CHORUS experiment is designed to detect $\nu_\mu \to \nu_\tau$ oscillation via the observation of the tau in three decay modes. An additional channel, $\tau \to e^- \nu_\tau \overline{\nu}_e$, was not included since electrons, while traversing the emulsion stacks, produce a lot of secondary particles via the Bremstrahlung process. Each emulsion stack is one radiation length thick and it is highly probable that the electron is lost if it traverses the target. These difficulties make them undetectable by the CHORUS detector system since they cannot reach the calorimeter.

Electrons, produced in the 4th emulsion stack, on the other hand, have some chance to reach the calorimeter without being lost. Assuming that the neutrino interaction vertices are distributed uniformly inside the stack, the probability of getting electrons out of the emulsion without showering can be estimated to be 63%. This problem is eliminated by requiring the condition of single target tracker track in the cone. $\sim 57\%$ of the events have a single track in the 60 $mrad$ angular region defined around the kink daughter track (see figure 5.2).

The most useful improvement in this study, has been done on electron identification. Since the detector was not designed to identify electrons, some techniques such as a preshower detector for electron pion separation, were not considered in

the design stage. On the other hand, the calorimeter of the experiment has very good granularity in the electromagnetic part and a very good energy resolution. This is a very suitable condition for electron identification. However, the presence of other particles in the neutrino interactions complicate electron identification with the calorimeter. Because of the high typical neutrino energy of the CERN WB beam, all these particles are contained in a rather narrow cone, due to Lorentz boost. These facts affect more the tau to electron event selection, since especially electrons produced by gamma conversion decrease the selection efficiency. As explained in previous sections, this problem is eliminated automatically, since tau to electron decay events have to be in the non-muonic tau decay sample. Once the event is found and the kink daughter vertex is identified, all electrons from gamma conversion are not background anymore since their conversion point can be identified in emulsion.

After eliminating the above problems, kink daughter tracks can be extrapolated to the calorimeter. A possible calorimeter hit clustering around this track should give an indication about its nature by comparing the amount of energy deposited in the electromagnetic and hadronic parts. The clustering can be done by using only single calorimeter modules since the Moliere radius is 2 cm and an electromagnetic module has dimensions of 4×4 cm. Target tracker tracks are also precise enough (~ 3 $mrad$) to achieve this track extrapolation. When all these pieces of information are combined in a hit clustering algorithm, 95% electron identification is reached for events where the vertex is reconstructed and non-muonic event selection criteria are imposed and a charge determination is

required.

Scanning and kink finding efficiencies in emulsion plates and in changeable sheets (CS and SS), are estimated by repeating a similar exercise for the hadronic decay channel of the tau. Moreover, results of track scanning for the 1994 neutrino data are used in this estimation. Electron tracks are chosen from this data if the event vertex is in 4th emulsion stack. These tracks are examined for scanning efficiencies in CS and SS, and similar results to the ones for the hadronic sample, are obtained (see table 5.1).

Charge assignment for the electron tracks, are investigated using simulated tau neutrino CC events with the electronic decay mode of the tau. The charge measurement quality is expected to be equal for electrons and for the same momentum. Here, showering electrons are assumed to be eliminated already from the sample as mentioned above. Multiple scattering, on the other hand, is larger for electrons. However, when radiation length of the fiber trackers around the hexagonal magnet and that of hexagonal magnet itself, are considered, it can be neglected. For the tau decay events, in 52% of the cases the charge of the electron is measured correctly. Wrong charge measurement percentage is 7.4% for the same events. In the rest of the cases, no momentum is assigned.

Taking all efficiencies into account, the total background contribution to tau neutrino detection via the electron channel, is of the order of 10^{-7} and hence negligible (see table 5.7). This is the main advantage of the experiment. The total background contribution is negligible for the total number of collected ν_μ CC interactions (~ 350000). Thus also for the electronic decay channel, no

background need to be expected.

Presently, the CHORUS experiment groups have analysed 10% of the data. No ν_τ candidate has been observed yet. The analysed data sample contains the muonic and hadronic decay samples. A limit of $\sin^2 2\theta_{\mu\tau} \leq 4.5 \times 10^{-3}$ is obtained at large Δm^2 with present analysed sample. A similar exercise is repeated within the inclusion of the electron decay sample. It is seen that, $4 - 6\%$ improvement at $\sin^2 2\theta_{\mu\tau}$ limit is reachable with the neutrino events which have interaction vertex in 4th emulsion stack. The above value decreases to $\sin^2 2\theta_{\mu\tau} \leq 4.23 \times 10^{-3}$ with the inclusion of this channel. It should be stressed again that, no extra emulsion scanning load nor extra data taking need to be done to reach this result. With better event selection criteria, the number of events observable with the electron decay channel in the non-muonic decay sample can be enhanced and the contribution of this channel can be increased. Moreover, improvements on track scanning, vertex location and kink search in emulsion for the hadronic decay channel, can automatically be applied to this channel. The sensitivity of the electron decay channel on $\sin^2 2\theta_{\mu\tau}$ can be 9% of that of the hadronic channel ($\frac{1}{4} \times \frac{0.18}{0.5}$) if all efficiencies are equal.

There is an important byproduct of this study. If electrons can be identified in emulsion, which seems possible (although more investigation is necessary) tau neutrino detection with electron decay channel can be done in the other emulsion stacks (1st, 2nd and 3rd) too. Neutrino interaction vertices can still be found in the emulsion by following hadrons to the primary vertex. However, showering electrons do not allow the use diamond trackers for charge measurement. In this

case, positrons are automatically in the sample. This means that positron decays of a charmed meson which are produced by beam neutrino (ν_μ) CC interactions, will constitute a background and they have to be eliminated. As presented in appendix A, these background interactions can be suppressed by a factor 7 with only 20% loss for the tau neutrino events. By optimising the applied cuts, more background suppression is possible. This method is more advantageous than the charge measurement by the diamond tracker since during the later process, 48% of the events are lost. Therefore, not requiring the charge measurement by the diamond tracker system, even better event detection efficiency can be achieved. With this method $20 - 30\%$ improvement on $\sin^2 2\theta_{\mu\tau}$ limit can be reached. In addition, with electron identification in emulsion, the electron neutrino CC interaction can be studied.

Finally, all these results show that tau neutrino detection in the 4th emulsion stack with electronic decay mode of the tau is possible and brings appreciable improvement to the CHORUS sensitivity with no additional cost. With this statement, it can be said that the goal of this study is fulfilled. Further improved analysis methods can still improve the results. The full CHORUS neutrino data analysis is necessary for final numbers and conclusions.

REFERENCES

[1] E. Fermi Z. Physik 88-161 (1934)

[2] B. Pontecoervo, Chalk River Laboratory Report No. PD-205 (1946)

[3] T.D.Lee, C.N. Yang Phys. Rev. 104, 254 (1956)

[4] C.S. Nu et al., Phys. Rev. 105, 1413 (1957)

[5] R.L. Garwin, L.M. Lederman, H.Weinsich Phys. Rev. 105, 1415 (1957)

[6] J.I. Friedman, V.L. Telegdi Phys. Rev. 105, 1681 (1957)

[7] M. Goldhaber, L. Grodzius, A.W. Sungar Phys. Rev. 109, 1015 (1958)

[8] F. Reines, C.L. Cowan, Phys. Rev. 113, 273 (1969)

[9] G. Feinberg Phys. Rev. 110, 1482 (1958)

[10] T.D. Lee, C.N. Yang Phys. Rev. Lett. 4, 307 (1960)

[11] G. Danby, J.-M. Gaillard, K. Goulianos, L. Lederman, N.Mistry, M. Schwartz and J. Steinberger, Phys. Rev. Lett. 9, 36 (1962)

[12] S.L. Glashow Nucl. Phys. 22, 579 (1961)

[13] S. Weinberg Phys. Rev. Lett. 19, 1264 (1967)

[14] A. Salam, Ward Phys. Lett. 13, 168 (1964)

[15] F.J. Hasert et al., Phys. Lett. 46B, 121, 138 (1973)

[16] M. Perl et al., Phys. Rev. Lett. 35, 1489 (1975)

[17] S. Aktağ, A. Çelikel, A.K. Çiftçi, S. Sultansoy and O.Ü. Yılmaz AU-HEP-96-01

[18] J.N. Bahcall and M.H. Pinsonneault, Rev. Mod. Phys. 64, 885 (1992)

[19] S. Turck-Chiéze and I. Lopes, Astrophys. J. 408, 347 (1993)

[20] B.T. Cleveland et al., Nucl. Phys. (Proc. Supp.) B38, 47 (1995)

[21] P. Anselmann et al., Phys. Lett. B327, 377 (1994)

[22] J.N. Abdurashitov et al., Nucl. Phys. (Proc. Supp.) B38, 60 (1995)

[23] Y. Suzuki, Nucl. Phys. (Proc. Supp.) B38, 54 (1995)

[24] FREJUS collaboration Phys. Rev. D51, 2090 (1995)

[25] Kamiokande Collaboration Phys. Lett. B335, 237 (1994)

[26] IMB Collaboration Phys. Rev. Lett. 69, 1010 (1992)

[27] B. Pontecorvo, Zh. Eksp. Teor. Fiz. 34, 247 (1957)

[28] Z. Maki, M. Nakagawa and S. sakata, Prog. Theor. Phys. 28, 870 (1962)

[29] V. Zacek et al., Phys. Lett. B164, 193 (1985)

[30] C. Athanassopoulos, et al., LSND Collaboration Phys. Rev. Lett. 75, 2650 (1995)

[31] C. Athanassopoulos, et al., LSND Collaboration UCRHEP-E197

[32] Armenise, A. et al., "A new search for ν_μ - ν_τ oscillations" CERN-SPSLC/90-42 P254 (1990)

[33] N. Ushida et al., Phys. Rev. Lett. 57, 2897 (1986)

[34] P. W. Higgs, Phys. Lett. 12, 132 (1964)

[35] S. M. Bilenky and S. T. Petcov, Rev. of Mod. Phys. 59, 3-1 671 (1987)

[36] V. Gribov and B. Pontecorvo, Phys. Lett. B28, 463 (1969)

[37] B. Kayser, Phys. Rev. D24, 110 (1981)

[38] Eskut, E. et al. "The CHORUS Experiment to search for $\nu_\mu \rightarrow \nu_\tau$ oscillation" to be publ. in: Nucl. Instr. Meth. Phys. Res. (74p) 1997

[39] D. Geiregat et al., CHARM II Collaboration, Phys. Lett. B232, 539 (1989)

[40] B. van de Vijver, "Prompt Tau-neutrino Background in Wide-band Muon-neutrino Beams" subm. to NIM (1996)

[41] P. Annis et al., "The CHORUS scintillating fiber tracker and opto-electronic readout system" CERN-PPE/97-100 (1997)

[42] M. Gruwe, PhD Thesis, Université Libre de Bruxelles (1994)

[43] F. Bergsma et al., "The hexagonal toroidal air-core magnet of the CHORUS detector" Nucl. Instr. and Meth. Phys. Research A357, 243-248 (1995)

[44] D. Acosta et al., Nucl. Instr. and Meth. A 308, 481 (1991)

[45] E. Di Capua et al., "Response to electrons and pions of the calorimeter for the CHORUS experiment" Nucl. Instr. and Meth. A 378, 221 (1996)

[46] H. Abramovitz et al., CDHS Collaboration, Nucl. Instr. and Meth. 180, 429 (1981)

[47] J.P. Dewulf et al., CHARM II Collaboration, Nucl. Instr. and Meth. A 252, 443 (1986)

[48] S. Aoki, et al., Nucl. Instr. and Meth. B 51, 446 (1990)

[49] van Beuzekom, M.G. et al., "The trigger system of the CHORUS experiment", to be submitted to Nucl. Instr. and Meth. (1997)

[50] Astier, P. et al., "Search for the oscillation $\nu_\mu \to \nu_\tau$ " CERN-SPSLC/91-21 P261 (1991)

[51] P. Migliozzi, PhD thesis, Pascuale, University of Napoli "Federico II" (1997)

[52] K.Kodama et al., COSMOS Proposal, Fermilab PROPOSAL P803 (1993) ; Udate Report on Fermilab E803, (1995)

[53] C. Weinheimer ICHEP conference proceedings, Warsaw, (1996)

[54] O. Sato, Internal reports of the CHORUS Collaboration (1997)

[55] R.M.Barnett et al., PDG group Phys. Rev. D54, 179 (1996)

APPENDIX A

KINEMATICAL BACKGROUND SUPPRESSION

Kinematical quantities describing the neutrino-nucleon interaction [55] can be used for the purpose of background suppression. The neutrino-nucleon interaction diagram is shown in figure A.1. The invariant quantities are the following: The first one is the fraction of the lepton's energy loss in the laboratory frame.

$$y = \frac{qP}{M} = \frac{E - E'}{E} \tag{A.1}$$

where M is the nucleon mass, E is the initial energy of the neutrino and E' is the final energy of the lepton. The second invariant quantity is the square of the four-momentum transferred to the nucleon system.

$$Q^2 = -q^2 = 2(EE' - \vec{k} \cdot \vec{k'}) - m_l^2 - m_{l'}^2 \tag{A.2}$$

where $m_l(m_{l'})$ is the initial (final) lepton mass. Other invariant quantities are the arithmetic combinations of these two quantities and therefore cannot give additional information to differentiate background neutrino interactions from the ν_τ interactions.

Neutrino interactions are sources of background mainly if the primary lepton is not identified by the experimental set-up. In order to study this fact in detail, ν_τ CC interactions with all decay channels of the tau lepton and $\nu_{\mu,e}$ interactions

with the charm meson production are generated with simulation tools available in the CHORUS experiment. Moreover, ν_μ NC interactions are also generated to study the kinematical structure of white kink background.

Initially, kinematical properties of the background events are studied at the generator level with a generic detector simulation. A schematic sketch of the detector is given in figure A.2. Vertices of the events are placed inside the emulsion stack randomly. With this vertex position, the event is considered as background if the primary lepton, which is the μ in this case, is out of the acceptance of the calorimeter or if the energy of the primary lepton is less than 1.5 GeV. These two conditions are largely correlated since smaller energy brings larger angle with respect to beam direction due to the smaller Lorentz Boost. If the primary lepton is an electron, all events are considered as background. Detector smearing with the different detector resolution parameters, which are listed in table A.1, is also used in the calculations. White kink background is generated by randomly taking a hadron with $1 \geq E \geq 15 \, GeV$ energy attached to the primary vertex of ν_μ NC interactions and by assuming that this hadron makes an elastic scattering. The angle of the hadron with respect to the beam is taken as kink parent angle. The kink daughter angle is not considered since this parameter is not used in the study. Invariant kinematical quantities y and Q^2 are calculated for these events in order to be able to compare these parameters for signal and background events. The scatter plot of these parameters can be seen in figure A.3 for different neutrino interactions.

As can be seen from the plots, invariant quantities y and Q^2 are different for
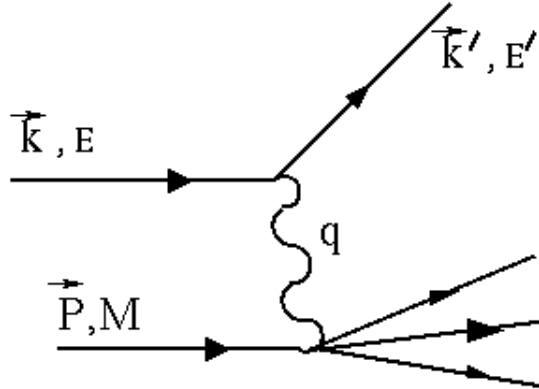
Figure A.1: Neutrino-nucleon interaction diagram

charm related background interactions compared to the tau production events. The condition of a low energetic primary lepton or that the lepton is out of the calorimeter acceptance, implies that y is close to 1.0 for these events. In the energy range of the CERN WB neutrino beam, the remaining energy is in most of the cases transfered to the nucleon system since the primary lepton takes only small fraction. Thus, Q^2 is expected to be high when y is close to 1.0 . It should be noted here that, the flavour of the interacting neutrino is known at this moment, which is not the case in reality. Since the calculation of the parameters are different for $\overline{\nu}_{\mu,e}$ and ν_{τ} interactions, it would not be possible to extract these plots from the experiment.

In reality, we do not know a priori which type of neutrinos made the interaction and the measurement of these kinematical parameters should give a clue about the neutrino type. The formula that is going to be used for calculating y, however, is different for $\overline{\nu}_{\mu,e}$ and ν_{τ} interactions since in the background case the primary
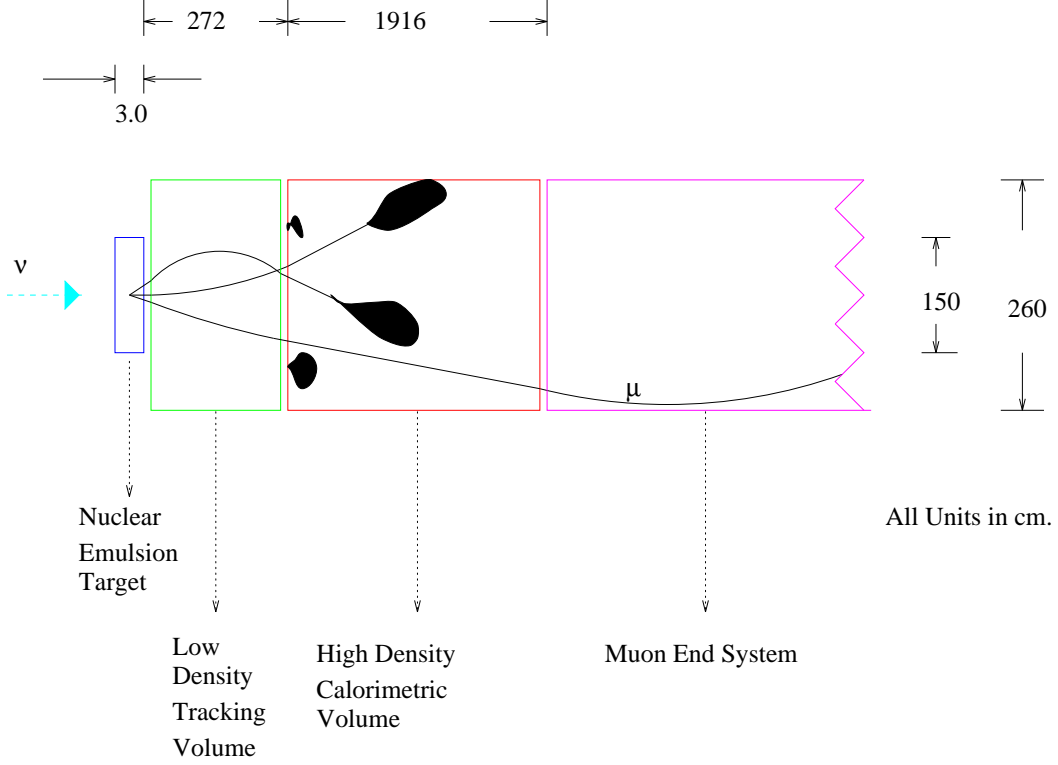
Figure A.2: Generic detector geometry

lepton is lost or low energetic and in the ν_τ case, the kink parent is the primary lepton itself. Formulas can be derived for ν_τ case and can be applied to both cases; ν_τ interactions should obey to the formula, while $\overline{\nu}_{\mu,e}$ interactions are not obeying. Q^2 and y parameters for ν_τ interactions are

$$y = \frac{E_\nu - E_\tau}{E_\nu} = \frac{E_X}{E_\nu} \tag{A.3}$$

$$Q^2 = 2(E_\nu E_\tau - P_\tau^L P_\nu^L) - m_\tau^2 \tag{A.4}$$

where E_X is the energy of the hadronic shower at the primary vertex. Taking into account the momentum balance in the transverse plane and making the assumption that the tau mass is negligible compared to its momentum, one can

109

Table A.1: Detector resolution parameters used for detector smearing

Measurement	Performance
Charge tag	$> 99\%$
Electromagnetic energy resolution	$13\%\sqrt{E}$
Hadron energy resolution	$33\%\sqrt{E}$
Muon momentum resolution	15%
Angular resolution of the emulsion (charged tracks)	5 mrad
Angular resolution of the calorimeter	10 mrad
Energy loss before the calorimeter	50 MeV

rewrite the equation as follows:

$$Q^2 = 2E_\nu \frac{E_X \sin\theta_X}{\sin\theta_\tau}(1 - \cos\theta_\tau) - m_\tau^2 \qquad (A.5)$$

where θ_τ is the angle of tau particle or kink particle with respect to the beam direction and θ_X is the angle of the hadron shower attached to the primary interaction vertex. Some more simplifications using properties of trigonometric functions can be done which results in

$$yQ^2 = 2E_X^2 \sin\theta_X \tan\frac{\theta_\tau}{2} \qquad (A.6)$$

At this moment, it is necessary to consider whether these parameters are accessible in the experiment. The CHORUS experiment has more information compared to other similar kinds of experiments such as bob-hybrid counter experiments. The main difference comes from the availability of the 3D high-resolution vertex detector which is the emulsion. Detector information from the CHORUS
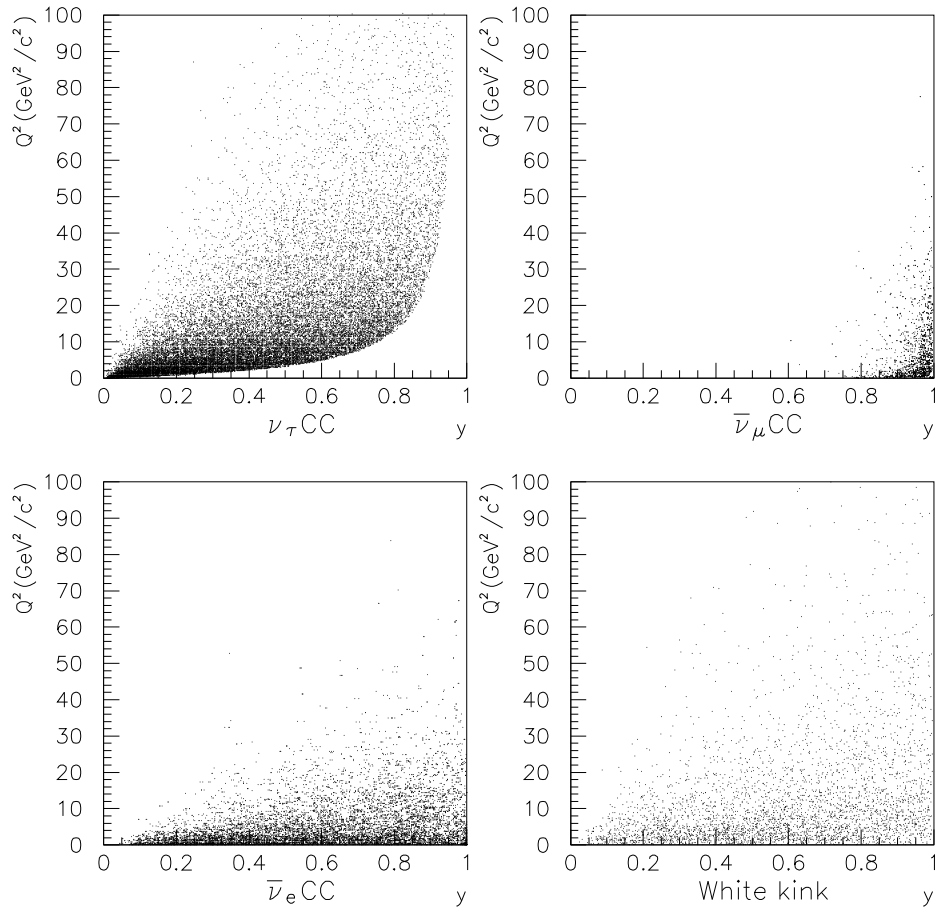
Figure A.3: Invariant kinematical quantities y and Q^2 for different neutrino interactions

detector, available for this study, includes particle charge and momentum information from diamond trackers and spectrometer, particle type from the calorimeter and spectrometer, shower energy and shower angle from the calorimeter and 3D vertex information from emulsion as mentioned earlier. For generic detector simulation, charged kink daughter particle's energy is assumed to be extracted from the calorimeter with the help of the tracker information. Neutral kink daughter particles, on the other hand, are assumed to be unidentified and their energy are left in the calorimeter shower energy calculations. For each particle within the direction of the calorimeter acceptance, 50 MeV kinetic energy loss is assumed for the penetration through the tracker medium between emulsion stacks and the calorimeter.

With the help of the experimentally available information, parameter E_T which is shower angle times shower energy and parameter θ_L which is angle of kink parent with respect to beam direction, are calculated. The relation between $E_T\theta_L$ and formula (A.6) is the following: If the formula (A.6) is slightly changed, one obtains

$$yQ^2 = 2E_X E_T \frac{\theta_\tau}{2} \qquad (A.7)$$

assuming that θ_τ is small enough. Therefore eqn.(A.7) contains the term $E_T\theta_L$ but it is not equal to it. Since the aim is here to develop a method to differentiate background events from ν_τ interaction events, we can consider $E_T\theta_L$ instead of eqn.(A.7). Actually, $E_T\theta_L$ should show the same behaviour as eqn.(A.7) because bringing in constant terms or adding the same parameters that exists already in

the equation like E_X, should not give more information for the interactions under study. Moreover, inserting the same parameter more than once will bring less differentiation power due to the finite resolution in these parameters. With these reasonings, $E_T\theta_L$ should map the yQ^2 distribution and give similar differentiation power between background and signal interactions.

The $E_T\theta_L$ distribution obtained from the generic detector simulation for different neutrino interactions are presented in figure A.4. $\overline{\nu}_\mu$ interactions have an $E_T\theta_L$ distribution similar to ν_τ interactions if the condition of undetected primary lepton is not imposed. This is the reason for the similarity of the distributions for $\overline{\nu}_e$ CC interactions and ν_τ CC interactions since electrons are assumed to be not identified. It can be noted also from figure A.4 that background and signal separation for white kink events is low and another method has to be applied. The lines in the figure are not normalised to event numbers of different neutrino interactions. The efficiencies for cuts applied to the samples, are summarised in table A.2.

Table A.2: Suppression factors for different background channels for sample cuts applied

Cuts	ν_τ CC	$\overline{\nu}_\mu$ CC	$\overline{\nu}_e$ CC	ν_μ NC[1]
$\theta_T > 100^o$	0.92	0.42	0.75	0.29
$\theta_L E_T > 0.04$	0.74	0.14	0.46	0.84
Total	0.72	0.05	0.41	0.22
$\theta_T > 100^o$	0.92	0.42	0.75	0.29
$\theta_L E_T > 0.025$	0.82	0.37	0.61	0.91
Total	0.79	0.11	0.52	0.25

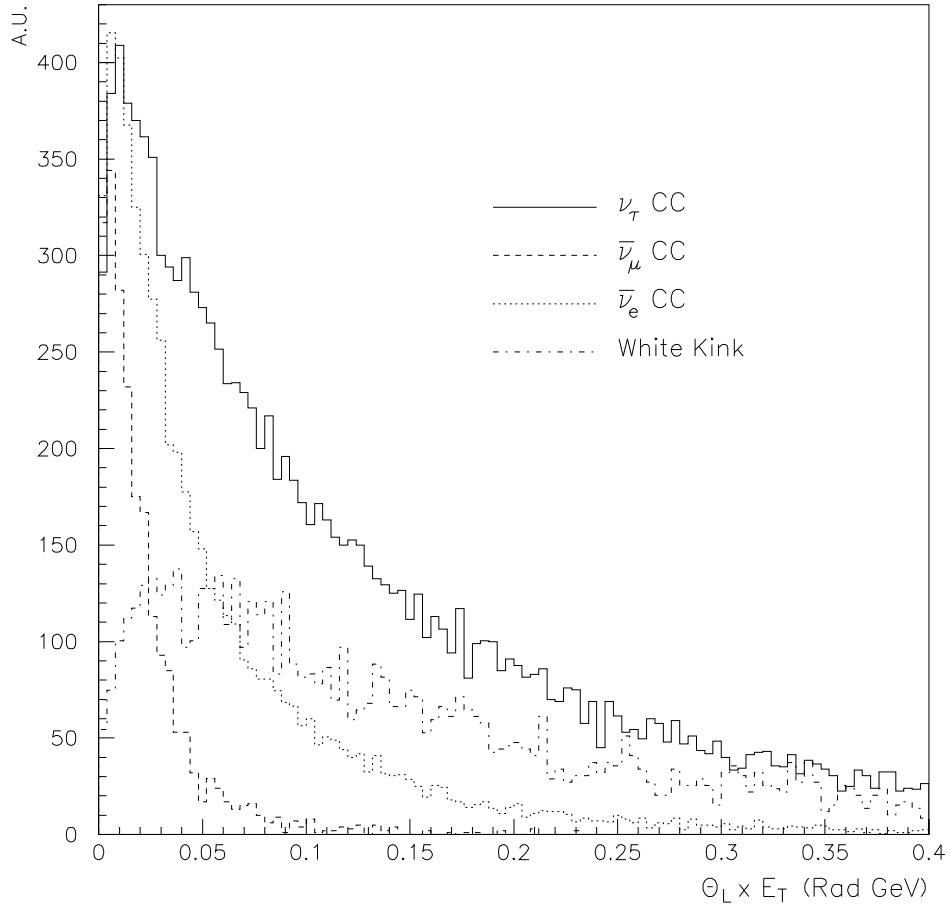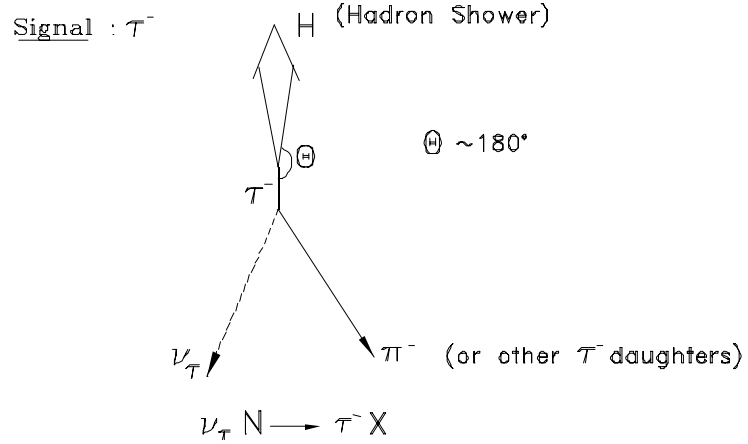The experimental parameter $E_T\theta_L$ works well in suppressing the background

Figure A.4: $E_T\theta_L$ distribution obtained by generic detector simulation for different neutrino interactions

generated by $\overline{\nu}_{\mu,e}$ CC interactions, however, another parameter is necessary to deal with "White kink" background. It is known that the transverse momentum of the kink parent has to balance that of hadron shower in ν_τ CC interactions contrary to the other cases. This can be checked very well with the measurement of an angle between kink parent and hadron shower by using both the calorimeter and emulsion 3D information. As shown in figure A.5, the transverse angle is close to 180° for ν_τ CC events, but would be small for both charm decays and white kink, where the kink parent is part of the hadron shower. Experimentally this parameter can be calculated by using 3D angle information for the kink parent from emulsion and by using the transverse momentum information from the calorimeter. The transverse angle distribution is shown in figure A.6 and corresponding cut efficiencies are listed in table A.2. As can be seen, the background behaves differently from ν_τ CC interactions and especially this method offers a powerful tool to separate the "white kink" background.
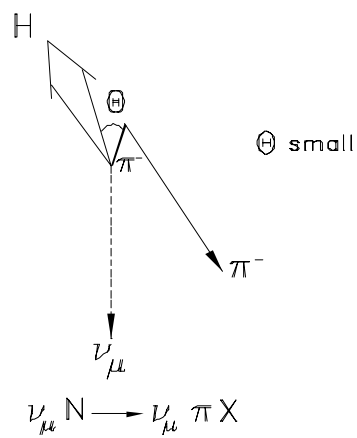
As a next step, experimentally measurable parameters $E_T\theta_L$ and θ_T are obtained with the full simulation of the CHORUS detector. Generated events are placed randomly inside the 4th emulsion stack. In order to gain simulation time and to have more statistics, $\overline{\nu}_\mu$ CC interaction events are skipped during the simulation if the primary lepton (μ^+) is out of the calorimeter acceptance. Low energetic muons inside the detector acceptance are left for later selection of in the analysis program. For this purpose, ν_τ CC interactions with electron decay channel of tau, $\overline{\nu}_{\mu,e}$ and $\nu_{\mu,e}$ CC interactions with all single prong decay channels

Vertex Kinematics : Transverse Plane

Signal : τ^-

H (Hadron Shower)

Θ

τ^-

$\Theta \sim 180°$

ν_τ

π^- (or other τ^- daughters)

$\nu_\tau \, N \longrightarrow \tau^- X$

Background:

"White Kink"

H

Θ

π^-

Θ small

π^-

ν_μ

$\nu_\mu \, N \longrightarrow \nu_\mu \, \pi \, X$

Charm (D$^-$) Decays

H

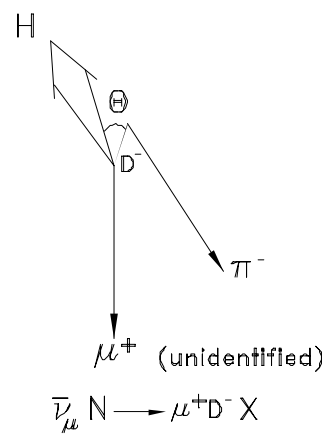Θ

D$^-$

π^-

μ^+ (unidentified)

$\overline{\nu}_\mu \, N \longrightarrow \mu^+ D^- X$

$\Theta \equiv$ Transverse Angle between Kink Parent and Hadron Shower

Figure A.5: A schematic diagram of transverse angle (θ_T) for different kinds of neutrino interactions
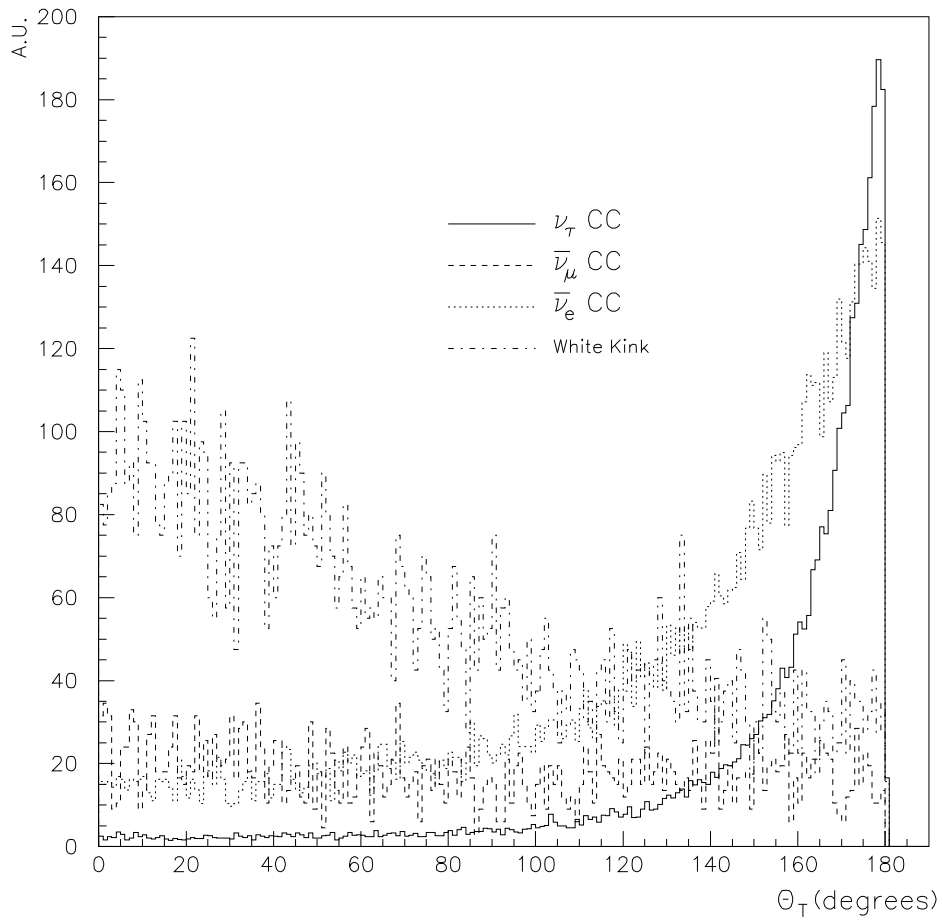
Figure A.6: θ_T distribution obtained by generic detector simulation for different neutrino interactions

of a charmed meson are simulated. The numbers of simulated events for mentioned neutrino types are listed in table 5.4. Since scanning information is not available, the angles in emulsion, like in the generic detector simulation case, are assumed to be measured with the precision of $5mrad$. All other parameters are obtained with the CHORAL analysis programme. Resulting plots are shown in figures A.7 and A.8.

For $E_T\theta_L$a similar behaviour is expected for neutrino and anti-neutrino interactions. Topologically the interactions are similar and slight differences can be expected from the different beam spectra. $E_T\theta_L$ distribution for background events, is shifted to higher values compared with the same distribution obtained from generic detector simulation. The reason for this effect is the conditions imposed on the events. The first condition is that the main trigger has to be satisfied. This is satisfied at the 99% level for ν_τ and background neutrino CC interactions. The second condition is that the event has to be reconstructed with CHORAL and the vertex has to be in the right stack which is the stack number 4 for this study. This condition brings some bias already. The last condition applied is that non-muonic tau decay event selection criteria have to be satisfied [51]. These conditions for events in 4th emulsion stack are summarised in table A.3. As can be seen from the cuts, the visible energy should be less than 10 GeV and transfer momentum should be greater than 1.9 GeV/c. These two conditions essentially cut off events on the lower part of yQ^2 distribution and they are the main conditions responsible for the different yQ^2 distribution from the one obtained by the generic detector simulation. For comparison, cut efficiencies

are calculated and presented in table A.4. The rejection power for background events is the same while the number of ν_τ interaction events is reduced more as a result. Criteria need to be tuned to reduce real event loss. In order to reproduce generic simulation results, two conditions (event vertex being in 4th stack and non-muonic event selection criteria) are removed and results are presented as corrected total sum of the efficiencies. This exercise shows that, detector resolutions are well presented in the generic detector simulation and the background rejection power is still valid for the reconstructed events in the CHORUS detector. It should also be noted that, the main background rejection power of $E_T\theta_L$ cut comes from the θ_L information and this is not effected very much by the full simulation. The value θ_L is measured precisely in emulsion ($\sim \pm 6 \ mrad$).

The parameter θ_T, on the other hand, is much more effected by detector resolution. Information from two different detector parts is necessary for the calculation of this parameter as mentioned before: angle information is provided by the emulsion and shower transverse momentum information by the calorimeter. A full simulation is more essential for the second part and as can be seen from θ_T plots, values are shifted more and the sharp peak is softened in the case of ν_τ CC interaction. A similar effect is also true for background events which can be followed more precisely from table A.4.

Finally, 19 CHORUS events with a kink, reconstructed in the 4th emulsion stack, are used to calculate $E_T\theta_L$ and θ_T values. Events are separated into two categories: events with no muon reconstructed and events with at least one muon reconstructed. One kink event observed with no muon reconstructed and with a
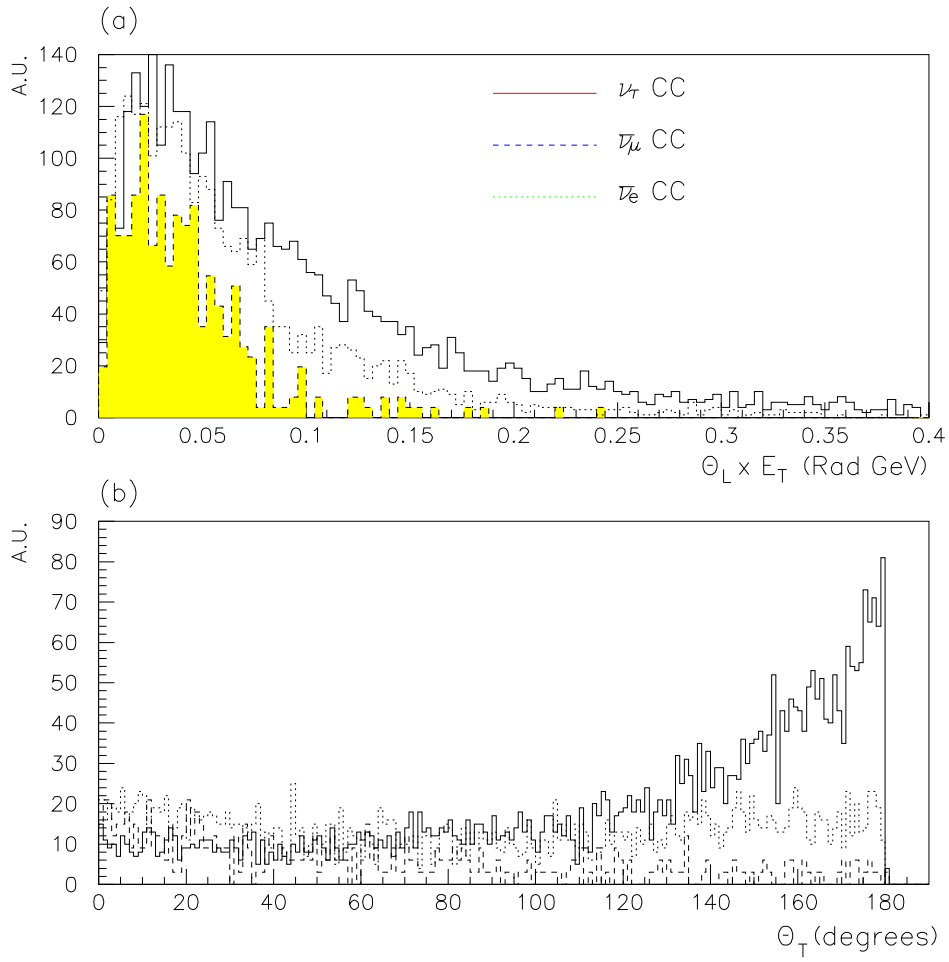
Figure A.7: a)$E_T\theta_L$ and b)θ_T distribution obtained by full detector simulation for ν_τ, $\overline{\nu}_\mu$ and $\overline{\nu}_e$ CC neutrino interactions

Figure A.8: a)$E_T\theta_L$ and b)θ_T distribution obtained by full detector simulation for ν_τ, ν_μ and ν_e CC neutrino interactions
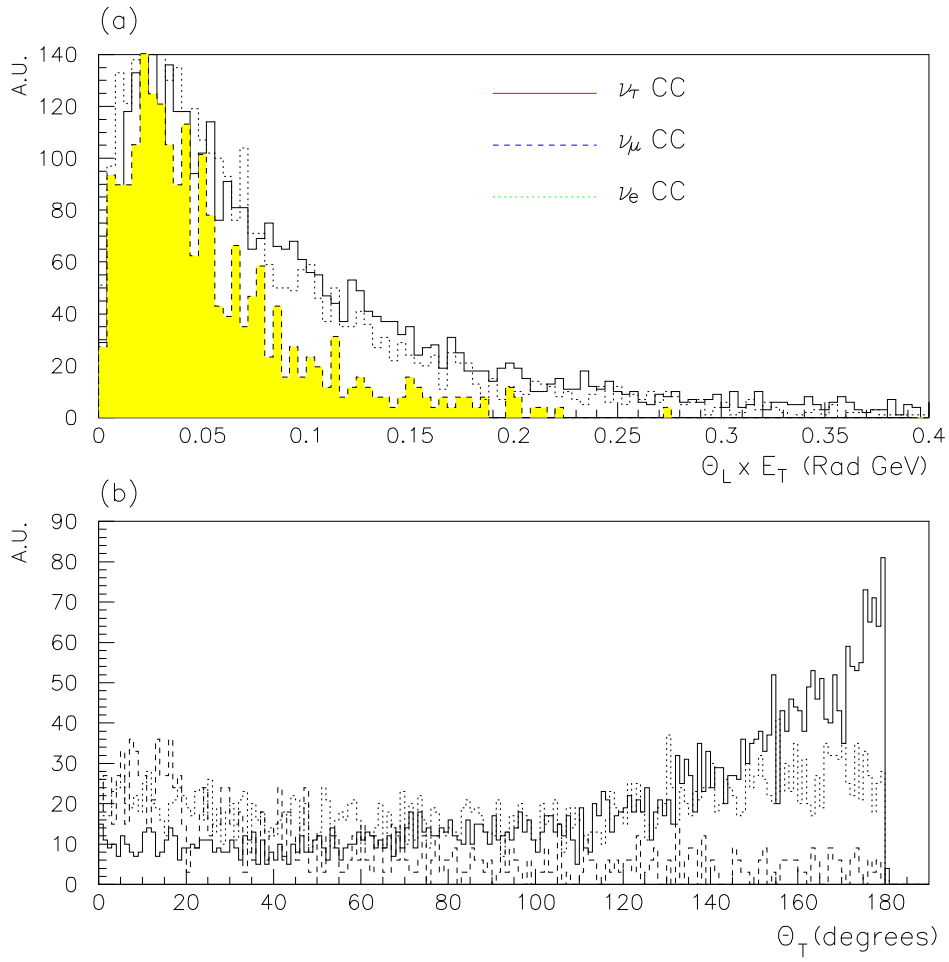
Table A.3: 0μ selection criteria for events in 4th emulsion stack

$10 \leq E_{vis} < 20$ GeV	and	$P^T \leq 1.9$	GeV/c
or			
$20 \leq E_{vis} < 40$ GeV	and	$P^T \leq 2.0$	GeV/c
or			
$E_{vis} > 40$ GeV	and	$\frac{P^T}{E} \leq 0.1$	1/c

Table A.4: Suppression factors for different background channels with a full detector simulation

Cuts	ν_τ CC	$\overline{\nu}_\mu$ CC	ν_μ CC	$\overline{\nu}_e$ CC	ν_e CC
$\theta_T > 100^o$	0.69	0.23	0.21	0.45	0.51
$\theta_L E_T > 0.04$	0.70	0.44	0.52	0.57	0.63
Total	0.53	0.07	0.07	0.25	0.33
Total (corrected)	0.79	0.11	0.13	0.36	0.49

blob attached to the kink, is studied as an example of kink events which occurr with an elastic scattering of hadrons in the emulsion. This event shows white kink behaviour for $E_T\theta_L$ and it has very small θ_T which strongly indicates that it is a kink event which has occurred by elastic scattering of an hadron. Events and their properties are listed in table A.5. Some events are able to pass the cuts on the sample, however, these events do not satisfy background rejection conditions. They have a muon on their primary vertex. For the moment, there is no event that can pass the cuts on the sample. Existing event statistics, on the other hand, does not give very solid proof of the method. More events are necessary for this purpose. These events are also drawn in figure A.9 and figure A.10 with MC results of corresponding interaction types to have visual comparison of the data.
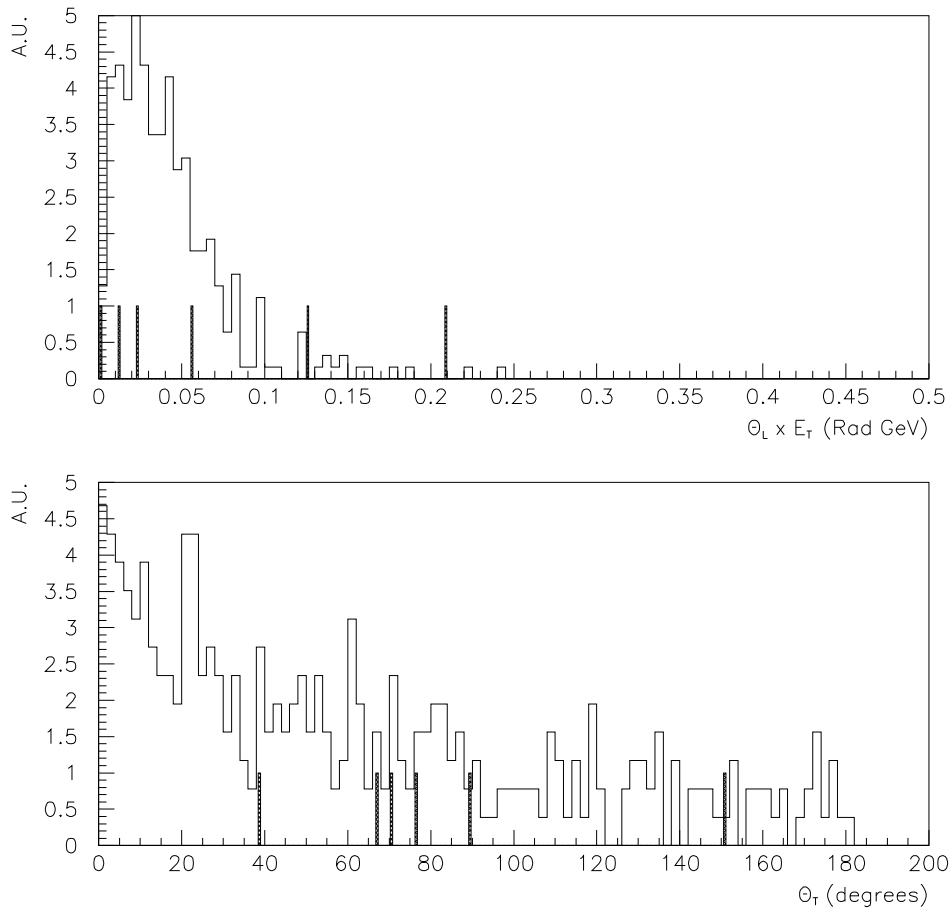
Figure A.9: a)$E_T\theta_L$ and b)θ_T distribution of the CHORUS events with no muon attached to the event and simulated $\overline{\nu}_\mu$ CC interactions with non-identified primary lepton
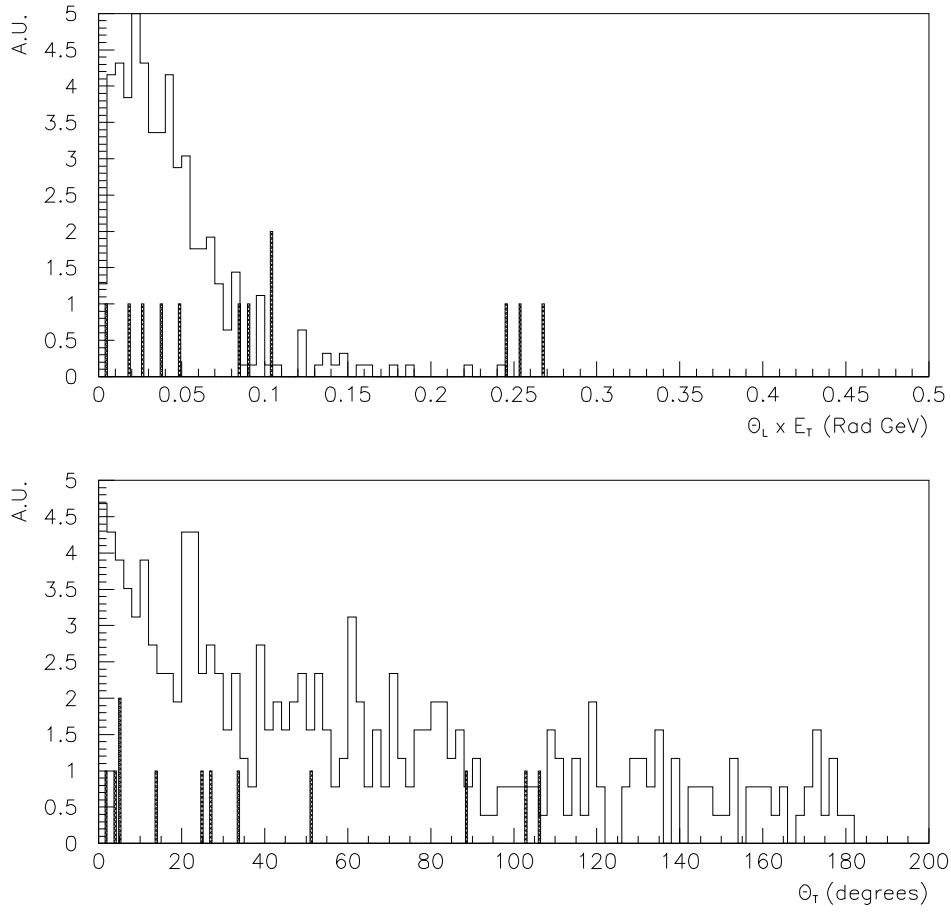
Figure A.10: a)$E_T\theta_L$ and b)θ_T distribution of the CHORUS events with one muon at primary vertex and simulated $\overline{\nu}_\mu$ CC interactions

Table A.5: Real kink events for year 1994 reconstructed and found in emulsion stack 4

Run Event	μ at primary	μ at secondary	blob at kink	$E_T\theta_L$	θ_T
426 185	no	no	no	0.209	77
616 1800	no	no	no	0.126	89
1237 1096	no	no	no	0.025	151
1443 3208	no	no	no	0.015	70
1608 5352	no	no	no	0.001	38
1767 1700	no	no	no	0.055	66
1105 1712	yes	no	no	0.037	5
1138 1190	yes	no	no	0.105	3
1244 867	yes	no	no	0.105	106
1875 1108	yes	no	no	0.041	51
1797 2024	yes	no	no	0.254	2
2003 2565	yes	no	no	0.268	27
2062 3724	yes	no	no	0.092	33
1052 3181	yes	yes	no	0.026	5
1265 1192	yes	yes	no	0.019	89
1429 2646	yes	yes	no	0.247	14
1550 3909	yes	yes	no	0.086	25
1689 5661	yes	yes	no	0.049	103
1141 2288	no	no	yes	0.387	3